COPPE
Instituto Alberto Luiz Coimbra de Pós-Graduação e Pesquisa de Engenharia
UFRJ

ASSESSING THE SUITABILITY OF SI/AL RATIO AS A REACTIVITY DESCRIPTOR FOR ION-EXCHANGED ZEOLITES FOR THE DIRECT METHANE TO METHANOL CONVERSION REACTION

Paulo Roberto Coelho Martins Junior

Dissertação de Mestrado apresentada ao Programa de Pós-graduação em Engenharia Química, COPPE, da Universidade Federal do Rio de Janeiro, como parte dos requisitos necessários à obtenção do título de Mestre em Engenharia Química.

Orientador: Henrique Poltronieri Pacheco

Rio de Janeiro
Junho de 2025

ASSESSING THE SUITABILITY OF SI/AL RATIO AS A REACTIVITY DESCRIPTOR FOR ION-EXCHANGED ZEOLITES FOR THE DIRECT METHANE TO METHANOL CONVERSION REACTION

Paulo Roberto Coelho Martins Junior

DISSERTAÇÃO SUBMETIDA AO CORPO DOCENTE DO INSTITUTO ALBERTO LUIZ COIMBRA DE PÓS-GRADUAÇÃO E PESQUISA DE ENGENHARIA DA UNIVERSIDADE FEDERAL DO RIO DE JANEIRO COMO PARTE DOS REQUISITOS NECESSÁRIOS PARA A OBTENÇÃO DO GRAU DE MESTRE EM CIÊNCIAS EM ENGENHARIA QUÍMICA.

Orientador: Henrique Poltronieri Pacheco

Aprovada por: Prof. Henrique Poltronieri Pacheco
Profa. Cristiane Assumpção Henriques
Profa. Sibele Berenice Castellã Pergher

RIO DE JANEIRO, RJ – BRASIL
JUNHO DE 2025

Coelho Martins Junior, Paulo Roberto

Assessing the Suitability of Si/Al Ratio as a Reactivity Descriptor for Ion-Exchanged Zeolites for the Direct Methane to Methanol Conversion Reaction/Paulo Roberto Coelho Martins Junior. – Rio de Janeiro: UFRJ/COPPE, 2025.

XIV, 78 p.: il.; 29, 7cm.

Orientador: Henrique Poltronieri Pacheco

Dissertação (mestrado) – UFRJ/COPPE/Programa de Engenharia Química, 2025.

Referências Bibliográficas: p. 67 – 74.

1. Modern catalysis. 2. Descriptors. 3. Scaling relations. I. Pacheco, Henrique Poltronieri. II. Universidade Federal do Rio de Janeiro, COPPE, Programa de Engenharia Química. III. Título.

À minha família,
a que me deu a vida
e a que na vida escolhi.
Ao Raphael.
À Mia & Leona.

Acknowledgments

Agradeço inicialmente a meu orientador, prof. Henrique, por todo o apoio incondicional ao longo dessa empreitada.

Agradeço também a todo o corpo técnico do NUCAT, em especial à Dora, Rodrigo, Evelyn e Anacleto, por todo o auxílio e paciência.

Agradeço à coordenação e a todos os professores do Programa, em especial ao prof. Fábio e profa. Cris.

Aproveito para, de maneira formal, agradecer aos órgãos de fomento, Conselho Nacional de Desenvolvimento Científico e Tecnológico (CNPq) e Coordenação de Aperfeiçoamento de Pessoal de Nível Superior (CAPES), que permitiram a execução deste trabalho e que permitem o avanço científico brasileiro.

Agradeço também ao Laboratório Multiusuário de Difração de Raios X do Instituto de Química da UERJ (LMDRX - IQ /UERJ), à profa. Sibele Pergher (UFRN) e ao Dr. Renato Barbosa junto ao Instituto SENAI de Inovação em Biossintéticos e Fibras, pela colaboração e suporte na condução deste trabalho.

Agradeço aos meus queridos colegas do PEQ que foram obrigados a me aturar, em especial àqueles do NUCAT.

Aos amigos que fiz ao longo da UFRJ, e neste momento em especial à Gabi que foi absolutamente fundamental nessa jornada e que espero levar para a vida.

Agradeço, obviamente, à minha família, que neste mundo em que muitos não tem as devidas oportunidades, me permitiu realizar tanto.

Aos meus sempre amados Vitor, Sara, Pedro, Carol e Isaías.

Agradeço também àqueles que me ajudaram a me manter razoavelmente são ao longos dos últimos anos, em especial à doida da Melissa.

Faço um agradecimento especial ao Vinícius, por muito, mas especialmente por ter me dado apoio para que eu tivesse força em momentos muito difícies.

Agradeço às minhas gatas por terem me mostrado tanto amor.

Finalmente, agradeço ao Raphael, à quem eu amo e devo tanto e que não existem palavras suficientes para descrever a importância na minha vida.

No mais, agradeço a todos que direta ou indiretamente tenham me apoiado e colaborado para a execução deste trabalho.

"All models are wrong, some are useful."

George Box

Resumo da Dissertação apresentada à COPPE/UFRJ como parte dos requisitos necessários para a obtenção do grau de Mestre em Ciências (M.Sc.)

ASSESSING THE SUITABILITY OF SI/AL RATIO AS A REACTIVITY DESCRIPTOR FOR ION-EXCHANGED ZEOLITES FOR THE DIRECT METHANE TO METHANOL CONVERSION REACTION

Paulo Roberto Coelho Martins Junior

Junho/2025

Orientador: Henrique Poltronieri Pacheco

Programa: Engenharia Química

Este trabalho investiga a influência da razão Si/Al no desempenho catalítico da mordenita (MOR) trocada com cobre (Cu) na conversão direta de metano em metanol (dMtMc), avaliando seu potencial como descritor da produtividade de CH_3OH. Para isso, amostras de MOR com diferentes razões Si/Al foram preparadas por dealuminação controlada utilizando ácido oxálico. Essas amostras foram posteriormente submetidas a protocolos padronizados de troca iônica para a obtenção dos catalisadores do tipo Cu-MOR. A atividade catalítica foi avaliada por meio de um protocolo em etapas, empregando ar como agente de ativação e vapor de água como agente de dessorção. Diversas técnicas de caracterização foram aplicadas para a análise das propriedades estruturais e texturais, bem como a composição dos materiais. Os resultados confirmaram a eficácia dos procedimentos de modificação e preparação, resultando em catalisadores com composições e propriedades distintas. A desaluminização provocou mudanças sistemáticas na cristalinidade e porosidade. Cu foi incorporado com sucesso em quantidades adequadas em toda a série de materiais. Os testes catalíticos indicaram produção de CH_3OH em quantidades distintas em todas as amostras. Os experimentos revelaram a possível existência de tendências associadas à razão Si/Al, embora não tenha sido possível estabelecer uma correlação entre a estrutura e o rendimento de CH_3OH. As amostras analisadas apresentaram comportamentos específicos, sugerindo que o ambiente estrutural pode influenciar a especiação dos sítios ativos, embora outros fatores também pareçam desempenhar um papel relevante. Assim, os resultados indicam que, embora a razão Si/Al afete o desempenho dos catalisadores do tipo Cu–MOR, ela não pode ser considerada, no presente escopo, um descritor da atividade catalítica nesse tipo de sistema.

Abstract of Dissertation presented to COPPE/UFRJ as a partial fulfillment of the requirements for the degree of Master of Science (M.Sc.)

ASSESSING THE SUITABILITY OF SI/AL RATIO AS A REACTIVITY DESCRIPTOR FOR ION-EXCHANGED ZEOLITES FOR THE DIRECT METHANE TO METHANOL CONVERSION REACTION

Paulo Roberto Coelho Martins Junior

June/2025

Advisor: Henrique Poltronieri Pacheco

Department: Chemical Engineering

This work investigates the influence of the Si/Al ratio on the catalytic performance of Cu-exchanged mordenite (MOR) for the direct methane-to-methanol conversion (dMtMc), assessing its potential as a descriptor for CH_3OH productivity. In order to do so, MOR samples with varying Si/Al ratios were prepared through controlled dealumination using oxalic acid. Those samples were then submitted to ion-exchange protocols under standardised protocols to produce Cu-MOR catalysts. Catalytic activity was assessed via the stepwise protocol utilising air as activation agent and steam as desorption agent with product detection carried out by FTIR spectroscopy. Several characterisation techniques were applied for the evaluation of compositional, structural and textural properties of the material. The results confirmed the effectiveness of the modification and preparation procedures, leading to catalysts with distinct compositions and properties. Dealumination induced systematic changes in crystallinity and porosity. Cu was successfully introduced in adequate amounts across the material series. Catalytic tests showed measurable CH_3OH production for all Cu-containing samples, with varying intensities of CH_3OH and other products. Spectroscopic analysis revealed trends related to Si/Al ratio, though no universal or direct correlation between framework composition and CH_3OH yield could be firmly established. Sample-specific behaviours were observed, suggesting that structural environment may influence active site speciation, though additional factors likely play a significant role. Thus, the findings indicate that while the Si/Al ratio can affect Cu–MOR performance, it cannot, under the scope of this work, yet be considered a standalone descriptor of activity in these catalytic systems.

Contents

List of Figures

List of Tables

Chapter 1

Introduction

1.1 Motivation

Natural gas (NG) is expected to remain a key energy source for the transition from fossil fuels to a sustainable renewable energy economy.[1] However, over 150 billion m^3 of NG are annually wasted by flaring or venting due to the absence of cost-effective routes for transport or processing, specially in remote areas.[2] Such not only represents a massive waste of resource, but also a significant input of CO_2 to the atmosphere, strongly contributing to climate change. Methane (CH_4), the main component of NG, is a potent greenhouse gas (GHG), whose global-warming potential (GWP) is more than 20 times that of CO_2 over a 100-year timeframe.[1, 2] The main use of NG is energy generation, specially through direct combustion. However, it is also extensively processed through steam methane reforming (SMR) to produce synthesis gas (syngas), a mixture of hydrogen (H_2) and carbon monoxide (CO), which serves as building block for several chemicals. For instance, SMR is the main route for purified H_2 production, primarily used in ammonia (NH_3) production. Syngas is often utilised to produce liquid hydrocarbons, specially synthetic fuel, via Fischer-Tropsch synthesis (FTS), or other valuable chemicals. Additionally, syngas is used in methanol (CH_3OH) synthesis.[1, 3]

CH_3OH is a highly versatile liquid chemical and one of the most important chemical plataforms.[3] It gained attention as a possible H_2 carrier and alternative liquid fuel.[1, 4] Although effective, the well-established industrial production of CH_3OH from CH_4 suffers from several technical and economical bottlenecks. First of all, CH_3OH synthesis from syngas is only economically viable at large scale. The same is valid for SMR, which additionally demands temperatures often above 1000 K, and pressure over 30 bar, resulting in a high energy demand considering the required infrastructure scale. Consequently, such facilities are geographically restricted to locations with high feedstock availability. Moreover, large scale processes, with several

sub-processes, imply intrinsic process efficiency losses. These challenges underscore the the necessity of developing an alternative that could potentially enable decentralised utilisation of CH_4 sources, preferably in a direct route, without the need of an intermediate, to produce CH_3OH.[3, 4]

The direct methane-to-methanol conversion (dMtMc) represents one of the most impactful and scientifically challenging topics, which recently gained increased attention, reflected in a steady rise in research publications throughout the years (Fig. 1.1). One of the most promising approaches is the partial oxidation of methane over zeolites containing copper (Cu). These materials are able host specific redox-active Cu–oxo species in their porous frameworks. Their behaviour mimics the action of methane monooxygenases (MMOs) enzymes found in methanotrophic bacteria, known to enabling dMtMc to occur at moderate conditions. However, key limitations still prevent both biological and heterogeneous catalytic systems from being scaled to industrial processes. It is important to highly that biological systems demand very specific conditions, making them usually only suitable for rather small scale. Regarding the zeolitic counterpart, many of the most selective systems work under non-catalytic, stoichiometric conditions and require separate activation and desorption steps, leading to low overall productivity.[5–13]

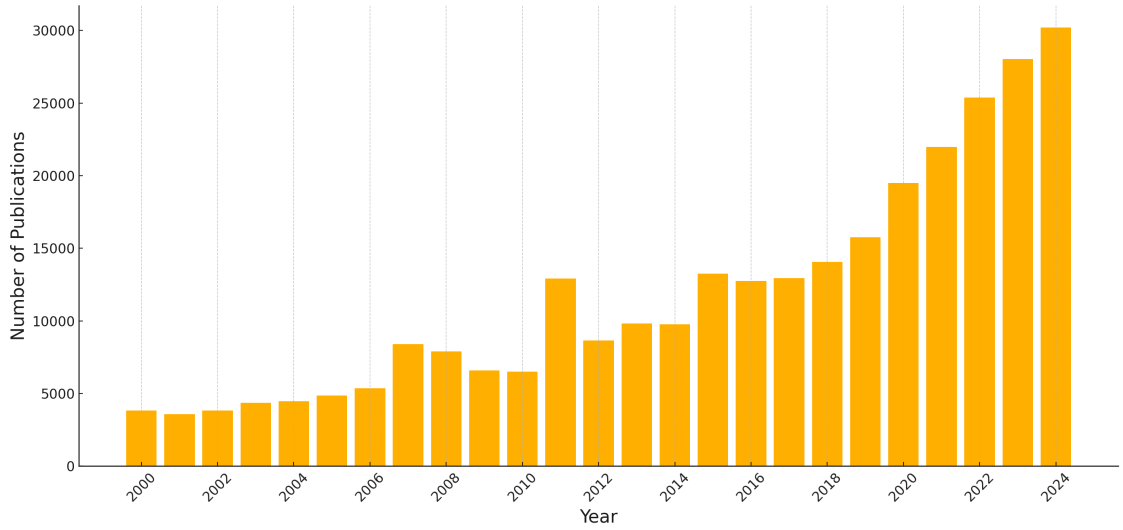

Figure 1.1: Number of publications regarding "Methane-to-Methanol" according to Dimensions^{TM} scientific metrics platform on research regarding metrics of publications on "Methane-to-Methanol" from 2000 to 2024 on 15 May 2025.

Despite several efforts to address such issues, major questions remain, particularly concerning the exact nature of active sites for dMtMc reaction and the mechanistic pathway. Additionally, there is growing evidence on the influence of support framework structure on the speciation and redox potential of Cu species.[9, 12, 14, 15] A key structural composition feature of zeolites is the framework Si/Al ratio. It can be understood as an indirect indication of the number and

spatial distribution of framework charges, which in turn are known to impact Cu ion location, coordination, and potential for forming redox-active species.[9, 10, 15] Thus, such environmental nuances ultimately affect catalytic performance. However, a systematic understanding of how framework composition governs Cu site speciation and ultimately catalytic function remains incomplete. Most studies in the literature examine only a limited set of framework compositions or rely on commercial materials with fixed Si/Al, making it difficult to establish any possible structure–function correlations. Hence, the Si/Al could potentially be used as a design parameter for enhanced dMtMc catalysts. Since Si/Al holds several framework information which potentially relate to the electronic and geometric environment of exchanged Cu species, thereby modulating redox behaviour, active site distribution, and ultimately methanol yield and selectivity, it may possibly be used as a descriptor for the catalytic activity of such catalyst.[9, 10, 14, 15]

1.2 Objective

The present work aims to evaluate how changes in Si/Al influence the formation, stabilisation, and reactivity of Cu species in zeolites, particularly Cu-oxo clusters in mordenite (MOR) and what could potentially be the reasons. In order to achieve this, the following specific objectives were established:

- To effectively prepare a series of Cu-exchanged MOR catalysts with diverse Si/Al, via a systematic modification protocol of MOR zeolites, for subsequent catalytical assessment.
- To characterise the obtained samples in order to evaluate if the implemented protocols were effective on producing a working catalyst.
- To assess the catalytic activity of the Cu–MOR series in the stepwise dMtMc protocol.
- To investigate the existance of a relationship between suppost structure and catalytic performance, with a focus on CH_3OH productivity.
- To explore whether the Si/Al can serve as a descriptor for Cu speciation and catalytic behaviour in Cu-zeolite systems, and to identify possible trends or scaling relationships.

1.3 General Divisions of the Thesis

This document is divided in 5 main chapters after this brief introduction. Chapter 2 dwells on the basic physical principles governing interactions and their possible consequences one the formation of catalytic sites. Chapter 3 describe the experimental methodology applied in this work. Whereas chapter 4 presents and discusses the raw obtained results. Finally, chapter 5 offers the conclusions that can be obtained from the present work and suggestions to further refine the findings.

Chapter 2

Theoretical Background

2.1 Direct Methane-to-Methanol Conversion

CH_4, the primary component of natural gas, is a highly abundant and stable hydrocarbon. Its conversion into CH_3OH, a critical step in utilising CH_4 for chemical synthesis and energy applications, poses a long-standing challenge in catalysis due to CH_4 strong inert nature (C–H bond dissociation energy is circa 104 kcal/mol), as well as its non-polar nature, which makes selective activation difficult under mild conditions[3, 13]. The direct partial oxidation of CH_4 to CH_3OH is especially challenging because CH_3OH is more reactive than CH_4 and is therefore susceptible to over-oxidation to CO or CO_2, particularly in the presence of strong oxidants [8, 13]. As a result, traditional industrial methods proceed via an indirect, multi-step process that first converts CH_4 into syngas (a mixture of CO and H_2) using high-temperature steam reforming (Eq. 2.1), followed by catalytic CH_3OH synthesis over $Cu/ZnO/Al_2O_3$ catalysts under high pressure (Eq. 2.2). This route operates at temperatures of 973 K – 1373 K and pressures of 20 bar – 100 bar, requiring extensive infrastructure [3, 13]. The conventional route can be summarised as follows:

$$CH_4 + H_2O \rightarrow CO + 3H_2 \qquad \Delta H = +206 \text{ kJ/mol} \tag{2.1}$$

$$CO + 2H_2 \rightarrow CH_3OH \qquad \Delta H = -91 \text{ kJ/mol} \tag{2.2}$$

It is noteworthy that the direct reaction of CH_4 with molecular oxygen (O_2) to produce methanol (CH_3OH) is fundamentally forbidden under Wigner's spin selection rules [5, 16]. According to these quantum mechanical rules, the total spin of a system must be conserved in an elementary reaction step. CH_4 exists in a singlet ground state ($S = 0$), while O_2 exists in a triplet ground state ($S = 1$) due to its two unpaired electrons occupying degenerate π^* anti-bonding orbitals. CH_3OH is also a singlet (Eq. 2.3). As such, the net spin transition from:

$$CH_4\ (\text{singlet}) + O_2\ (\text{triplet}) \rightarrow CH_3OH\ (\text{singlet}) \tag{2.3}$$

involves a transition from an initial triplet to a final singlet state, which is spin-forbidden in a single elementary step. Such fundamental constraint helps explain why no homogeneous or heterogeneous system has been found that catalyses the direct one-step CH_4 oxidation with O_2 to CH_3OH at ambient conditions. Catalytic systems can bypass this limitation through multi-step pathways involving electron transfer, which allow for a stepwise redox-mediated spin manipulation.[5, 17]

Biocatalytic direct MtM conversion is efficiently carried out by methanotrophic bacteria, which operate under ambient temperature and pressure using a class of enzymes known as methane monooxygenases (MMOs). [13, 18] MMOs exist in two distinct forms: the soluble methane monooxygenase (sMMO), which functions in the cytoplasm and features a diiron active site, and the particulate methane monooxygenase (pMMO), a membrane-bound enzyme whose active site contains one or more Cu ions (Fig. 2.1), though the exact nuclearity and geometry of the site are still under active debate. [9, 12, 19] In both systems, CH_4 oxidation is understood to proceed via a stepwise mechanism, beginning with the activation of molecular oxygen and formation of a high-valent metal–oxo intermediate, capable of hydrogen atom abstraction (HAA), followed by the homolytic C–H bond cleavage on the CH_4 molecule and a radical rebound step that yields CH_3OH. [12, 18, 19]

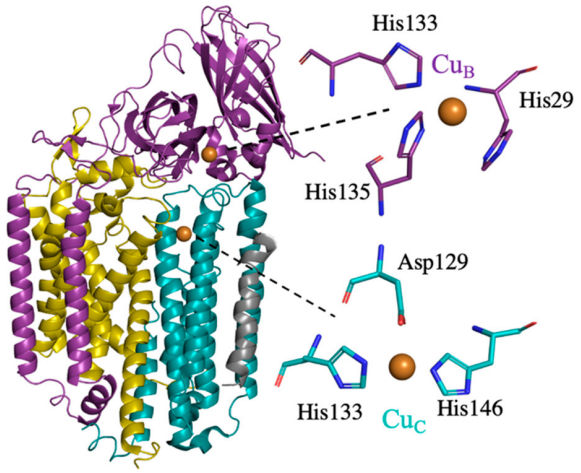

Figure 2.1: A single protomer from the crystal structure of *Mc. sp. str. Rockwell* pMMO (PDB accession code 4PHZ). PmoA is light gold, PmoB is purple, PmoC is teal, and an unidentified helix is gray. The two copper ions are shown as spheres and to the right are expanded to show the modeled coordinating residues. Reprinted from Reference [20]

Despite the remarkable selectivity and mild operating conditions of these enzymes, scaling their use for industrial applications remains challenging. The key

limitations include the slow microbial growth rates and the instability of enzymes in industrial conditions. [10, 12, 18] These drawbacks have motivated the design of biomimetic systems that emulate MMO-like reactivity by replicating the biocatalysed radical hydroxylation chemistry in homogeneous or heterogeneous settings. [10, 13]. The most promising approach for industrial applications involves zeolites exchanged with Cu or Fe, and have been widely studied.[11, 12] These systems are particularly attractive because the zeolite lattice can stabilise catalytically active species. Upon activation with oxidants such as N_2O, O_2, or H_2O_2, the metal sites are oxidised to generate high-valent species capable of HAA.[11–13]. While these systems are promising, challenges such as over-oxidation to CO or CO_2, particularly when oxidising agents remain present during the CH_3OH formation step, as well as catalyst deactivation, remain.[12, 21, 22] A widely adopted strategy to mitigate these limitations and improve CH_3OH yield is to decouple the CH_4 activation and CH_3OH extraction steps to enhance selectivity. [11, 21]

Despite significant progress in catalyst development and mechanistic understanding, the commercial viability of direct MtM conversion (dMtMc) remains prohibitive.[21] The key barriers include: (i) low CH_3OH yield per catalytic cycle (as reported in Tab. 2.1), much below industrially relevant thresholds [22]; (ii) the relatively high catalyst cost, particularly for its low-stability [4]; and (iii) unresolved issues related to process scalability, including the need for multi-step protocols [11, 12, 21]. Nevertheless, dMtMc remains one of the most highly sought-after transformations in heterogeneous catalysis, frequently referred to as a "dream reaction". The development of advanced catalysts is one crucial step on the strategy to achieve viability.[10, 19, 21, 22]

Table 2.1: Different reported CH_3OH yields. Adapted from Reference [4]

Cu-zeolite	**Cu** / wt%	**Activation Temperature** / K	**Reaction Temperature** / K	**Yield CH_3OH** / mol mol_{Cu}^{-1}
MFI	8.3	723.15	473.15	0.06
MOR	8.2	723.15	473.15	0.32
MOR	8.1	723.15	473.15	0.03
MOR	4.8	723.15	473.15	0.02
MOR	2.3	773.15	473.15	0.17
CHA	8.9	773.15	473.15	0.20
CHA	4.9	723.15	473.15	0.04
CHA	3.2	723.15	473.15	0.09

2.2 The Sabatier Principle

The fundamental principle governing heterogeneous catalysis is the change on the interaction energy of a system with a specific configuration that allows or facilitates its evolution into a different configuration. This is achieved thanks to the interaction of all related species, including the catalyst, which takes place due to their electronic properties. [23] The surface interaction between fluid and solid species is defined as adsorption. Adsorption can occur via physisorption, which involves weak van der Waals forces, or chemisorption, in which chemical bonds between the adsorbate and the catalyst surface are effectively formed. Then, the adsorbed species interact with each other via elementary chemical reactions. Ultimately, the heterogeneous catalysis phenomena includes adsorption of reactants on the catalyst surface, surface reaction(s), and product desorption (Fig. 2.2). These are all in nature simply the reorganisation of electronic structures.[3, 23, 24]

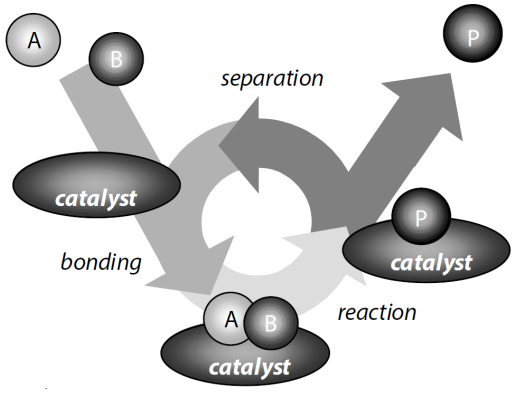

Figure 2.2: Most simplified catalytic cycle. Reprinted from Reference [3].

Since the perturbation of the electronic structures of the reacting species is the phenomenon behind heterogeneous catalysis, the strength and type of interactions taking place in a certain system influence the reaction pathway and catalytic efficiency.[3, 23, 25] Hence, the nature of those electronic structures is the defining parameter of interaction, henceforth called catalytic activity. On the catalyst surface, activity is governed by the specific geometric arrangements and electronic properties of the surface structure, defining the active sites. On solid surfaces, these active sites often arise from low-coordination atoms, step edges, or strained regions, where local variations in electronic density enable the breaking and formation of chemical bonds with high specificity.[23, 25]

Heterogeneous catalysts can be complex arrangements of metals, oxides, sulphides and other chemical compositions.[3] Many of the most active heterogeneous catalysts are composed of transition metals, whose partially filled d-orbital offer unique flexibility in bonding. The electronic landscape of these materials, especially

the position and width of the d-band relative to the Fermi level, governs their ability to donate or accept charge during interaction with adsorbates.[23] The d-band arises from the overlapping of close neighbouring d-orbitals as they interact in a very localised manner (Fig. 2.3). When a reactant binds to a transition metal site, the interaction is mediated by the overlap between their own molecular orbitals and the transition metal's d-states, forming new hybridised states and, therefore, bonding and anti-bonding states (Fig. 2.4).[3, 16, 23]

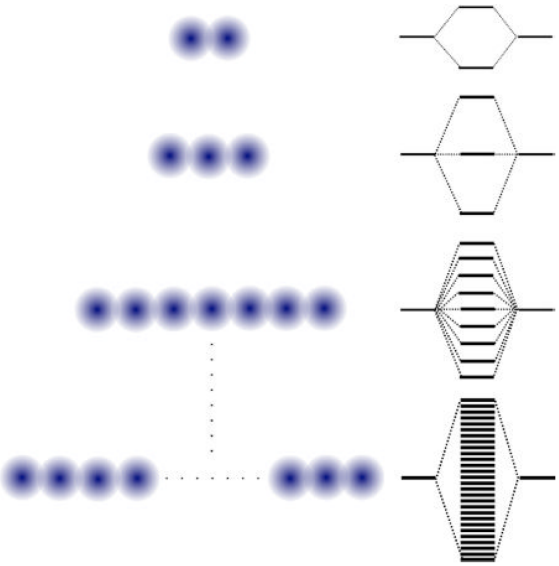

Figure 2.3: Schematics showing what happens in the limit of infinitely many overlapping orbitals. Reprinted from Reference [23]

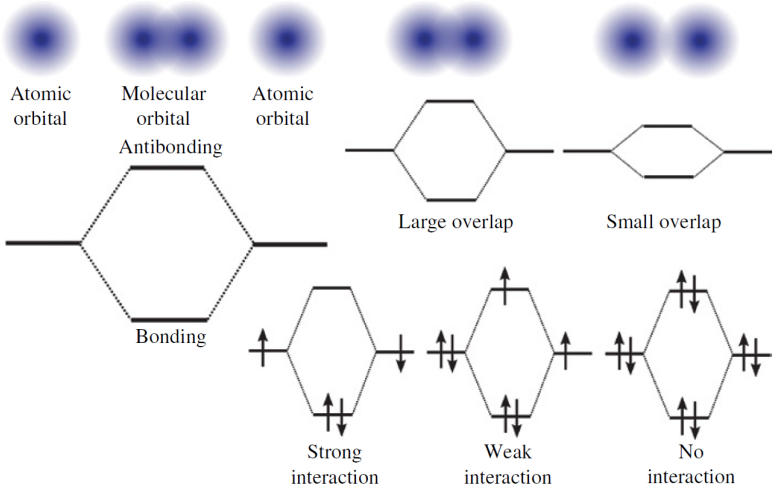

Figure 2.4: Molecular orbital energies depend on the overlap of the constituent atomic orbitals; the bond strength depends also on the occupation of the orbitals.[24] Reprinted from Reference [20]

The occupation of the aforementioned bonding and anti-bonding states results in electrons being transferred or shared across the interface. This phenomena is

known as electronic donation and back-donation. Electrons may flow from filled orbitals of the metal into vacant orbitals of the adsorbate, characterising donation, and simultaneously from filled orbitals of the adsorbate into unoccupied metal states, characterising back-donation (Fig. 2.5). Ultimately, the final configuration of bond-

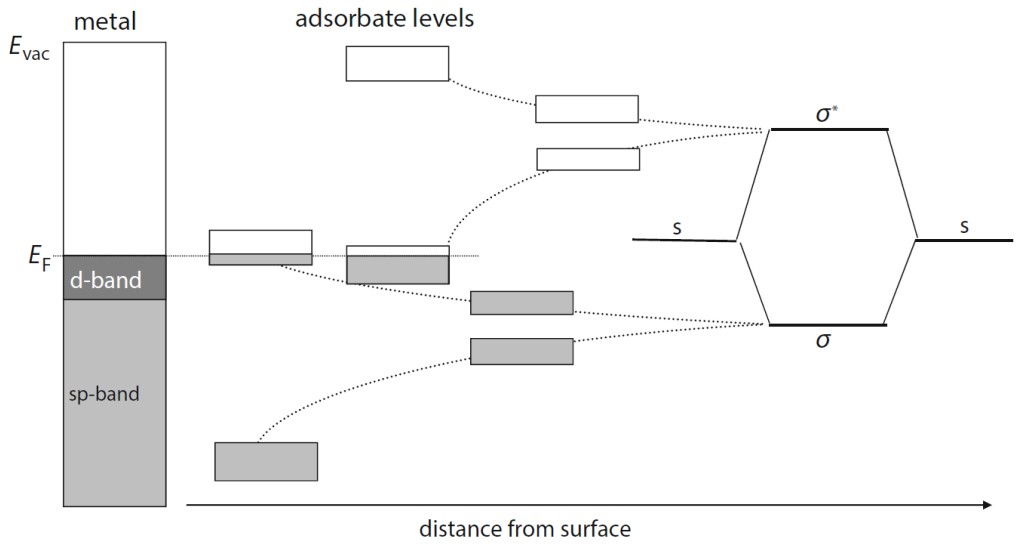

Figure 2.5: A molecule with a bonding σ and anti-bonding orbitals $\sigma*$ interacts with both the sp band and the narrow d-band of the transition metal. The former leads to the lowering and broadening of the bands, while the latter results in splitting into bonding and anti-bonding orbitals. Reprinted from Reference [3]

ing and anti-bonding states determines the binding strength. The binding strength is the central concept for the Sabatier principle. First proposed over a century ago, the Sabatier principle remains a cornerstone of modern catalysis. It states that for a catalyst to be maximally effective, its interaction with intermediates must be neither too weak nor too strong. If the binding is too weak, the reactants fail to adsorb or activate; if too strong, the products or intermediates become trapped on the surface, blocking further turnover (Fig. 2.6). Only when the interaction lies in an optimal intermediate regime can the catalyst promote the reaction without impeding its continuity.[3, 23, 24, 26]

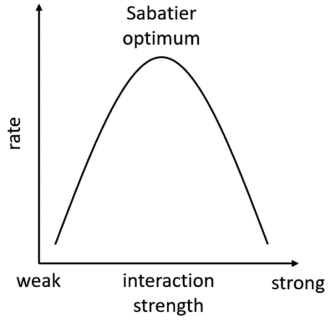

Figure 2.6: Schematic diagram qualitatively representing the Sabatier principle. This is what is called a volcano plot. Reprinted from Reference [27]

The Sabatier principle manifests itself in the well-known volcano plots, where catalytic activity is plotted against a descriptor, often the adsorption energy of one key intermediate or an electronic structure parameter like d-band filling (Fig. 2.7). These plots reveal a non-monotonic trend in which activity rises with increasing binding strength up to a point, beyond which further strengthening leads to deactivation. The apex of the volcano corresponds to the ideal compromise: a catalyst which electronic properties harmonise adsorption, activation, and desorption. In such way, the most effective catalysts are those able to perfectly balance the binding strength to related species. Recently, advances in quantum mechanical modelling, particularly density functional theory (DFT), have enabled researchers to connect experimentally observed activity trends with computable electronic descriptors. Those descriptors, such as the position of the d-band centre, work function, or charge transfer capacity, function as critical metrics that capture the essence of how a catalytic system operates and can serve as predictive tools in rational catalyst design.[3, 23, 24, 26, 28]

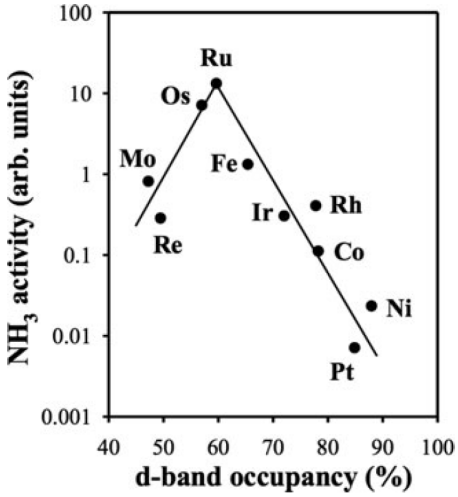

Figure 2.7: Ammonia activity correlates to d-band occupancy following Sabatier's Principle and forming a vocano plot. Reprinted from Reference [3]

Traditionally, catalytic development, both in process and material, rely on empirical methods with iterative testing under various several conditions. The strategy of using descriptors to guide the development of catalysts allows researchers to navigate the vast combinatorial space of materials more intelligently and efficiently.[3, 23, 25, 26, 28–30] Emerging computational techniques, including artificial intelligence and machine-learning, offer further enhancement to high-throughput screening. This is particularly interesting when combined with descriptor-based strategies, not only for its predictive precision, but also for its ability to translate fundamental theoretical insights into practical synthetic directions. [14, 23–26, 28] A critical combination of such approaches, aligned with experimental validation, further enhances our ability to engineer catalysts with tailored properties.[24–26, 30]

In fact, ammonia synthesis catalysts have been historically designed guided, although probably not formally, by direct application of the Sabatier Principle (Fig. 2.8).[3, 23, 28] Improvements on the hundred year process are studied up to this day. A recent study [31] demonstrated how applying strain in Pd(111) surfaces shifts the adsorption energy of key intermediates such as *N and *NH, in which the * indicates that the species is adsorbed on the catalyst. The application of such can effectively predict catalytic activity for ammonia synthesis, offering a clear route to fine-tune performance.[3, 23] Another recent study [32] presented how the electronic structure of the support affects metal-support interaction and, consequently, catalytic performance, by correlating the valence band maximum of various supports with turnover frequencies in ammonia synthesis over Ru nano-clusters. By doing so, it introduced a catalyst support descriptor for the guided material selection for advanced catalysts' formulation.

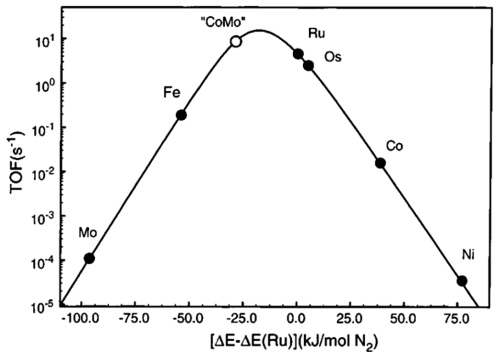

Figure 2.8: Calculated turnover frequencies for ammonia synthesis as a function of the adsorption energy of nitrogen. Reprinted from Reference [33]

The mentioned studies demonstrate the direct application of the ideas implicit in the Sabatier principle, executed with atomistic precision in order to enhance well established processes.[23, 28, 31, 32] The same strategy is applied on the development of completely new processes, following pathways that would not be considered before. For instance, the *d*-band centre was used as a universal descriptor for NO electro-reduction, allowing high-throughput screening of electrocatalysts for selective NH_3 synthesis.[34] Another study focused on optimising the electrocatalytic N_2 oxidation to HNO_3, using the difference in adsorption free energy (ΔG_{ads}) between N_2 and N_2O_2 as a descriptor for the selective oxidation activity. This strategy enabled the identification of doped-graphene catalysts with activity even at ambient condition.[35]

Following the same idea, the adsorption free energy of hydrogen (ΔG_H), as well as the *d*-band centre and the electron localisation function, were used as descriptors of the hydrogen evolution reaction (HER) activity over MoS_2 catalysts, allowing the identification of optimal dopants.[36] On the other hand, doping of perovskite

catalyst for the oxygen evolution reaction (OER) was modulated thanks to the use of the occupancy of the e_g orbital as a descriptor of activity.[37] Additionally, the number of excess electrons was proposed as one descriptor for the same OER activity of metal oxides, guiding the prediction of another system.[38] It is worth noting that it is known that structural defects are responsible for those excess electrons, which by nature are simply localised electron transfers that occur due to specific established electronic configuration, demonstrating the effect of structural environment directly in the electronic properties that govern catalytic activity.

2.3 Zeolite Materials

Zeolites are crystalline materials composed primarily of aluminosilicates. They compose a distinctive class of oxides characterised by their extremely well-defined network of SiO_4 and AlO_4 tetrahedra, forming a framework containing pores, with diameters ranging from 2 Å to 13 Å, capable of hosting various species like ions and even molecules. They are essentially formed by periodic structures containing a selection of building units that are basic arrangements of TO_4 (where T is either Al or Si), connected by oxygen corner sharing atoms, into rings, cages and channels, which combination renders different frameworks. [3, 17, 24, 29, 39]

Zeolites are categorised based on their framework type, as defined by the International Zeolite Association (IZA). Each framework type is specifically defined according to its own specific building blocks arrangement and porosity, giving rise to channels and cages, a configuration that periodically repeat forming the unit cell. A codified name is given to each type.[3, 39] Each framework type exhibits a specific pore system that can be one-, two-, or three-dimensional. Additionally, the size of the channels and cages is also well-defined according to the number of central T-members contained in the essential rings composing the building blocks and uniform throughout the framework. Hence, their ability to store different species vary as per the framework type.[3, 39] The different spatial configurations also offer specific confinement systems, allowing for geometric selectivity.[3] Fig. 2.9 shows the structures of some zeolites and their respective pore systems.

Some structures such as mordenite (MOR), faujasite (FAU) and ferrierite (FER) are among the approximately 45 naturally occurring zeolite types. They are also some of the most important industrially applicable frameworks. Nonetheless, the intrinsic variability and impurity in naturally occurring minerals limit their application. For that reason, the tailored synthesis of zeolites, where crystallographic purity, compositional control, and framework uniformity can be precisely managed, was of great interest in the second half of the 20th century.[3, 24, 29, 40]

Typically, zeolites are synthesised under hydrothermal conditions. For such,

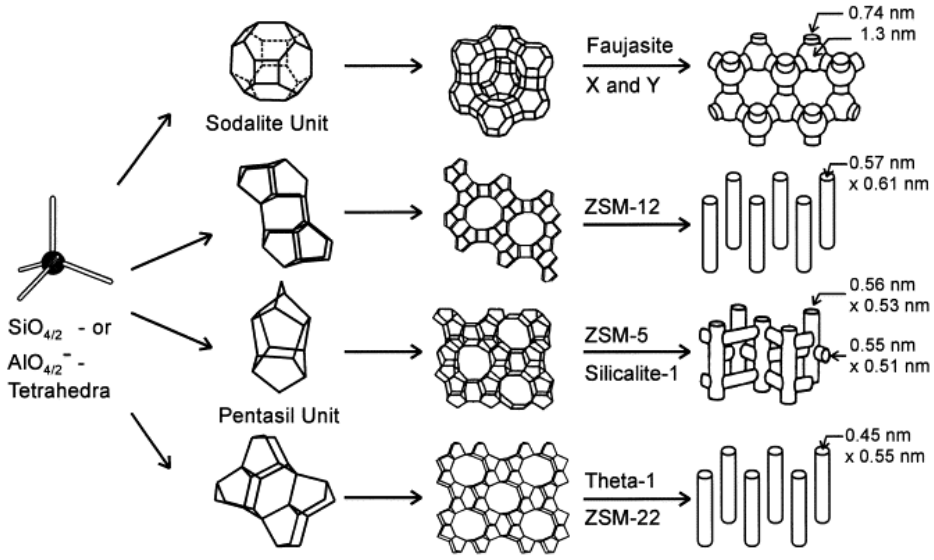

Figure 2.9: Structures of four commercial zeolites (from top to bottom: Faujasite (FAU) or zeolites X, Y; zeolite ZSM-12; zeolite ZSM-5 or silicalite-1; zeolite Theta-1 or ZSM-22) and their micropore systems and dimensions. Reprinted from Reference [40]

a precursor gel containing alumina and silica sources, mineralisers and structure-directing agents (SDA) is produced, transferred into autoclaves and subjected to thermal treatment under static or dynamic (e.g., tumbling) conditions, initiating the nucleation and growth of zeolite crystals. Although the full mechanistic pathway remains unresolved, the formation process is generally understood to occur in two main stages: an initial nucleation phase followed by a crystal growth phase. During nucleation, silicate and aluminate monomers undergo a dynamic equilibrium of polymerisation and de-polymerisation, yielding amorphous or partially ordered precursors. These nanostructured entities exist in equilibrium with dissolved species and their size distribution is strongly influenced by the SDA identity, mineraliser concentration, and synthesis conditions. The mineraliser acts enhancing the solubility and mobility of framework-forming species, while SDA acts as a template that stabilises specific framework topologies, guiding the crystallisation into producing a certain zeolite type.[3, 24, 29, 40]

It is worth noting that substituting Si^{4+} by Al^{3+} in a tetrahedral unit creates a formal negative charge that must be compensated with the presence of compensating cations, often catalytically active, in order to maintain neutrality. When such cations are protons, as depicted in Fig. 2.10, the material can act like a Brønsted acid (a proton donor). These cations are not randomly distributed within the pore system, but stabilised at specific crystallographic positions due to steric and geometric constraints and electrostatic interactions.[3, 12, 15, 24, 39, 41] Al^{3+} substitution obeys topological and energetic constraints summarised by the Loewenstein's rule

states that Al-O-Al linkages are forbidden and, therefore, Al centres are always separate by at least one Si centre. Such constraint imposes a statistically restricted distribution of Al atoms on the framework, therefore generating a spatial dependent electrostatical potential field from the localised formal charge induced by the presence of AlO_4^-.[3, 15, 24] The total electrostatic potential at a lattice site arising from the surrounding charges of the framework can be quantitatively described by the Madelung potential.[41–44]

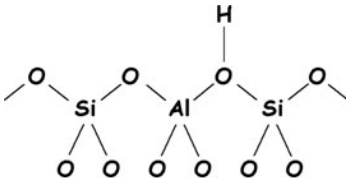

Figure 2.10: Principle of a solid acid: the proton compensates the deficient charge of the aluminum ion (3+) to match the valence of the silicon ion (4+). Reprinted from Reference [3]

Effectively, the presence of a negative charge creates a potential well, whose depth can be accessed by the value of the Madelung potential. Considering a simplified model in which a transition metal ion, M^{x+}, is embedded within a SiO_4 array periodically containing AlO_4^- units. As the density and proximity of such units increase, therefore lowering the formal charge and the Madelung potential, the net electrostatic field at the metal site becomes stronger. As a consequence, there's a increased ligand field splitting, altering *d*-orbital populations and spin state stability. Thus, a more negative Madelung potential lowers the energy of the unoccupied *d*-orbitals of a transition metal ligand stabilised in the electrostatic potential well created by negative charges, effectively impacting adsorption energies and, thus, catalytic activity.[3, 15, 24, 41–44]

From a thermodynamic point-of-view, nearby Al atoms are energetically disfavoured due to Coulombic repulsion and entropy loss, but under certain synthesis regimes they may be kinetically trapped during crystal nucleation and growth. However, the statistical probability of forming close Al atoms decreases exponentially with increasing Si/Al.[16, 24, 42, 44] Thus, the Si/Al, while often treated as a simple compositional parameter, exerts multidimensional control over the structural, electronic, and thermodynamic landscape of the zeolite framework. Beyond geometric effects, the Si/Al also governs the acidity, hydrophilicity, and hydrothermal stability of the zeolite, influencing both its catalytic and mechanical robustness.[3, 24, 44] For instance, acid strength increases with Si/Al due to the enhanced inductive effect of silicon-rich surroundings on the bridging OH group (Si–OH–Al). These stronger Brønsted acid sites may compete with metal centres for reactants or intermediates.[24]

The Si/Al can be tailored in three main ways: (i) by adjusting the ratio between Si and Al sources, mineralisers and SDA, as well as adjusting synthesis conditions such as pH, temperature, and time, directly during zeolite crystallisation itself; (ii) by post-synthesis removal of Si atoms from the framework (desilication) via treatment with alkaline solution, decreasing Si/Al; or (iii) post-synthesis removal of Al atoms from the framework (dealumination) via acid leaching, hydrothermal treatment, or their combination, increasing Si/Al. Regardless of the methodology, preferential positioning will occur based on access of species and energy minimisation. Moreover, crystallinity and structure uniformity and integrity are always affected. For instance, framework type imposes limits to the Si/Al range, directly impacting the crystallisation process. On the other hand, post-synthesis approaches usually introduce mesoporosity to the framework, giving rise to secondary porosity (hierarchical) and a distinct kinetic regime. Depending on the severity of such treatments, outcomes from the formation of local defects to the complete disruption of the zeolitic framework are possible. In addition, post-synthesis modification can result on the entrapment of amorphous phases (extra-framework species) inside the material lattice, due to inefficient removal.[3, 15, 24, 40, 45]

When post-synthetic methods are performed in a highly controlled manner, they can effectively tune Si/Al without disrupting framework and crystallographic integrity. [3, 24, 40, 45] The controlled acid leaching using oxalic acid has been demonstrated to selectively chelate framework Al whilst hydrolysing formed extra-framework aluminium (EFAL) species, facilitating their removal under mild conditions, minimising structural collapse and accumulation of EFAL.[45] Nonetheless, accumulation may always take place due to a multitude of factors, including the stabilisation of a wide range of EFAL species by the framework. Depending on the mobility of EFAL species, they are able to self-organise into cationic clusters and become complexes with more than one Al centre that may be stabilised at different locations (Fig. 2.11) during high-temperature zeolite activation. Those species usually find preferential siting inside the framework based on a favourable coordination and charge-compensation environment.[46]

Although zeolites are by themselves catalytically active materials able to perform a range of reactions[3, 29], they are often functionalised with the introduction of transition metals to their structure in order to perform other reactions, especially those involving the electron transfer. Thanks to their very special properties, zeolites can participate in the catalysis, exhibiting a cooperative effect with the incorporated transition metal; furthermore, they can merely act as a support, which in turn can potentially affect reactional performance. Among the most common strategies for metal incorporation are impregnation and ion-exchange, both of which offer distinct advantages and limitations depending on the nature of the metal precursor,

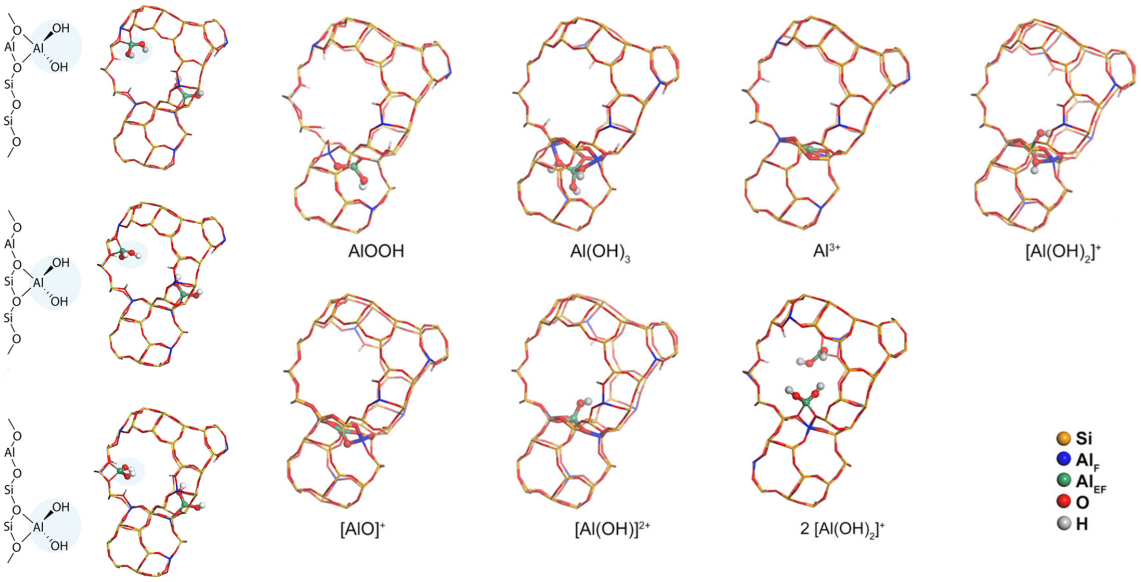

Figure 2.11: Structures of some possible EFAL species stabilised in FAU. Adapted from Reference [46]

the properties of the support, and the desired loading, dispersion and catalytic properties.[3, 39, 47]

Impregnation involves the deposition of metal precursors onto the zeolite through the infiltration of a solution followed by drying and thermal treatment. Two main variants are commonly used: (I) Incipient wetness impregnation (IWI), in which the volume of the metal precursor solution is matched to the pore volume of the zeolite, ensuring minimal excess solvent and efficient uptake, although risking preferential deposition near pore openings and external surfaces. IWI is relatively simple and widely used for scale-up, but it often yields non-uniform metal distributions and is prone to forming large metal oxide particles upon calcination; and (ii) Wet impregnation (WI), in which an excess volume of precursor solution is used, allowing for diffusion and equilibration of the metal throughout the pore system, this approach can improve dispersion if followed by careful drying but may result in poor loading uniformity. While impregnation allows for higher metal loading and a broad choice of precursors, it generally offers less control over the final configuration. The resulting species may reside inside pores, on external surfaces, or as aggregates depending on the treatment conditions and the nature of the support.[3, 29, 39, 47]

Ion exchange exploits the intrinsic cation-exchange capacity of zeolites, already mentioned, in which the compensating cations are replaced by transition metal cations from an appropriately prepared solution. This method typically produces well-dispersed, isolated metal ions located at or near Al sites. Consequently, ion exchange is highly dependent on the total number of exchangeable sites, which depends on the Si/Al as explained; the distribution of Al atoms, pH and composition of the exchange solution, temperature and contact time, which govern equilibrium

and diffusion. Since this approach leverages electrostatic attraction, it is generally more selective and yields metal species in defined positions, often within the inner pore system. However, it is limited to metal precursors that can exist as soluble cations under the desired conditions, and typically results in lower metal loadings than impregnation.[3, 15, 29, 39, 47]

Regardless of the approach, the success of metal incorporation and the resulting stabilised species are closely related to the physicochemical properties of the zeolite. Framework topology influences accessibility of the precursor and confinement effects on species; while Si/Al defines the number of exchangeable sites and the hydrophobicity of the material, and the Al distribution affects whether isolated or multi-nuclear species can be formed and stabilised (Fig. 2.12). For instance, frameworks with low Si/Al tend to stabilise higher densities of metal ions but may also introduce stronger electrostatic interactions and favour aggregation if not controlled. Conversely, high-silica zeolites may yield lower dispersion but could also potentially offer improved thermal stability and hydrophobicity. Hence, the choice of incorporation method must be carefully coordinated with the structural and compositional characteristics of the zeolite to achieve desired catalytic performance, especially when targeting specific oxidation states, coordination geometries, or redox cycling behaviour.[24, 39]

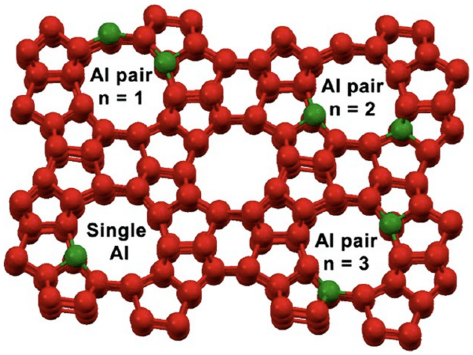

Figure 2.12: Some possible configurations of Al distribution within MFI framework. Reprinted from Reference [48]

As previously mentioned, each Al atom introduces a negative charge into the zeolite lattice, generating a localised electrostatic field. This electrostatic landscape, reflected in the Madelung potential, is not uniform, but highly dependent on Al distribution, Si/Al, and crystallographic topology of the framework. Regions of the framework that contain clustered Al atoms or lie near silanol nests, especially in post-synthesis modified materials, may create deeper electrostatic wells capable of stabilising higher-valent or multi-nuclear metal species, while isolated Al atoms, in as synthesised high-silica environments, may favour mononuclear or low-valent cations. Since the spatial variation in local potential directly modulates the ligand

field strength, influences the splitting of *d*-orbitals, and determines the energetic accessibility of different redox and coordination states, even if the same metal precursor and incorporation technique are used, the final speciation, oxidation state, and catalytic reactivity of the resulting active centres can differ depending on the zeolite's framework local configuration.

2.4 Copper-Exchanged Zeolites

One of the earliest metals used by humanity, Cu use can be traced back to approximately 7,000 years. Thanks to several advancements in smelting and alloying techniques throughout history, it is considered one of the most versatile metals. Thus, it is now the third most utilised metal by weight. The advent of electricity in the mid-19th century marked a turning point, propelling its demand and usage. Since then, Cu consumption has surged dramatically, while production costs and market prices have generally declined.[49] Positioned on the group 11 of the periodic table, Cu sits at an intersection between the noble metals behaviour and that of more reactive transition metals. It has an electron configuration of $[Ar]3d^{10}4s^{1}$, exhibiting two oxidation states, +1, Cu(I), with a d^{10} distribution, and +2, Cu(II), with a d^{9} distribution.[50] As already mentioned, a crucial framework for understanding reactivity in transition metal chemistry is the filling of the *d*-band.[3, 24]

Earlier transition metals, such as Fe (d^{6}) and Co (d^{7}), have partially filled *d*-band, therefore exhibiting comparatively higher affinity for ligands, resulting in strong metal–ligand bonds (Fig. 2.13). On the other hand, Cu possesses a complete (in a d^{10} configuration) or almost complete (in a d^{9} configuration) *d*-band. Consequently, their interactions with ligands are distinct to those of Fe and Co, for

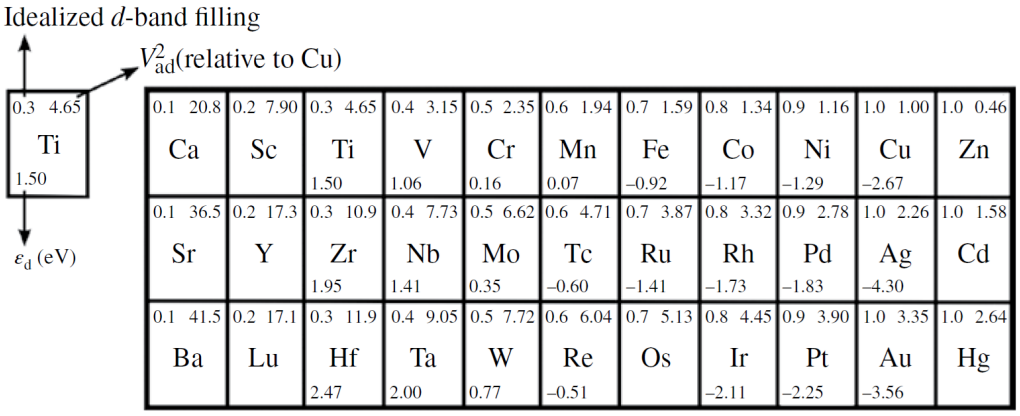

Figure 2.13: Part of the periodic table, showing a number of electronic structure parameters. The d-band centers are calculated for the most close-packed surfaces of the experimentally predicted crystal structures fcc(111), hcp(0001), and bcc(110). The idealized d-band fillings are shown in the upper left corner, and a coupling matrix element relative to Cu. Reprinted from Reference [26]

example. Adsorption energies are weaker, and bond activation is less energetically demanding, particularly the activation of strong covalent bonds. Such behaviour can be explained by the fact that the closer the d-band is to being full, the lower the metal–adsorbate coupling strength, because there are fewer empty states near the Fermi level to accept electrons from bonding orbitals. This weaker, more moderate interaction turns out to be critically important in catalytic reactions involving oxygenated intermediates. In particular, Cu milder reactivity favours the formation and stabilisation of partially oxidised species, rather than driving them to complete oxidation products such as CO_2 and H_2O. For instance, taking the strong C–O bond chemistry as an example, Fe readily activates and cleaves C–O bonds, and Co and Ni exhibit high propensities for deep reduction or cracking reactions. In contrast, Cu tends to promote partial oxidation and moderate bond activation, stabilising oxygenated species without excessively weakening their C–O bonds. It is precisely an intermediate reactivity that renders Cu uniquely suited for processes like CH_3OH synthesis. Not surprisingly, Cu-based catalysts (notably $Cu/ZnO/Al_2O_3$) are the most commonly employed in the industrial CH_3OH synthesis process from syngas. In this scenario, Cu sites are selective for the hydrogenation of CO or CO_2 to CH_3OH, carefully balancing adsorption strength, strong enough to activate C=O bonds, but weak enough to desorb the partially hydrogenated product (CH_3OH) without further over-reduction to CH_4.[3, 24]

An interesting catalytic system emerges from combining the unique chemical behaviour of Cu with the structural precision, high surface area, and tunable environment of zeolites. Such system is very relevant, for example, in the context of emission control for its performance on the decomposition of nitrogen oxides ($2\,NO \rightarrow N_2 + O_2$), in which the challenge lies in cleaving the N=O bond and recombining nitrogen atoms to form N_2 without forming N_2O nor re-oxidising intermediates. Such in mediated through the dynamic redox cycling between Cu^+ and Cu^{2+} states. [14, 51] It is worth noting that, in theory, the same redox-active Cu centres that cleave the N=O bond to form N_2 and O_2 could assist in the recombination of N_2 and O_2 back into NO, an intrinsic ability of every catalyst known as microscopic reversibility. The actual feasibility and rate of these reverse reactions depend critically on kinetic and thermodynamic conditions. These conditions may be explored to produce distinct processes, by adjusting operational conditions or even the catalyst structure in order to guide the direction of the process.[3, 24]

As already explained for the general case of transition metals, the zeolite framework is far more than a passive scaffold. Through its composition (that can be represented by the Si/Al), topology, and charge distribution, it can govern the geometry, electronic structure, and reactivity of Cu species hosted within its pores.[3, 10, 12, 14, 15, 24, 41–44] Hence, understanding the catalytic properties of

Cu species confined in zeolitic environments requires a rigorous investigation into their electronic structure. This involves analysing how the Cu $3d$-orbitals are split by the ligand field imposed by the surrounding framework oxygens in which they sit, how electron density is transferred between the framework ligands and the Cu centre via ligand-to-metal and metal-to-ligand charge transfer, and how the redox states and spin configurations of Cu are stabilised within the complex electrostatic potential landscape generated by the framework.[3, 10, 15, 17, 24, 41–44]

One foundational tool for understanding such effects is ligand field theory (LFT), an advanced conceptual framework that extends the crystal field theory (CFT) by incorporating both electrostatic attraction/repulsion and orbital overlap between metal and ligands. In the original CFT, ligands are treated as negative point charges that surround a central metal ion, creating an anisotropic electric field that changes the degeneracy of the metal's d-orbitals. The specific pattern of orbital splitting depends on the geometry of the coordination environment. The electrostatic approach is refined by introducing the concept of orbital overlap between the ligand's lone pairs (or π-systems) and the metal's empty or partially filled d-orbitals. This allows for σ-donation (ligand to metal electron density transfer) and π-back-donation (metal to ligand π^*-orbital interactions), leading to a strengthening in metal–ligand bonds. In addition to electrostatics, the rigid spatial constraints of the zeolitic framework alter metal–ligand bond angles and lengths, leading to distortions in the overlap geometry between the Cu d-orbitals and the lone pairs of the framework oxygen. These distortions modify the ligand field strength, the orbital overlapping, and ultimately the bonding scheme.[16, 17, 24]

In the case of Cu^{2+} species within a zeolitic framework, the ligand field induces a strong Jahn–Teller distortion, particularly in axial versus equatorial ligand fields, resulting in a preference for the usual six-coordinate tetragonal geometry, a distorted octahedral. This leads to an asymmetric orbital occupation, where the unpaired electron typically occupies the e_g-orbitals, namely $d_{x^2-y^2}$ and d_{z^2}, that have lower symmetry. The magnitude and specific characteristics of such distortion are particularly sensitive to the ligand nature, and the local electrostatic potential, as well as the geometry imposed by the surrounding. Very restrict surroundings (robust, non-moving framework and spatial confinement) can suppress certain vibrational and rotational levels, restricting some relaxation stages, altering bond angles and lengths, and consequently affecting both the orbital splitting and the spin density distribution on the resulting Cu sites. In contrast, Cu^{1+}, although generally found as a four-coordinated tetrahedral, should not exhibit a strong preference for any specific geometry, resulting in the preponderance of framework topology effects on the splitting patterns and spin-density distribution in such species. As a result, different Cu centres will exhibit unique orbital configurations, which are not purely

metal-localised, but in reality represent hybridised orbitals shaped by the quantum symmetry constrains imposed by the zeolite framework.[15, 17, 24, 43, 52–54]

Thus, Cu species in zeolites can exist in various forms, including $[CuOCu]^{2+}$ (mono-(μ-oxo)-dicopper), $[Cu_2O_2]^{2+}$ (bis-(μ-oxo)-dicopper), and $[Cu_3O_3]^{2+}$ (tricopper) clusters (Fig. 2.14), each of these that may be related to the catalytic activity

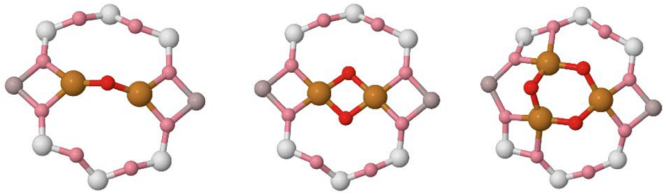

Figure 2.14: mono-(μ-oxo)-dicopper (left), bis-(μ-oxo)-dicopper (centre), and tricopper (right) clusters in copper zeolites. Reprinted from Reference [5]

of Cu-exchanged zeolites for dMtMc.[7, 10, 13] Despite thoroughly debated, the precise active site remains unresolved. However, regardless of their precise configuration, Cu-oxo motifs of the type Cu-O-Cu are believed to play a crucial role in CH_4 activation. Moreover, the reaction is believed to occur thanks to electron transfer promoted by these multi-cooper sites as follows: electron density from oxygen π-orbitals on oxo ligands flows into empty or partially filled metal orbitals; this electron donation from O to Cu increases the oxidation potential of the metal centre by stabilising Cu(II) state while simultaneously introducing radical character on the bridging oxygen ligand, essential for the hydrogen abstraction (homolytic C-H activation). [4–10, 12, 13, 15, 17, 19, 22, 25] Moreover, Cu redox couples are able to perform electron self-exchange, in which an electron is exchanged between two Cu centers in different oxidation states (Fig. 2.15). The reversible process between

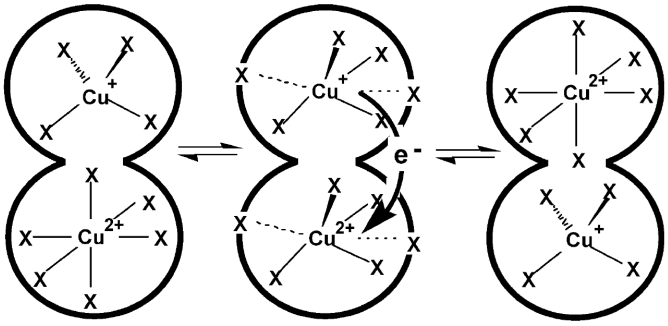

Figure 2.15: Schematic diagram of outer-sphere reactions as normally conceived for a single-step electron-transfer process showing the reorganization of the inner-sphere coordination geometry in a Cu(II)-Cu(I) self-exchange process. Adapted from Reference [53]

Cu(II) and Cu(I) species can be described follows:

$$*Cu^{II} + Cu^{I} \overset{k}{\rightleftharpoons} *Cu^{I} + Cu^{II} \tag{2.4}$$

In which the asterisk denotes the site in which the redox event is being observed. Notably, this process does not dependent on thermodynamics, since the overall Gibbs free energy change for the self-exchange process is zero ($\Delta G^\circ = 0$).[50, 53] In Cu-oxo species such as $[CuOCu]^{2+}$, ligand-metal charge transfer also enhances metal–metal exchange, increasing the de-localisation of spin density and improving the stability of multiple electron redox intermediates. [13, 15, 16, 50, 53]

2.5 The Catalytic Mechanism

The conversion of CH_4 into CH_3OH over Cu-exchanged zeolites proceed through a multistep redox-mediated mechanism that reflects a cascade of interconnected phenomena rooted in the unique physicochemical properties of Cu species confined in the zeolitic frameworks. Theses steps include: (i) O_2 activation; (ii) C-H bond activation; (iii) reorganisation and rebound mechanisms; and (iv) CH_3OH desorption and site regeneration (Fig. 2.16).[5, 7, 8, 11, 19, 21] Each of these steps is shaped by the local coordination geometry, redox potential, spin configuration, and ligand field environment of the Cu active site, parameters that, as previously shown, are strongly modulated by the structural topology and composition of the host zeolite. Thus, to fully comprehend how these mechanistic steps unfold at molecular level, one must consider not only the structural identity of the Cu-oxo intermediates, but also the electronic environment in which they operate.[15, 23, 24, 42, 43, 47]

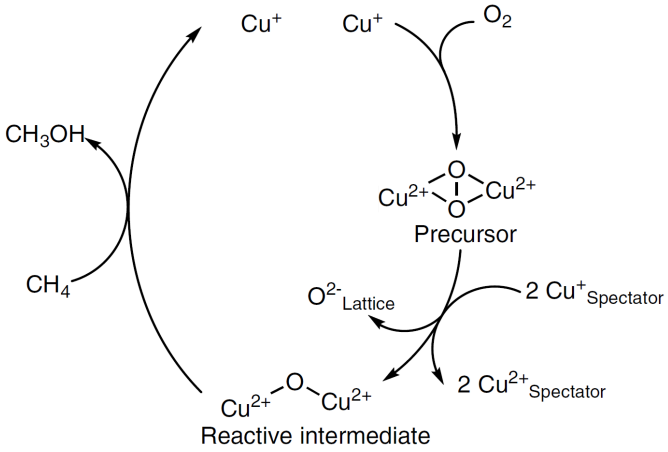

Figure 2.16: Proposed reaction cycle for O_2 activation and CH_4 hydroxylation by copper zeolites. Reprinted from Reference [5]

It all begins with the oxidation of Cu^+ ions, forming an O^2 adduct. In an idealised activation step, two adjacent Cu^+ ions co-operatively bind molecular oxygen, forming a $[Cu(O_2)Cu]^{2+}$ complex (Eq. 2.5), which is a peroxo dicopper intermediate. This step involves a structural rearrangement and ligand-to-metal charge transfer in which electron density from Cu^+ is transferred into the anti-bonding $\pi*$-orbitals of

O_2, oxidising both Cu^+ centres to Cu^{2+} whilst destabilising the O_2 moiety, instantly imposing the rupture of the O-O bond. This may result in either a planar or slightly distorted dimer bridged by two μ-oxo ligands, the $[Cu_2O_2]^{2+}$ complex named bis-(μ-oxo)-dicopper. Further reorganisation and oxygen migration result in several Cu species, including the $[CuOCu]^{2+}$ complex named mono-(μ-oxo)-dicopper (Eq. 2.6). Such configuration enhances orbital overlap between Cu centres and the bridging O atoms, promoting strong spin coupling and, consequently, resulting in a triplet ground state ($S = 1$).[5, 8, 10, 15, 24]

The most important step in the catalytic cycle is the activation of C-H bond in CH_4. In this step, the bridging oxo ligand in the $[CuOCu]^{2+}$ cluster abstracts a hydrogen atom from CH_4, resulting in the formation of a surface-bound hydroxyl group and a methyl radical (Eq. 2.7). This process proceeds through a radical-like transition state and is widely recognised as the highest energy barrier in the entire catalytic sequence.[10] The efficiency of HAA is highly sensitive to the electronic configuration of the Cu–oxo cluster, specifically its spin state and frontier orbital alignment. In binuclear Cu-oxo species, spin coupling between the two Cu centres is governed by the their exchange interaction, which depends on the Cu–Cu distance, the geometry of the bridging ligand, and, ultimately, the σ-interactions between e_g-orbitals through the bridge. Short Cu–Cu distances and strong μ-oxo bridges tend to promote antiferromagnetic coupling, yielding a singlet ground state (S = 0), where the two Cu^{2+} centres are anti-ferromagnetically coupled. In such configuration, the transition to a radical intermediate involves a spin-forbidden transformation, requiring inter-system crossing to access a triplet surface. This spin crossover introduces a significant entropic and enthalpic penalty, reducing reactivity. In contrast, the triplet ground state, characterised by a partially delocalised radical density on the oxo ligands, exhibit spin-allowed coupling with the radical character of the transition state. This facilitates efficient charge transfer from σ(C–H) to Cu-O LUMO, resulting in lower HAA barriers, consequently enabling higher turnover rates and more favourable kinetics. [5, 8, 10, 15–17, 24, 50]

Once formed, the methyl radical remains confined within the microporous environment of the zeolite and can rapidly undergo radical rebound with a nearby Cu–OH radical species, forming CH_3OH. This rebound mechanism involves coupling of the methyl radical with the hydroxyl group generated during HAA, and it proceeds via a spin-allowed, orbital-controlled recombination (Eq. 2.8). The success of this step is critically dependent on the spatial proximity of the reactive intermediates, which is promoted by the geometry and confinement effects of the zeolite framework.[5, 8–10, 13, 24] Within the constrained pore system, radical diffusion is minimised, and the orientation of the methyl radical relative to the Cu–OH orbital geometry promotes σ-overlap, increasing the rate and selectivity of CH_3OH forma-

tion. DFT studies support that this rebound step is barrier-less or has a very low activation energy under ideal geometries, provided that the reaction occurs in confined environments such as MOR side pockets or ZSM-5 straight channels.[8, 10, 24]

The resulting CH_3OH molecule is typically weakly coordinated to the Cu centre via a lone pair on the oxygen. Its desorption can be induced by competitive adsorption of water, thermal activation, or introduction of some other polar specie, which displace CH_3OH from the coordination sphere. After CH_3OH formation and desorption, the Cu active centres are typically left in a reduced state, often as Cu^+, completing the two-electron redox cycle (Eq. 2.9). These Cu^+ sites can then be reactivated via exposure to an oxidant, generally O_2, N_2O, H_2O_2 or even controlled steam, regenerating the Cu–oxo species and allowing for subsequent turnovers.[5, 8, 10, 11] In this stepwise catalytic mechanism, the cyclical re-oxidation is central in allowing the partial, selective oxidation of CH_4. Moreover, since over-oxidation products such as CO or CO_2 can form if the Cu–oxo species exhibit excessive electrophilicity, or CH_3OH is not sufficiently rapidly desorbed, allowing it to remain in contact with active oxidants, an effective catalyst design must necessarily strike a perfect balance in which sufficient redox potential for effective C–H activation is achieved, oxidising strength is enough to allow for the redox cycle to occur, but moderate enough in order to prevent deep oxidation. Additionally, the confined environment must allow a rapid desorption and diffusion of products, while preventing diffusion of intermediates.[5, 8–10, 13, 24] The overall catalytic cycle can be summarised as:

$$Cu^+ + Cu^+ + O_2 \rightarrow [Cu_2(O_2)]^{2+} \tag{2.5}$$

$$[Cu_2(O_2)]^{2+} \rightarrow [\text{Cu-O-Cu}]^{2+} + O^{2-} \tag{2.6}$$

$$[\text{Cu-O-Cu}]^{2+} + CH_4 \rightarrow [\text{Cu}-\cdot\,\text{OH}\cdots\text{Cu}]^{2+} + \cdot CH_3 \tag{2.7}$$

$$[\text{Cu}-\cdot\,\text{OH}\cdots\text{Cu}]^{2+} + \cdot CH_3 \rightarrow [\text{Cu}\cdots\text{OHCH}_3\cdots\text{Cu}]^{2+} \tag{2.8}$$

$$[\text{Cu}\cdots\text{OHCH}_3\cdots\text{Cu}]^{2+} + H_2O \rightarrow 2Cu^+ + CH_3OH \tag{2.9}$$

The kinetics and thermodynamics of each step in the MtM catalytic cycle have been extensively quantified through computational studies. DFT simulations consistently report that the activation energy for C–H bond cleavage by the mono-(μ-oxo)-dicopper, $[CuOCu]^{2+}$ (typical Cu-Cu distance ranging from 2.8Å to 3.1 Å), typically between 70 kJ/mol and 90 kJ/mol, depending on parameters such as the Cu–Cu distance, the orientation of bridging oxo ligands, and the zeolite framework topology. In contrast, species such as $[CuOOCu]^{2+}$, $[CuOH]^+$ or $[CuO]^+$ (in which Cu-Cu distance are larger than 3.5 Å) generally exhibit higher barriers, exceeding 100 kJ/mol, making them less efficient C–H activators under comparable conditions (Fig. 2.17).[7, 9, 10, 15] These computational results support the hypothesis that zeolite frameworks with low Si/Al, which statistically favour the formation of Al–Al

pairs, and thus binuclear Cu sites, should exhibit enhanced catalytic performance through both thermodynamic stabilisation and kinetic advantage.[10, 14]

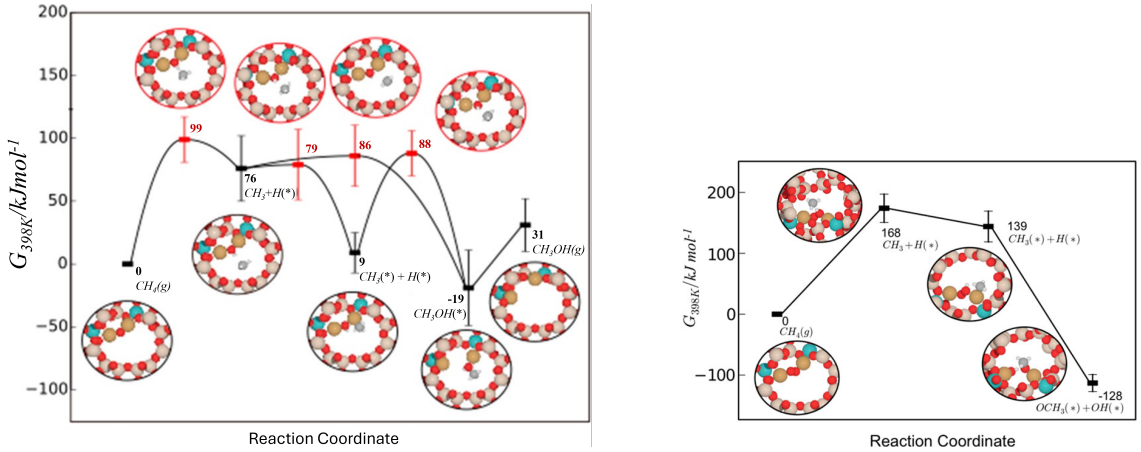

Figure 2.17: (a) Free energy profile and corresponding intermediates and transition state structures of methane conversion to methanol catalysed by CuOCu within the mordenite framework. The red line corresponds to the direct formation of methanol from CH_3 and OH. All energies are relative to gas-phase methane and the CuOCu motif. Error bars are obtained using the BEEF-vdW ensemble of exchange correlation functionals. Spin states of the intermediates and transition states are as follows: CH_3 + H*, triplet, CH_3* + H*, singlet; CH_3OH*, singlet; TS@99, triplet; TS@79, triplet; TS@86, singlet; TS@88, singlet. (b) Free energy profile and corresponding intermediates during CH_4 activation catalyzed by CuOOCu. Spin states of the intermediates and transition states are as follows: CH_3 + H*, triplet; CH_3* + H*, singlet; OCH_3* + OH*, triplet. Adapted from Reference [10]

It is important to note that the reaction mechanism is dynamic, rather than static. In real life scenarios, specially under transient reaction conditions, a distribution of Cu species coexist within the zeolite framework. These include mononuclear Cu^+/Cu^{2+} sites, binuclear Cu–oxo dimers, hydrated Cu–OH species, among other, each contributing to the overall reactivity with different turnover rates, redox cycling behaviour, and selectivity profiles. As a result, the catalyst often oscillates between multiple resting states, especially during pulsed reaction or stepwise operation modes. Under steady-state conditions, it is common that only a fraction of the total Cu content is catalytically active at any given moment, with the remainder existing in spectator configurations or structurally inactive states.[8, 10, 15, 24]

2.6 Final Considerations

This chapter has shown that the formation and catalytic function of Cu–oxo clusters cannot be decoupled from the environment in which they are effectively formed. The zeolitic framework intrinsically defines how Cu species will exist, by affecting

their own coordination, whether it will engage in efficient LMCT, and whether it will stabilise the desired intermediate and product species, like CH_3 or CH_3OH, without over-oxidation. Thus, these local phenomena are intrinsically linked to the dMtMc catalytic cycle, wherein catalytic activation, HAA, CH_3 rebound, and CH_3OH desorption, upon their activation energies, are each governed by the precise electronic structure of the active site, itself a function of global material properties. In that sense, the application of the Sabatier principle must be recontextualised. Here, the idea of "intermediate binding strength" must account not only for the adsorption energies but also to redox potentials, site nuclearity, and framework-induced electronic distortions. The emergence of volcano-like trends in activity as a function of Si/Al, or eventually some other descriptors, would reflect the multidimensional compromise that a successful dMtMc catalyst must embody: strong enough to activate C–H bonds, weak enough to release methanol; redox-flexible but not over-oxidising; spatially constrained yet sufficiently open for diffusion and turnover.

Chapter 3

Methodology

3.1 Material Preparation

The modification of the mordenite (MOR) zeolite, initially synthesised by LAB PEMOL/UFRN following the IZA protocol, was carried out using a sequential adaptation of various top-down methodologies reported in the literature.[14, 45, 55] The full methodology involved a systematic approach consisting of stages of ion exchange and dealumination, each step carefully designed to control the Si/Al and the catalytic properties of the final material.

The first modification step involved ion exchange of the original sodium MOR (Na-MOR) with ammonium chloride (NH_4Cl), following the methodology described by Katada et al. A 1 mol/L NH_4Cl solution was selected based on precedent literature, as it provides an efficient exchange of Na^+ ions while preserving the zeolite structure. The exact volume of solution required was calculated considering a theoretical Si/Al ratio of 6, a value initially provided by LAB PEMOL and subsequently validated by NMR analysis. Given a theoretical composition of [Si6AlO14]Na, corresponding to a molar mass of approximately 442.5 g/mol, the total amount of Na^+ in 10 g of dry Na-MOR was estimated at 0.0226 mols. Based on a literature-reported NH_4^+/Na^+ minimum operational ratio of 10:1, a minimum solution volume of 226 mL was determined for effective ion exchange.[55]

The ion exchange process began with the preparation of the NH_4Cl solution, achieved by dissolving an appropriate amount of NH_4Cl (99.8%, VETEC, batch 0502981) in deionised water to achieve the required concentration. The solution was then heated under continuous stirring (non-controlled) to 333 K in a Teflon beaker, where the temperature was monitored and stabilised. Once the desired temperature was reached, 10 g of dry Na-MOR were slowly added to the solution. The ion exchange was allowed to proceed for 120 min, ensuring sufficient time for the replacement of Na^+ ions with NH_4^+. After this period, the sample was centrifuged

at 3,000 rpm for 10 min, followed by three washing cycles with deionised water to remove residual salts. The ion exchange process was repeated three times to maximise NH_4^+ incorporation. After the final exchange cycle, the sample was filtered and dried at 393 K for 720 min (overnight). The dried material was then subjected to thermal treatment at 823 K for 240 min, with a heating rate of 4 K/min under a synthetic air flow of 100 $cm^3/min\ g_{material}$ to convert NH_4-MOR into its protonic form (H-MOR).

Subsequent dealumination of H-MOR was performed following the methodology reported by Giudici et al., using oxalic acid (99%, Sigma-Aldrich, batch BCCF8765) as the leaching agent. The 2 mol/L oxalic acid solution was selected based on Giudici's report, ensuring an effective reduction of the Al content while maintaining structural integrity in a controlled pace. The Si/Al modification was controlled by varying the contact time between the zeolite and the acid solution. Specifically, aliquots of approximately 1.2 g of H-MOR were subjected to acid leaching in 40 mL of 2 mol/L oxalic acid solution under reflux conditions.[45] The reflux treatment was conducted at five distinct time intervals: 10 min, 50 min, 100 min, 200 min, and 360 min, leading to the preparation of five different degrees of dealumination and resulting in five distinct Si/Al ratios.

Following the acid treatment, the samples were quenched to terminate the leaching process and extensively washed with deionised water until a neutral pH was achieved in the residual solution. The washed samples were filtered and dried at 393 K for 720 min (overnight). Subsequently, they underwent thermal treatment at 823 K for 300 min, with a 4 K/min heating ramp under synthetic air flow at 100 $cm^3/min\ g_{material}$ to remove residual organic species and stabilise the structure. These samples were designated H-MORX, where X corresponds to the acid treatment duration, representing, in theory, different Si/Al values.

Following dealumination, the samples were subjected to a sodium exchange process using $NaNO_3$ (99%, Sigma-Aldrich, batch MKCM2006) to restore their sodium form (Na-MORX), which was necessary for subsequent copper ion exchange. This step involved exchanging the dealuminated samples in a 1 mol/L $NaNO_3$ solution, maintaining a solution-to-zeolite ratio of 10 mL/g at 350 K for 240 min.[14] The procedure was repeated three times, with intermediate washing steps after each exchange, followed by drying at 393 K for 720 min (overnight) and thermal treatment at 823 K for 240 min, with a 4 K/min heating rate under a synthetic air flow of 100 $cm^3/min\ g_{material}$.

The Cu-exchange step was performed using copper acetate ($Cu(OAc)_2$) solution, following the methodology described by Xie et al. The Na-containing zeolite precursors with different Si/Al (Na-MORX) were exchanged in a 0.01 mol/L $Cu(OAc)_2$ solution at room temperature for 1440 min. The amount of Cu^{2+} solution added

(volume) was calculated based on the Si/Al of each sample to ensure full exchange, targeting a Cu/Al ratio of 0.5. The ion exchange procedure was repeated three times, with thorough washing after each cycle using at least 4 L of deionised water to remove residual acetate ions.[14] After the third exchange cycle, the samples were dried at 373 K for 720 min (overnight) and subsequently subjected to thermal treatment at 823 K for 240 min, following the same 4 K/min heating ramp under synthetic air flow (100 $cm^3/min\ g_{material}$).

The final Cu-MOR catalysts obtained through this rigorous synthesis approach were systematically analysed to assess the effect of Si/Al on copper incorporation, ensuring a well-defined relationship between structural modification, active site formation and distribution, and catalytic performance. A limited set of preliminary studies was carried out using more readily available ZSM-5, with nominal Si/Al of 15, primarily to optimise experimental protocols and minimise material loss. This strategy allowed for calibration of modification protocols and experimental conditions before applying them to the more restricted MOR samples. Thus, only a minimal portion of these auxiliary results will be presented herein.

3.2 Material Characterisation

3.2.1 Thermogravimetric Analysis (TGA)

Since zeolites are hygroscopic materials, TGAs were conducted to quantify the amount of water present in the material at each stage of preparation. Additionally, these analyses were employed to detect any residual organic materials used during the dealumination process. The experiments were performed using a TA Instruments SDT Q600 thermogravimetric analyser. Approximately 10 mg of sample were heated from room temperature to 1273 K under a synthetic air flow of 100 $mL{\cdot}min^{-1}$, with a heating rate of 10 $K{\cdot}min^{-1}$, while monitoring mass variations throughout the process.[3, 24, 56]

3.2.2 X-Ray Diffractometry (XRD)

Crystallographic properties and crystalline phases of the samples were evaluated using XRD. The samples, in powdered form, were analysed using a Bruker D8 Advance diffractometer equipped with a Cu X-ray source (Cu-Kα, $\lambda = 1.5418$ Å). Data acquisition was performed over an angular scanning range of $20° \leq 2\theta \leq 90°$, with a step size of 0.05°. The obtained diffraction patterns were compared against the International Centre for Diffraction Data (JCPDS) database using the JADE software, along with crystallographic files available in the Powder Diffraction File (PDF) database. To ensure accurate phase identification, a secondary verification

was performed using the IZA database and the X'Pert HighScore Plus software, which was also employed for numerical evaluation of the material's crystallinity and purity. All profiles were submitted to data smoothing and and range from 5° to 50° for x-axis was chosen for better visualisation. Cristallite size was estimated from XRD data using the Scherrer equation (Eq. 3.1), which provides a quantitative link between diffraction peak broadening and the size of coherently diffracting domains within the material.

$$D = \frac{K\lambda}{\beta \cos\theta} \tag{3.1}$$

where D is the average crystallite size in nanometers (nm), K is the dimensionless shape factor, considered 0.9 for simplicity, λ is the wavelength of the incident X-rays, β is the full width at half maximum (FWHM) of the selected diffraction peak in radians, and θ is the Bragg angle θ in radians. For all samples, peaks at circa 9.8°, 13.5°, 22.3°, 25.7° and 27.8° were selected as the most relevant, according to reference material from cif file from IZA.[3, 24] Final value was estimated as the average of the values of all selected diffraction peaks.

Crystallinity was estimated following a qualitative approach, by comparing the integrated area under characteristic XRD peaks. In crystalline solids, diffraction peak intensity is proportional to the amount of long-range structural order present. Therefore, for samples sharing the same crystal structure, the relative crystallinity (C_r) can be estimated by integrating the area under selected reflections (Eq. 3.2).

$$C_r(\%) = \left(\frac{\int_{\theta_1}^{\theta_2} I_{sample}(\theta) \quad d\theta}{\int_{\theta_1}^{\theta_2} I_{ref}(\theta) \quad d\theta} \right) \times 100 \tag{3.2}$$

In order to evaluate an average behaviour, the relative crystallinities of several selected peaks (circa 9.8°, 13.5°, 22.3°, 25.7° and 27.8°) are computed using OriginPro software. The average of these values correspond to an overall crystallinity (Eq. 3.3).

$$C_{r,overall}(\%) = \frac{\sum_{i=1}^{n} \left(\frac{A_{sample}}{A_{ref}} \right)_i}{n} \times 100 \tag{3.3}$$

where A_{sample} is the integrated area of the selected peak i in the sample, and A_{ref} is the corresponding area in the Na-MOR reference. This method ensures consistent comparison across the series and minimises error propagation due to amorphous background or instrumental variation. As such, it provides a reliable estimation of the relative degree of structural order preserved through the various stages of ion exchange and dealumination.[3, 24]

3.2.3 X-Ray Fluorescence (XRF)

Approximate bulk chemical composition analysis of the samples was carried out using XRF spectroscopy, a widely employed semi-quantitative assessment of elemental composition in solid-state materials. The measurements were performed using a Rigaku Primini XRF spectrometer equipped with a Pd X-ray generation tube operating at 4 kW. To minimise experimental variability, a standardised protocol was followed, and measurements were performed three times on three different samplings of approximately 200 mg each.[3, 24, 56]

3.2.4 Nuclear Magnetic Resonance (NMR)

Solid-state NMR experiments for ^{27}Al and ^{29}Si magic-angle spinning (MAS) NMR, as well as ^{29}Si cross-polarisation magic-angle spinning (CPMAS) NMR, were conducted using BRUKER DRX-300 and AVANCE III 400 (9.4T) spectrometers. Samples were transferred into 4 mm and 7 mm ZrO_2 rotors, in accordance with internal analytical protocols following the specific requirements of each nucleus for spectral acquisition quality.[56] All experimental acquisition parameters are displayed in Tab. 3.1.

Table 3.1: Acquisition conditions for solid-state NMR analysis.

Acquisition Conditions	^{27}Al **MAS NMR**	^{29}Si **MAS NMR**	^{29}Si **CPMAS NMR**
Probe	4 mmf	7 mm	4 mmT
Sample Holder	ZrO_2; 4 mm, Kel-F cap	ZrO_2; 7 mm, Kel-F cap	ZrO_2; 4 mm, Kel-F cap
Spinning Speed (Hz)	12,000	5,000	5,000
Pulse Sequence	Direct Polarisation	Direct Polarisation	Cross Polarisation
Recycle Delay (s)	0.5	60	4
Number of Scans	4k (4096 scans)	256 scans	4k (4096 scans)
Acquisition Time	36 min 26 s	4 h 16 min	4 h 32 min
Reference (ppm)	1M $AlCl_3{\cdot}6H_2O$ 0.0 ppm	Kaolinite -91.5 ppm	Kaolinite -91.5

3.2.5 N_2 Physisorption

Textural properties of the samples in all stages were evaluated through N_2 physisorption measurements conducted using a Micromeritics ASAP2020 adsorption analyser. Approximately 200 mg (measured prior to pretreatment) of sample was used in each analysis. Prior to the measurement, the samples underwent a pretreatment process at 423 K under vacuum for 14 h to ensure the removal of absorbed water (moisture). Adsorption–desorption isotherms were recorded by measuring the amount of N_2 adsorbed as a function of relative pressure (p/p_0).

The Brunauer-Emmett-Teller (BET) model (Eq. 3.4) is commonly employed for determining specific surface area.

$$\frac{p/p_0}{V(1-p/p_0)} = \frac{1}{V_m C} + \frac{C-1}{V_m C} \cdot \frac{p}{p_0} \tag{3.4}$$

where V is the volume adsorbed at relative pressure p/p_0, V_m is the monolayer capacity, and C is the BET constant related to the adsorption enthalpy.

The BET model is based on multilayer adsorption assumptions, which often fail for microporous materials such as zeolites. These materials typically lack significant multilayer formation. As a result, the BET equation may yield non-physical results. This issue can be assessed by a negative (or very low) value of the C constant, which indicates poor applicability of the model.

In case the BET model fails, the Langmuir model (Eq. 3.5) can be used instead. This model assumes monolayer adsorption onto a finite number of energetically equivalent sites, which is more appropriate for microporous frameworks.

$$\frac{1}{V} = \frac{1}{V_m K} \cdot \frac{1}{p/p_0} + \frac{1}{V_m} \tag{3.5}$$

where K is the Langmuir equilibrium constant and V_m is again the monolayer capacity.

The specific surface area S can be calculated from the Langmuir-derived monolayer volume V_m (Eq. 3.6).

$$S = \frac{V_m N_A \sigma}{V_m^{\text{gas}}} \tag{3.6}$$

where N_A is Avogadro's number, $\sigma = 0.162$ nm^2 is the molecular cross-sectional area of N_2, and $V_m^{\text{gas}} = 22\,414$ cm^3/mol is the molar volume of N_2 at standard temperature and pressure (STP), 273.15 K and 1 atm (101.325 kPa).[3, 24]

The De Boer method (t-plot method) was used to evaluate both the micropore surface area and the external surface area of the samples. This method relies on the statistical thickness of the adsorbed N_2 layer (t) as a function of p/p_0, using a standard reference isotherm for nonporous surfaces. The values for t (nm) are

estimated using the Harkins–Jura equation (Eq. 3.7).

$$t = 0.1 \left(\frac{13.99}{0.034 - log(p/p_0)} \right)^{0.5} \tag{3.7}$$

By plotting the adsorbed volume V versus t, a linear region is obtained corresponding to multilayer adsorption on the external surface. The slope of this linear region provides the external surface area, while the y-intercept represents the micropore volume. This method is particularly effective for microporous materials, where deviations from linearity at low t values indicate pore filling rather than surface adsorption.

3.2.6 NH_3 Temperature-Programmed Desorption (NH_3-TPD)

NH_3-TPD was employed to evaluate the acidity of the zeolitic catalysts. The TPD experiments were conducted using a quartz U-shaped tubular reactor inside a furnace equipped with PID temperature control. Approximately 100 mg of catalyst were used in each experiment. Prior to the adsorption step, the catalyst was dried under a continuous flow of pure He (60 mL/min), ramped at 10 K/min up to 473 K, and held at this temperature for 1 h. NH_3 adsorption was performed by flowing a 4 %vol. NH_3 in He mixture (60 mL/min) over the catalyst for 30 min at 100 °C. This was followed by a purging step using pure He (60 mL/min) for approximately 1 h to remove weakly adsorbed NH_3. Subsequently, the desorption phase was initiated by heating the catalyst to 873 K at a rate of 20 K/min under a flow of pure He (60 mL/min). Desorbed NH_3 was monitored via a quadrupole QMS 422 Balzers-Pfeiffer mass spectrometer by tracking the ion current corresponding to m/z = 15, which is a characteristic fragment of ammonia. The desorption profiles were used to calculate the total amount of NH_3 desorbed, providing a quantitative measure of the acid site concentration in μmol/g. This was done using calibration-derived sensitivity factors and a known signal-to-area conversion model.[3, 24, 56]

3.2.7 CH_4 Temperature-Programmed Surface Reaction (CH_4-TPSR)

CH_4-TPSR was employed to evaluate the reactivity of zeolitic catalysts towards methane activation and to determine the onset temperature for CO_x formation. The TPSR experiments were conducted using a quartz U-shaped tubular reactor inside a furnace equipped with PID temperature control. Prior to the reaction step, each catalyst sample was subjected to oxidative pretreatment under a flow of pure O_2 (20 mL/min) at 823 K for 2 h, using a temperature ramp of 5 K/min.

This was followed by a cleaning step under pure He (20 mL/min) at 523 K for 30 min to remove any residual adsorbates. The TPSR procedure was initiated by flowing a 2 vol.% CH_4/He gas mixture (total flowrate of 100 mL/min) over the catalyst while increasing the temperature from ambient to 623 K at a rate of 10 K/min. The evolution of CO_2 was continuously monitored using quadrupole QMS 200 BALZERS mass spectrometer coupled to a CH-TRON QUADSTAR 422 system with an electron multiplier detector by tracking the ion current corresponding to m/z=44, which is a characteristic fragment of CO_2.[3, 24, 56]

3.2.8 UV-Visible Diffuse Reflectance Spectroscopy (UV-Vis DRS)

UV-Vis DRS was employed to investigate the coordination environment of Cu species in the samples. The measurements were carried out using a Varian Cary 5000 UV-Vis-NIR spectrophotometer. Spectra were recorded at room temperature over the wavelength range of 200 nm to 800 nm, covering both the ultraviolet and visible regions of the electromagnetic spectrum. Barium sulfate ($BaSO_4$) powder was used as the reference material for baseline correction, and the resulting absorbance data were normalised accordingly.[3, 24, 56]

3.3 Catalytic Experiment

The catalytic tests were designed taking into account and adapting procedures described in reliable existing literature stepwise protocols (Fig. 3.1)[6–8, 11, 48] to evaluate the performance of the material for the productivity of methanol under controlled conditions. The protocol followed a systematic sequence of activation, reaction, and analysis steps to ensure the reproducibility and reliability of the obtained results.

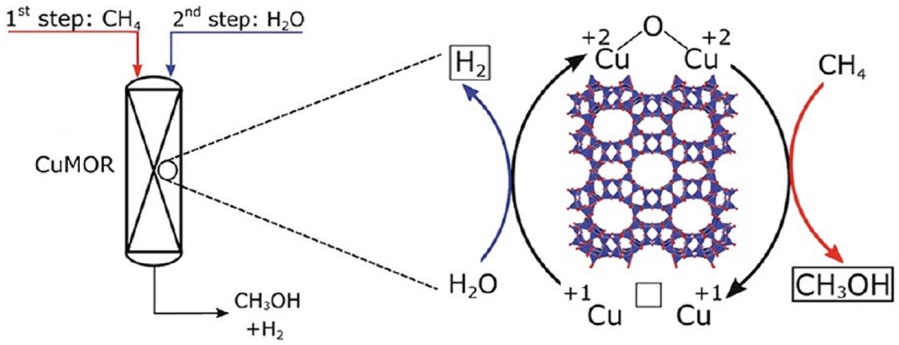

Figure 3.1: Simplified schematic representation of the dMtMc using water. Adapted from Reference [48]

The dMtMc reaction was performed on a quartz fixed bed tubular reactor coupled with a MKS-2030 Fourier Transform Infrared (FTIR) spectrometer.[56] The unit is equipped with gas lines to provide CH_4, N_2, and synthetic dry air, which acts as the oxidant due to the presence of oxygen.[5] Moreover, a humidifier cell and switchers allow for the addition of vapour to the system. For all runs the amount of catalyst was fixed as 150 mg.

The procedure began with the activation of the catalyst in a 20 mL/min synthetic dry air flow, and the temperature was gradually increased at a rate of 5 K/min until reaching 820 K.[6–8, 11] This temperature was maintained for 60 min to ensure complete oxidation of the material and stabilisation of the active sites. Controlled oxygen exposure at high temperatures is a crucial step for regenerating and activating Cu-exchanged zeolites, forming catalytically active oxo species.[5–8, 11, 13]

Following activation, the temperature was lowered to 473 K while maintaining the synthetic dry air flow to prevent thermal deactivation (through reduction).[6–8, 11] The choice of 473 K is based on literature[6–8, 11] and TPSR evaluation. Once the system stabilised at 473 K, the synthetic dry air flow was replaced with 20 mL/min of N_2 (inert) for 40 min, ensuring the removal of residual oxidant gas in the atmosphere to control and prevent unintended oxidative side reactions upon methane introduction.

To initiate the reaction phase, temperature was lowered to approximately 450 K, the optimal temperature for methane activation in the sample as verified by TPSR. At this point, the N_2 flow was replaced with a 20 mL/min CH_4 flow, and the catalyst was exposed to this condition for 60 min. The choice of 450 K as the reaction temperature is based on findings indicating that, at this range, partial methane oxidation to methanol occurs.

After methane exposure, the flow was switched back to N_2 gas while maintaining the temperature at 450 K. This step aims to flush unreacted methane and other species from the system, ensuring that the subsequent detection step is free from interferences. Since methanol yield is small and literature recognises that the formed species remain adsorbed to the catalyst, this step is believed not to interfere with the methanol quantity while cleaning the outlet flow.

Concomitantly with switching from CH_4 to N_2, the reactor outlet was directed to the analyser, where the chemical composition was monitored in real-time. Once CH_4 signal in the analyser stabilised at a baseline level, N_2 flow was replaced with a 20 mL/min 4% water vapour in N_2 flow.[24, 56] Water vapour is reported to promote methanol desorption from active sites in a controlled manner, stabilising the product and preventing further oxidation.[6–8, 11] An increase in the methanol signal at this stage confirmed the effectiveness of the implemented reactional and detection protocols.

The reaction was monitored until the methanol signal returned to a constant baseline, indicating the completion of product desorption.[56] The reactor was then purged with dry N_2 flow at 450 K for 30 min to dry the sample and the system, allowing for cleaning. Finally, the analyser was shut down, and temperature was gradually reduced to room temperature, concluding the experiment.

The quantification of gas species was performed by integrating the FTIR signal over time using OriginPro software, yielding a value proportional to the amount of analyte released during the experimental catalytical procedure. This integrated signal, expressed in arbitrary units (a.u.), is applied to appropriate calibration factor, k, specific to each gas species, which correlates the raw signal to concentration in ppm. Assuming ideal gas behaviour, it is possible to compute the total number of moles (Eq. 3.8) using the ideal gas law.

$$n_{\text{mol}} = \frac{P}{RT} \cdot Q \cdot k \cdot \text{AUC} \tag{3.8}$$

where n_{mol} is the total number of moles of the detected gas specie, P is the pressure during the measurement, T is the absolute temperature, R is the universal gas constant, Q is the total volumetric gas flow rate, k is the calibration factor, and AUC is the area under the FTIR signal versus time curve. All those should be in appropriate units according to provided calibration.

Finally, the FTIR raw signals we statistically treated using the Seaborn package in Python, using the average method to generate a heat map. The same dataset was subjected to principal component analysis (PCA) using the scikit-learn library to reduce data dimensionality by selecting data sets (analysed gas species) with best correlations factors across all samples. The combination of both information allow for qualitative identification of compositional trends across the evaluated samples.

Chapter 4

Results and Discussion

4.1 Chemical Composition

The ^{27}Al MAS NMR spectra of Na-MOR showed a single sharp peak at 55.9 ppm, indicating that all Al was present as tetrahedrally coordinated framework Al (Al^{VI}).[57–60] No signals in the 0 ppm to 10 ppm range were detected, confirming the absence of extra-framework Al^{IV} species and suggesting that the sample retained structural integrity.[57–60] ^{29}Si MAS NMR spectra of Na-MOR was analysed via both direct integration and deconvolution. Signals corresponding to Q^4(3Al), Q^4(2Al), Q^4(1Al), and Q^4(0Al) were clearly observed (Fig. 4.1). The dominant contribution came from Q^4(1Al) at circa -105.6 ppm. Both analytical methods yielded consistent estimates for the Si/Al molar ratio of 4.6. Additionally, the signal separation and sharpness, along with the absence of significant line broadening or additional peaks, are indicative of a well-defined, relatively ordered, crystalline framework with minimal amorphisation or defect-induced broadening.[57–60]

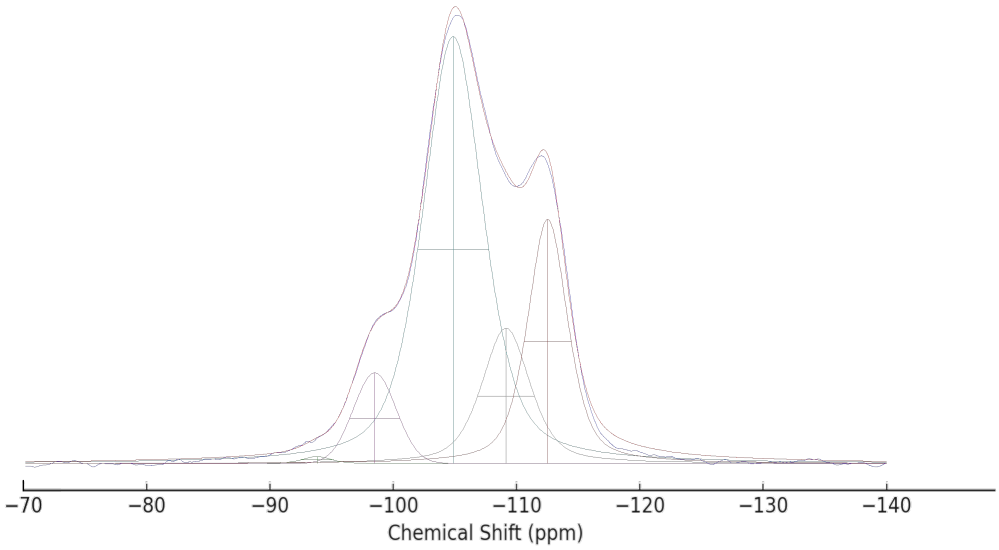

Figure 4.1: ^{29}Si MAS NMR spectra of Na-MOR

Additionally, two ZSM-5 samples with slightly different nominal Si/Al were examined to be used as comparative parameter for XRF values. The ^{27}Al MAS NMR spectra ZSM5-1 showed a single sharp peak at 56.8 ppm, corresponding exclusively to framework Al^{IV}.[57–60] On the other hand, ZSM5-0 displayed a main sharp peak at 56.1 ppm, but also a small peak at 1.3 ppm, which accounted for 9.7 % of the total signal area. This latter resonance is characteristic of octahedrally coordinated, extra-framework Al (Al^{VI}).[57–60] Regarding the ^{29}Si MAS NMR spectra, both samples showed signals around −106 ppm and −112 to −116 ppm, associated with Q^4(1Al) and Q^4(0Al) sites, respectively (Figs. 4.2 and 4.3).[57–60] The Si/Al was calculated at 16.0 for ZSM5-1, and 17.3 for ZSM5-0. Deconvolution revealed that the ZSM5-0 sample required two Gaussian components in the Q^4(0Al) region, probably reflecting the presence of distinct siliceous domains or varied local crystallinity.[57–60] Therefore, ^{29}Si CPMAS spectrum was acquired for ZSM5-0 to probe for the presence of silanol (Si-OH) groups. The enhanced signal intensity around −105 ppm in the CP spectrum, compared to the direct MAS spectrum, confirmed the presence of such defects. These Si-OH sites frequently reside near framework vacancies or distorted regions.[3, 24, 39, 57–60]

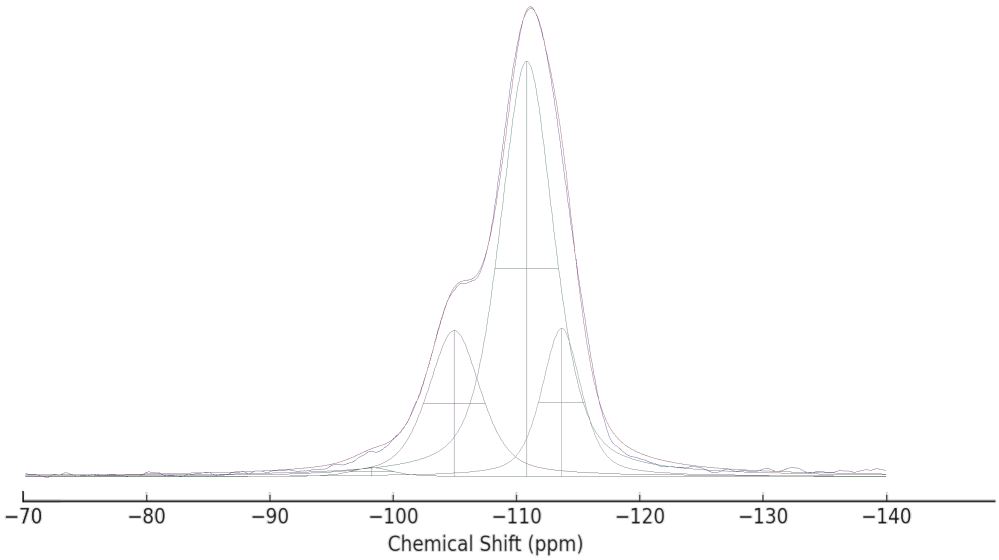

Figure 4.2: ^{29}Si MAS NMR spectra of ZMS5-1

Given the higher resolution and reliability of NMR analysis of zeolites for Si/Al determination, NMR acquired Si/Al values were used as a reference to calibrate the less accurate XRF acquired values. The parent samples Na-MOR and ZSM5-0 were both analysed in XRF, resulting in Si/Al values of 7 and 19 respectively. These values were compared to their corresponding NMR determined Si/Al of 4.6, for Na-MOR, and 17.3, ZSM5-0. Assuming a linear correlation between the two techniques, a calibration model was constructed by fitting the known Si/Al_{NMR}

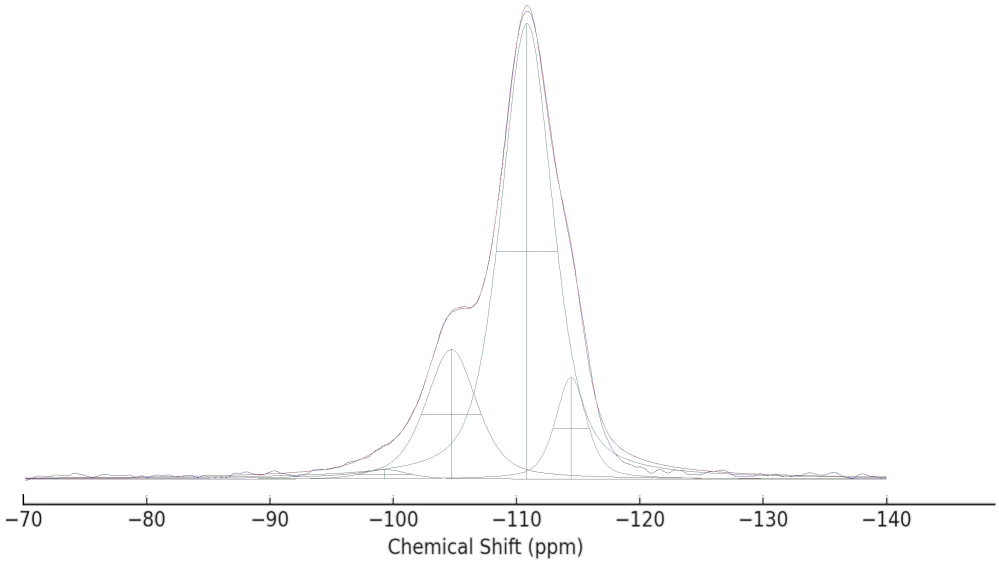

Figure 4.3: ^{29}Si MAS NMR spectra of ZSM5-0

values as a function of Si/Al$_{XRF}$. This resulted in the empirical correction equation $Si/Al_{NMR} = 1.058\ Si/Al_{XRF} - 2.808$, which accounts for the observed deviation in Si/Al values from XRF, compared to NMR. Considering that such behaviour in implicit to the XRF analysis and that a more accurate value is that obtained by NMR, a correction factor $Si/Al_{corrected} = 1.058\ Si/Al_{XRF} - 2.808$ was applied for all sample.

The results for chemical composition of Cu-MORx are displayed in Tab. 4.1. Corrected values calculated though applied model are also displayed. Such results confirm the effectiveness of the applied dealumination protocol.[45]

Table 4.1: XRF analysis.

Sample	**Molar fraction Si** / %	**Molar fraction Al** / %	**Molar fraction Cu** / %	**Calculated Si/Al$_{XRF}$**	**Si/Al$_{corrected}$**
Cu-MOR010	86.98	10.03	2.89	8.7	6.4
Cu-MOR050	89.75	7.97	2.06	11.3	9.1
Cu-MOR100	91.26	6.89	1.67	13.2	11.2
Cu-MOR200	92.99	5.42	1.19	17.2	15.3
Cu-MOR360	93.91	5.16	0.87	18.2	16.4

4.2 Crystalline Phases

XRD was employed to evaluate the structural integrity, long-range order, and crystallite size evolution on samples. Analysed samples includes the parent Na-MOR, ion-exchanged H-MOR, acid-treated derivatives (MOR000 to MOR360), and finally their corresponding Cu-exchanged forms (Cu-MOR000 to Cu-MOR360). Crystallinity values and estimated crystallite sizes are shown in Tab. 4.2.

Table 4.2: Calculated crystallinity and crystallite size for the Na-MOR, H-MOR, MORx, and Cu-MORx series.

Sample	**Crystallinity** / %	**Crystallite size** / nm
Na-MOR	100	595
H-MOR	85	580
MOR000	70	665
MOR010	75	535
MOR050	80	310
MOR100	85	275
MOR200	65	380
MOR360	55	615
Cu-MOR000	80	615
Cu-MOR010	95	515
Cu-MOR050	120	325
Cu-MOR100	110	255
Cu-MOR200	70	375
Cu-MOR360	60	595

The parent Na-MOR sample serves as the reference material. Its diffraction pattern (Fig. 4.4) exhibits well-resolved, sharp reflections throughout the 5°—90° 2θ range, indicating high long-range periodicity and minimal disorder, which is also corroborated by NMR. The calculated crystallite size is 600 nm, reflecting large, coherent domains. Across all samples, the main reference peaks are observed with no significant shifts in positions, indicating that unit cell dimensions remained basically constant. This implies that dealumination and ion exchange modify the framework composition and local environment but do not significantly induce strains on the lattice.[3, 24, 39]

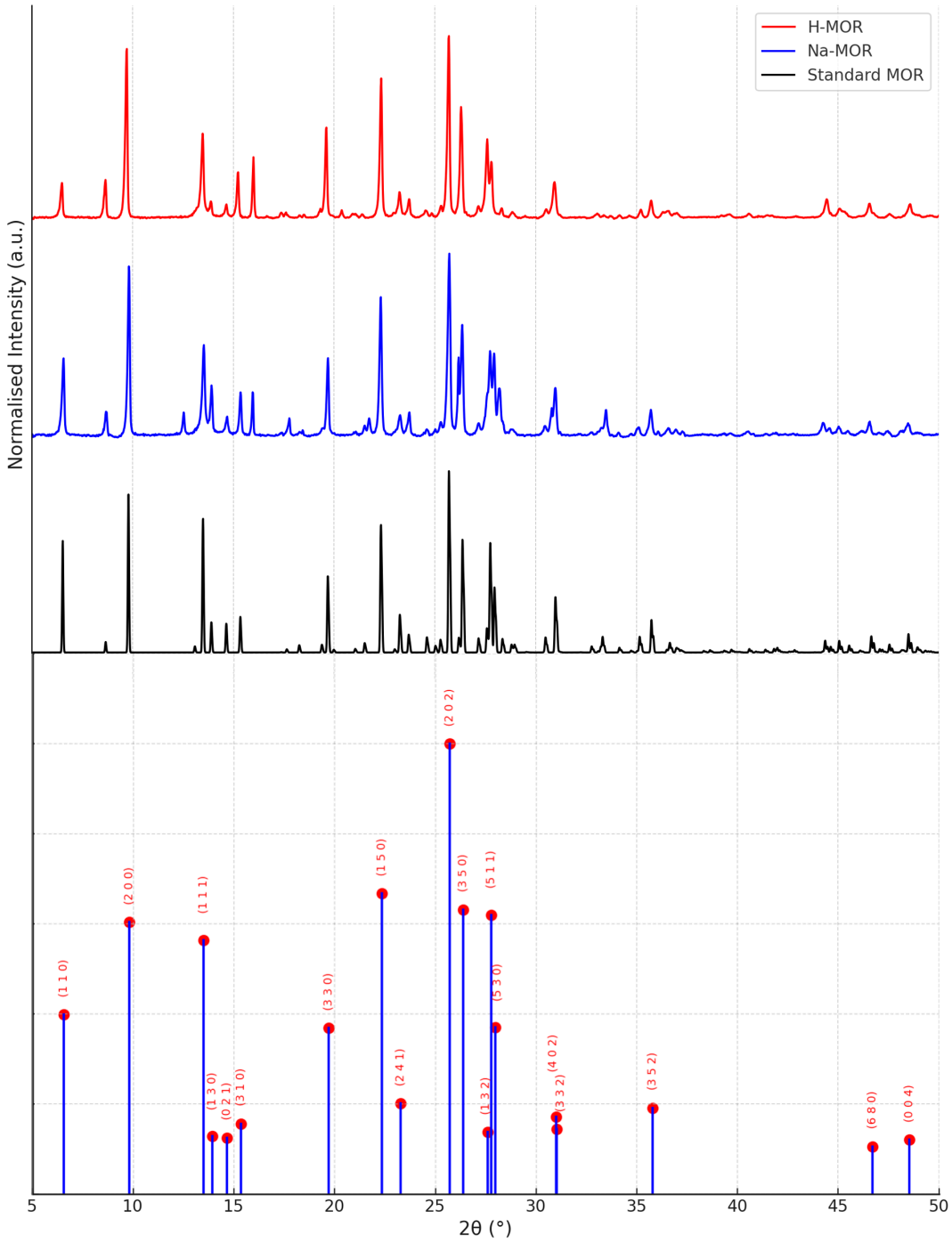

Figure 4.4: XRD profiles for parent Na-MOR and ion-exchanged H-MOR. Standard MOR profile and crystallographic planes according to IZA[61]

H-MOR displays only minor reductions in crystallinity, calculated at about 85 %, compared to Na-MOR parent sample, used as reference (Fig. 4.5). The preservation

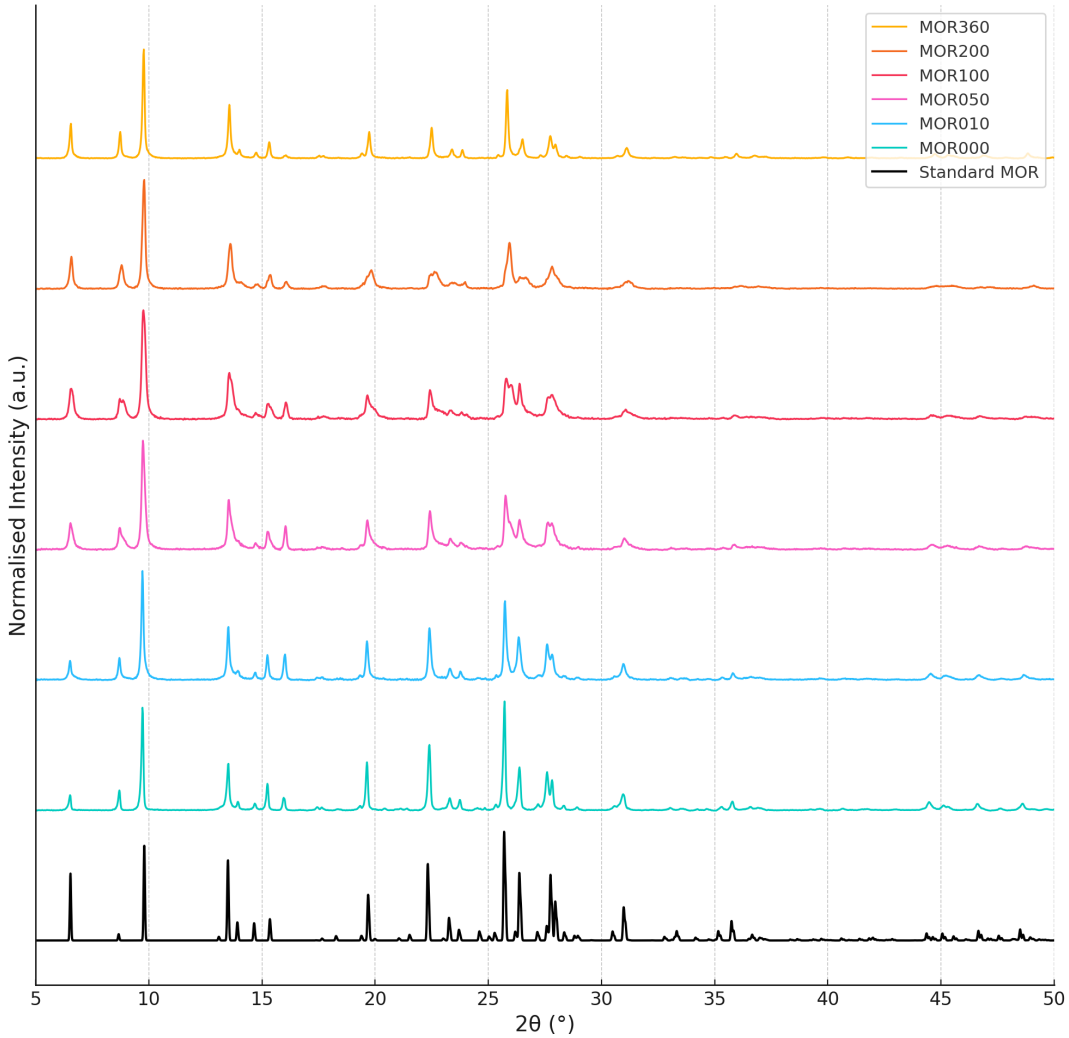

Figure 4.5: XRD profiles for acid treated MOR000, MOR010, MOR050, MOR100, MOR200 and MOR360.

of peak positions and minimal broadening suggest that NH_3 exchange and thermal conversion to the protonated form cause negligible framework degradation. This indicates that the ion exchange process did not introduce significant framework changes, nor introduced defects neither trigger framework hydrolysis.[3, 24, 39] Regarding the acid treated samples, MOR000 (subjected to extremely fast acid contact only), exhibits a pronounced drop in crystallinity, to a calculated value of 70 % compared to Na-MOR. Interestingly, real dealumination stages (MOR010, MOR050, and MOR100) exhibit a progressive increase in relative crystallinity, from 75 % to 85 %. This counter-intuitive effect is related to the fact that mild dealumination can eliminate extra-framework remains and other poorly ordered domains, thereby enhancing the crystallinity indexes in the XRD pattern. However, more aggressive acid exposure, on samples MOR200 and, especially, MOR360, do show smaller levels

of crystallinity, calculated as 65 % and 55 % respectively. This decline reflects the onset of structural degradation, likely due to hydrolytic cleavage of T–O–T bonds as framework aluminium is extensively removed.[45] Overall broadening and intensity reduction observed for most peaks in these samples are consistent with the formation of amorphous regions or, most probably, defect-rich domains.[3, 24] Crystallite size analysis further support these interpretations. Sizes decrease steadly from MOR000 to MOR100, reflecting growing internal amount of defects, reaching a minimum of 275 nm for MOR100. MOR200 and MOR360 exhibit values of 380 nm and 615 nm respectively, which may point to framework reorganisation or densification of remaining crystalline regions under prolonged treatment. This suggests the formation of fewer but larger coherent domains, possibly due to the collapse and reordering of small fragments. These findings are coherent with literature.[24, 45]

For the Cu-MOR samples (Fig. 4.6), an increase in crystallinity, compared to parent MORx, is observed. This result does not necessarily imply a real higher

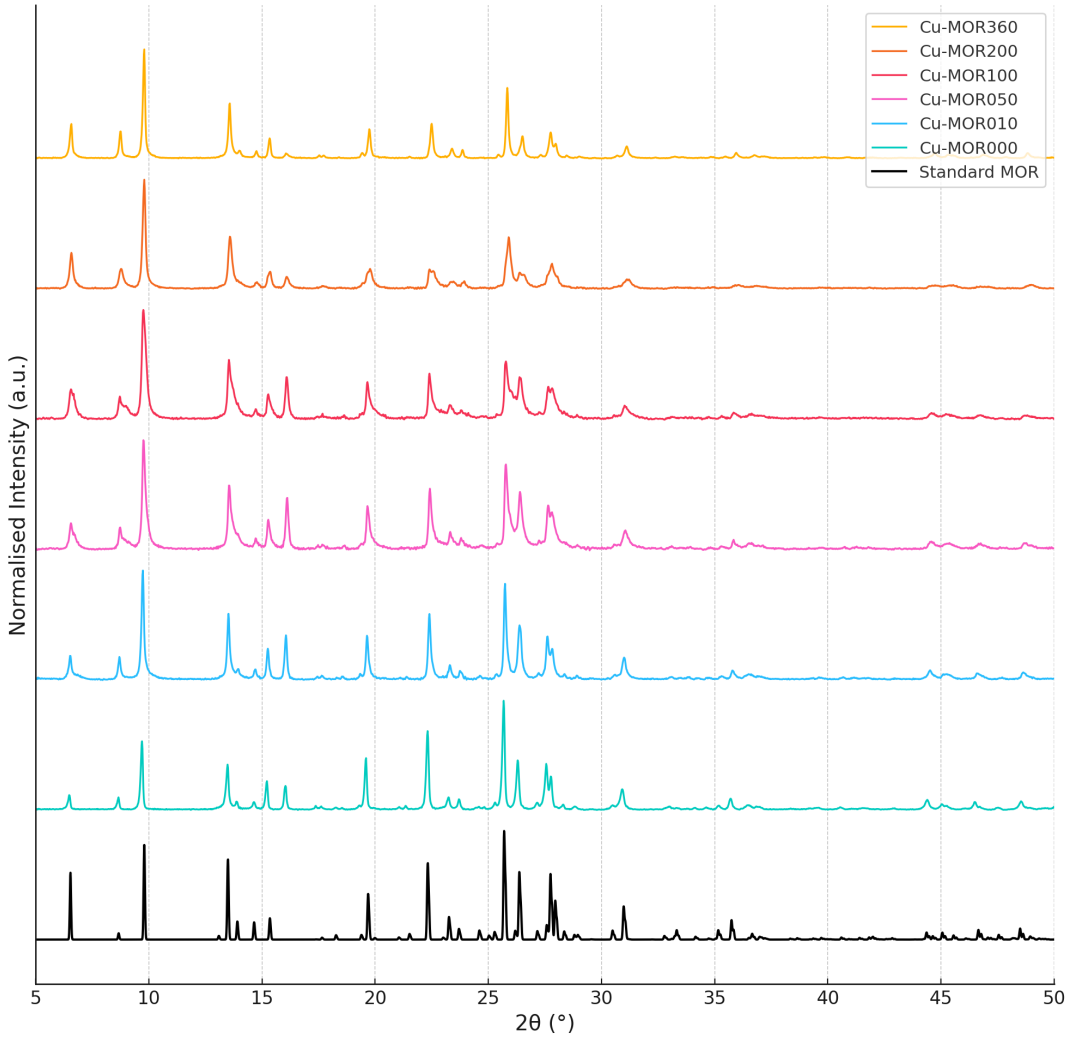

Figure 4.6: XRD profiles for Cu-exchanged samples Cu-MOR000, Cu-MOR010, Cu-MOR050, Cu-MOR100, Cu-MOR200 and Cu-MOR360.

degree of structural order; instead, it is likely due to the efficient removal of residual disordered and amorphous material or even only by a greater scattering factor induced by Cu.[3, 24, 55] However, Cu bridging could provide local structure stabilisation.[3, 15, 24, 62] Regardless, it is clear that the pattern is the same as that from parent MORx series, as it should be expected. Despite of the elevated apparent crystallinity, Cu-exchanged samples exhibit, overall, the same trend as observed for the parent samples. Despite the elevated crystallinity values, Cu-MOR050 and Cu-MOR100 exhibit some of the smallest crystallite sizes between all analysed samples, suggesting again that structural order has improved not by growing larger coherent domains, but rather by enhancing internal order within smaller ones. Incorporation of Cu may have resulted in the stabilisation of numerous small yet well-ordered domains rather than promoting domain coalescence or growth.[3, 15, 24, 62] Conversely, Cu-MOR200 and Cu-MOR360 display reduced crystallinity values, but show comparatively large crystallite sizes. This intriguing observation implies that the introduction of Cu species may facilitate partial recrystallisation or spatial realignment of fragmented framework regions, potentially during the drying phase or mild post-treatment. Altogether, the trend suggests that in highly dealuminated frameworks, Cu acts as a structural stabiliser, enabling the reformation of larger crystalline domains even when overall long-range order remains compromised.[3, 15, 24, 55, 62]

4.3 Textural Properties

The textural properties of the materials remained almost unchanged throughout the modification steps. N_2 physisorption analyses were performed, and adsorption-desorption isotherms were plotted (Figs. 4.7, 4.8 and 4.9) to confirm consistency.

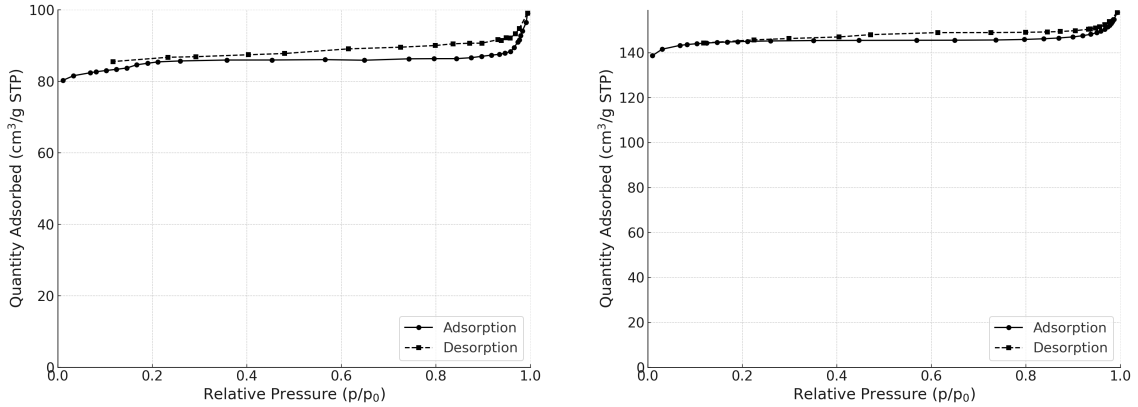

Figure 4.7: Isotherms for (a) parent Na-MOR and (b) ion-exchanged H-MOR.

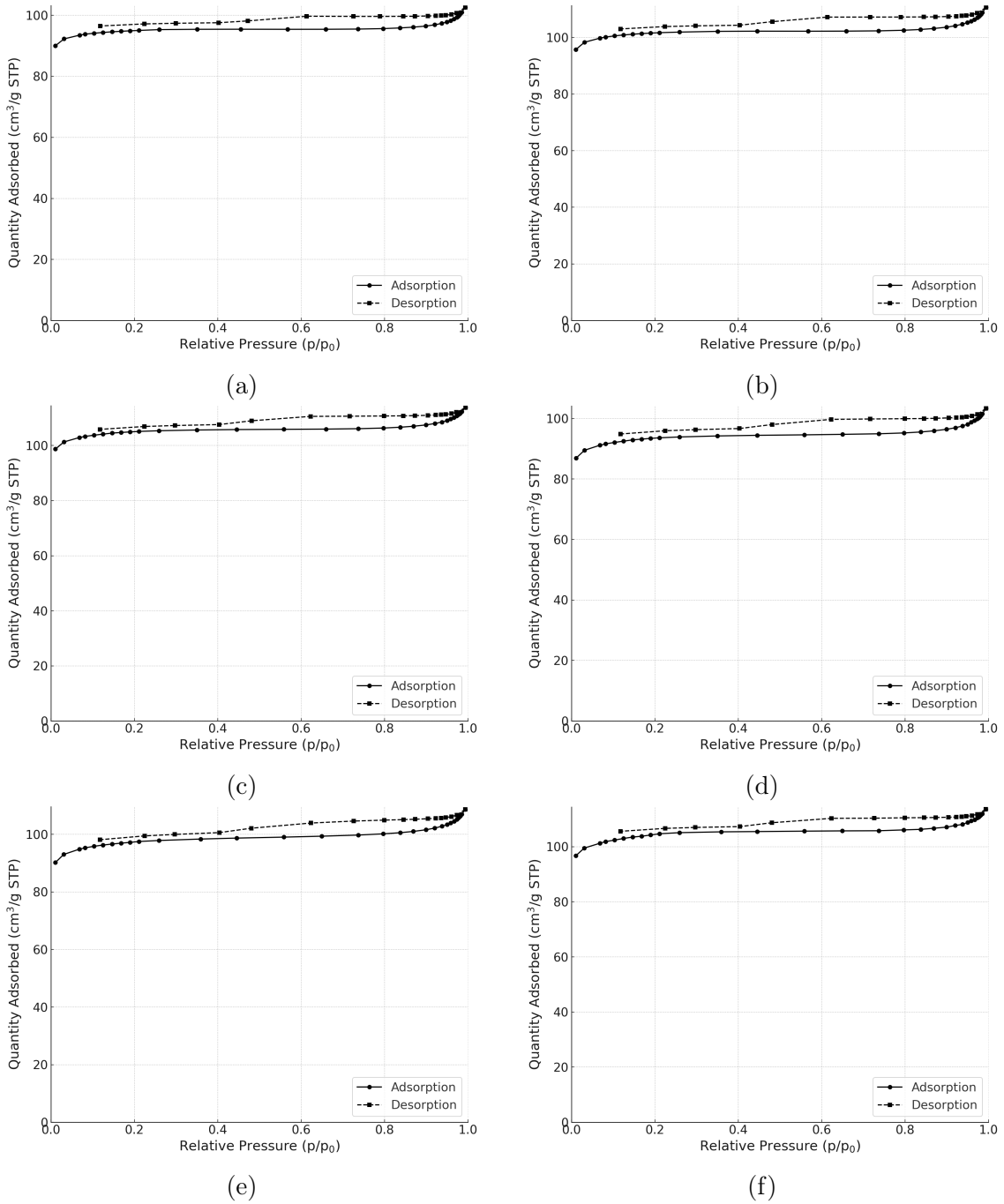

Figure 4.8: Isotherms for acid treated (a) MOR000, (b) MOR010, (c) MOR050, (d) MOR100, (e) MOR200 and (f) MOR360.

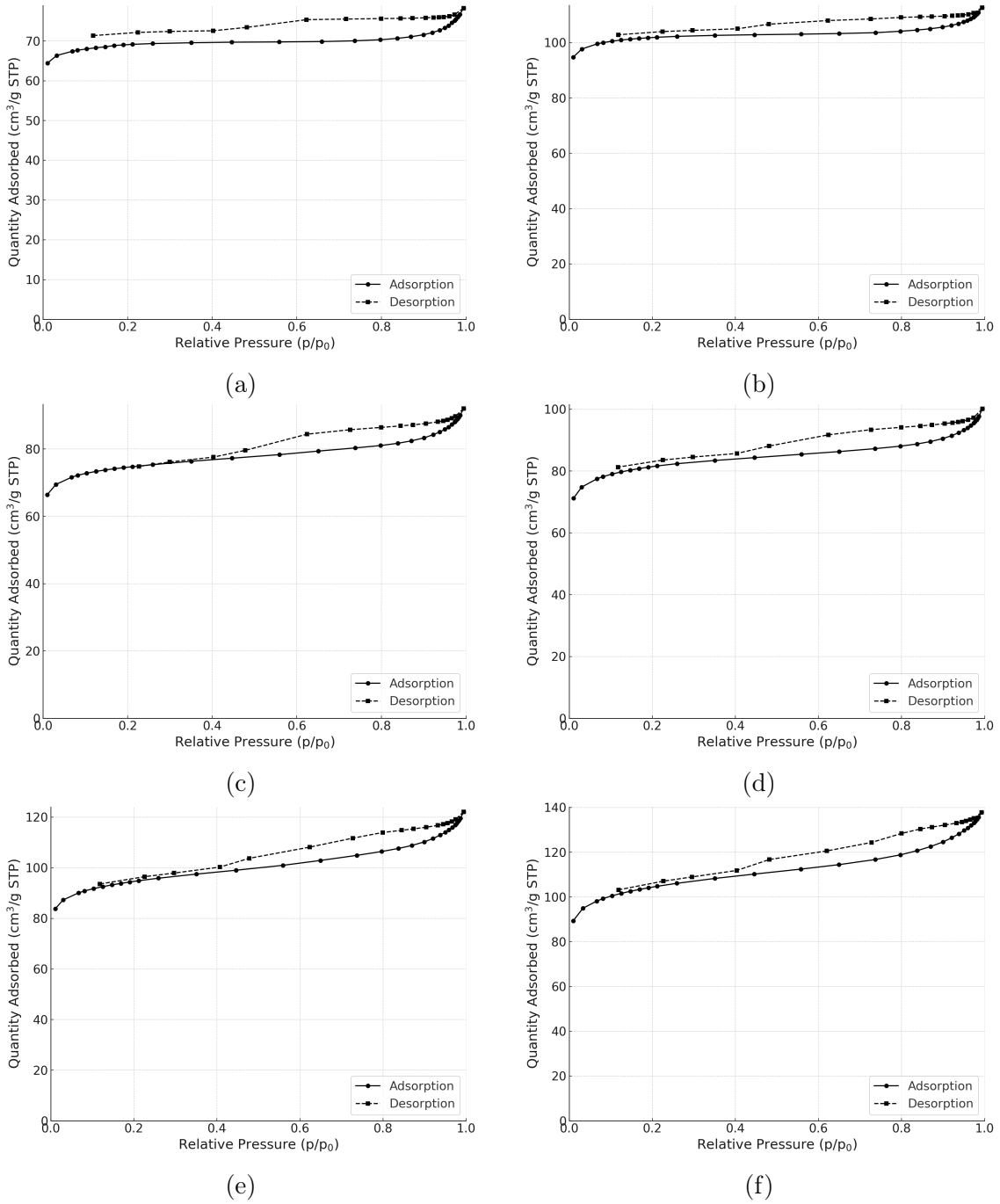

Figure 4.9: Isotherms for Cu-exchanged samples (a) Cu-MOR000, (b) Cu-MOR010, (c) Cu-MOR050, (d) Cu-MOR100, (e) Cu-MOR200 and (f) Cu-MOR360.

It is possible to observe consistent type 5 hysteresis for all the samples, indicating the presence of some mesoporosity accessible only through micropores, implying a hierarchical structure in which both microporosity and mesoporosity are in the same phase.[3, 24] However, it is clear that microporosity prevails. As a result, it was expected that the BET model would fail in representing such samples. In fact, the resulting C constants are negative for all samples (Tab. 4.3). Hence, the Langmuir

Table 4.3: BET C Constants for All Samples

Sample	**BET C Constant**
Na-MOR	-41.91
H-MOR	-36.44
MOR000	-38.14
MOR010	-38.67
MOR050	-38.60
MOR100	-38.42
MOR200	-39.28
MOR360	-39.27
Cu-MOR000	-39.68
Cu-MOR010	-36.41
Cu-MOR050	-35.73
Cu-MOR100	-34.82
Cu-MOR200	-34.18
Cu-MOR360	-38.65

model was used to calculate surface area. A summary of the N_2 physisorption results is provided in Tab. 4.4.

The untreated parent form, Na-MOR exhibits a modest surface area of 290 m^2/g and a micropore surface area of equal magnitude, suggesting that virtually all accessible surface area resides within the internal microporous channels. The external surface area is negligible, confirming the absence of mesopores or inter-particle voids. The total pore volume is 0.14 cm^3/g, of which 0.13 cm^3/g is attributed to microporosity. The pore distribution plots (Figs. A.1, A.2, and A.3, on Appendix) exhibit clear pore size concentration near 2.0 nm, which, although below the resolution limits of the BJH method, serves as a qualitative indication of microporosity. This observation aligns with the expected structural motif of one-dimensional 12-membered ring channels inherent to the MOR framework.[3, 24, 61]

Table 4.4: Selected textural properties of Na-form, H-form, dealuminated, and Cu-exchanged MOR samples.

Sample	**Langmuir Surface Area** / m^2g^{-1}	**Micropore Surface Area** / m^2g^{-1}	**External Surface Area** / m^2g^{-1}	**Total Pore Volume** / cm^3g^{-1}	**Micropore Pore Volume** / cm^3g^{-1}
Na-MOR	290	280	0	0.14	0.13
H-MOR	470	445	30	0.24	0.21
MOR000	315	285	25	0.15	0.14
MOR010	340	305	30	0.17	0.14
MOR050	350	310	35	0.17	0.14
MOR100	320	270	40	0.16	0.13
MOR200	335	280	40	0.16	0.13
MOR360	350	310	40	0.17	0.14
Cu-MOR000	280	200	30	0.12	0.10
Cu-MOR010	315	295	40	0.17	0.14
Cu-MOR050	300	200	50	0.14	0.09
Cu-MOR100	305	205	65	0.15	0.10
Cu-MOR200	315	250	65	0.18	0.12
Cu-MOR360	350	250	100	0.20	0.12

Upon ion exchange into the protonic form, H-MOR, a pronounced enhancement in textural properties is observed, with a surface area of 470 m^2/g and a micropore area of 445 m^2/g, with a concurrent increase in micropore volume to 0.21 cm^3/g and total pore volume to 0.24 cm^3/g. This transformation probably reflects the removal of extra-framework cations, in accordance to literature, which previously hindered access to the inner pores.[3, 24] The average pore width remains unchanged at 2.0 nm, indicating that, while accessibility improves, the fundamental channel architecture is retained.[3, 24, 39, 58]

Subsequent dealumination of H-MOR through oxalic acid treatment generates the MOR000 to MOR360 series. Across this progression, surface areas range from 315 to 360 m^2/g, with micropore surface areas between 285 and 310 m^2/g. These values demonstrate that despite partial framework degradation, the microporous network remains largely intact. Notably, the external surface area increases incrementally from 25 m^2/g in MOR000 to 40 m^2/g in MOR360, suggesting the development of secondary mesoporosity or inter-crystalline defects.[3, 24] The micropore volume remains stable at circa 0.14 cm^3/g across all dealuminated samples, while the total pore volume grows slightly from 0.15 to 0.17 cm^3/g. The average pore width consistently remains at 2.0 nm throughout the MORx series, confirming that the primary channels are structurally preserved, even as surface heterogeneity increases.

The subsequent introduction of Cu through ion exchange into the MOR framework leads to significant, though expected, changes in textural characteristics.[3, 15, 24, 55, 62] Compared to parent MOR000, the Cu-MOR000 sample shows a significantly reduced surface area of 280 m^2/g, with a micropore area of 200 m^2/g and external area of 30 m^2/g. The micropore and total pore volumes are also reduced to 0.10 cm^3/g and 0.12 cm^3/g, respectively. This indicates that Cu species occupy or partially block internal micropores, therefore reducing accessible surface area and volume. The average pore width remains the same, registering 2.1 nm. Such slight difference is perceived in the pore distribution data and, if considered, is potentially due to framework stress or partial rearrangement upon the introduction of Cu. The Cu-MOR010 sample presents a surface area of 315 m^2, a reduction if compared to MOR010, while micropore volume remains the same, and micropore area and external surface area are the same as the parent sample. This may suggest a redistribution of accessible porosity, most likely through partial occupation or constriction of internal channels.[3, 15, 24, 55, 62]

In case of Cu-MOR050, when compared to its parent MOR050, the surface area decreases from 350 m^2/g to 300 m^2/g, while the micropore area is substantially reduced from 310 m^2/g to 200 m^2/g. The observed external surface increases from 35 m^2/g to 50 m^2/g, and the micropore volume drops from 0.14 cm^3/g to 0.09 cm^3/g. These changes may indicate that Cu introduction into this more dealuminated ma-

trix leads to significant internal pore obstruction, although with increased mesoporosity or defect formation, as reflected by the increased external area and the slight broadening in pore distribution, resulting in the slightly higher average pore width of 2.2 nm.[3, 15, 24, 55, 62] The relatively high Cu loading typical of low-dealumination samples likely contributes to partial channel filling and Cu deposition at the micropore entrances.

Following the same logic, when compared to the parent MOR100, Cu-MOR100 surface area decreases modestly from 320 m^2/g to 305 m^2/g, while the micropore area is reduced from 270 m^2/g to 205 $^2/g$. On the other hand, the observed 65 m^2/g of external surface area exceeds that registred for the parent MOR100. Micropore volume decreases slightly, as well total pore volume. The results reflect the lower Cu loading at higher dealumination levels, leading to less severe micropore blocking.[24] A rather similar behaviour is observer for Cu-MOR200, exchanged from the extensively dealuminated MOR200 sample, in which the surface area is statistically the same as the parent (given the instrument precision limit, around 20 m^2/g), while micropore area only slightly reduced from 280 m^2/g in MOR200 to 250 m^2/g in Cu-MOR200. These minimal changes reflect the scenario in which the extensive dealumination of the parent sample limits the incorporation of Cu, resulting in negligible structural perturbation.[3, 24, 55]

Finally, Cu-MOR360, obtained from the most extensively dealuminated parent sample, MOR360, displays a surface area of 350 m^2/g, same value of its parent. The micropore area is reduced from 310 m^2/g to 250 m^2/g. Hence, an external surface area of 100 m^2/g is observed. The change in pore distribution, resulting in the higher average pore width of 2.4 nm possibly reflects blockage of smaller pores, possibly at the entrance, resulting in the elevation of external surface area.[3, 24, 55] The textural evolution observed throughout protocol implementation on the samples, while not directly correlated here to catalytic performance, are known to significantly influence the fundamental physicochemical phenomena governing reactivity in zeolite-based systems. The emergence of hierarchical porosity can facilitate mass transport by reducing diffusion limitations commonly associated with purely microporous frameworks. Moreover, the observed changes in accessible surface area and pore volume are likely to affect how reactant molecules interact with the zeolite framework, how confined they become near active centers, and how easily they can desorb after transformation.[3, 24]

4.4 Surface Acidity

The NH_3-TPD profiles reveal a clear and expected trend between the degree of dealumination and the amount of acid sites (Tab. 4.5). As expected, increasing

Table 4.5: NH_3-TPD acid sites quantification.

Sample	**Desorbed NH_3** / μmol g−1
MOR010	356
MOR100	263
MOR360	226
Cu-MOR010	225
Cu-MOR100	202
Cu-MOR360	203

dealumination severity resulted in a progressive decline in acid site concentration on MOR sample prior to Cu-exchange, reflecting the removal of framework aluminium atoms responsible for Brønsted acidity. Among the MOR samples, MOR010 exhibited the highest NH_3 uptake, with acidity gradually decreasing through MOR100 and MOR360, when it reach its lowest levels. Not surprisingly, the introduction of Cu consistently reduced the total amount of desorbed NH_3 relative to the corresponding MOR sample (Fig. 4.10). This is expected since samples prepared via ion-exchange

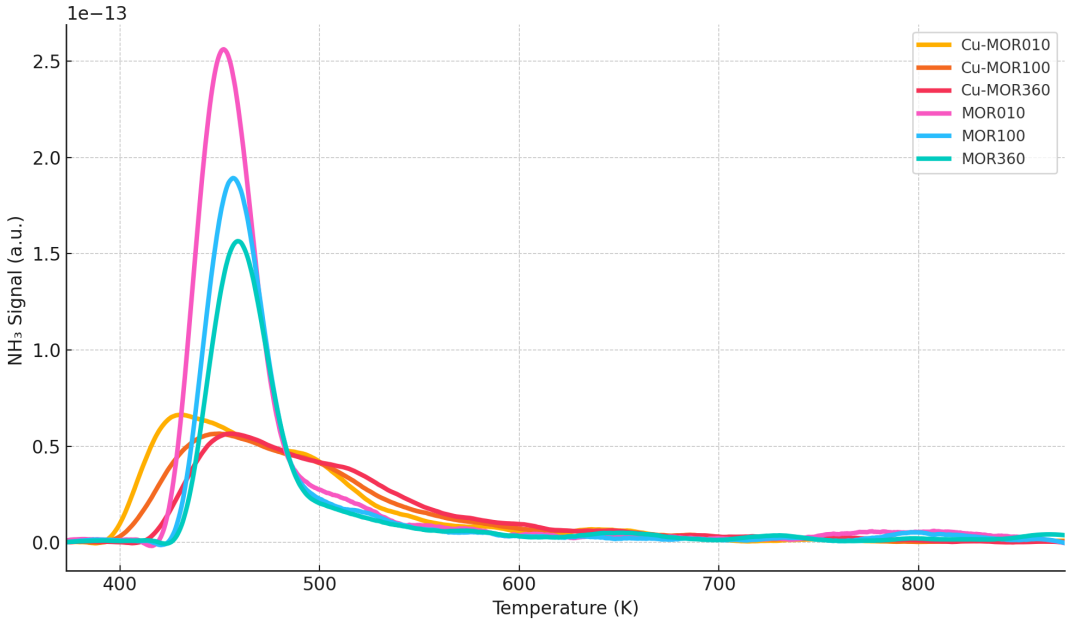

Figure 4.10: Smoothed NH_3-TPD profiles.

occur via substitution of Brønsted protons by Cu species, thereby decreasing the number of available protonic acid sites.[3, 15, 24, 55, 62] Additionally, the Cu-MOR samples retained the general trend observed in the dealuminated parent samples, with Cu-MOR010 exhibiting the highest acidity among the Cu-exchanged samples. Moreover, it is worth noting that all the Cu-MOR curves displayed broader, more asymmetric features, likely indicative of a wider distribution of acid strength and a more heterogeneous surface environment.

4.5 Catalytic Activity

CH_4-TPSR was used primarily in order to determine the temperature in which over-oxidation would start to take place, defined as the point at which CO_2 formation becomes detectable. This temperature was observed to be 454 K for Cu-ZSM5, circa 460 K for Cu-MOR000 and 480 K for Cu-MOR260. Additionally, it was possible to effectively demonstrated that CH_4 activation occurs exclusively in the presence of Cu species, as no significant CO_2 signal was observed for the H-ZSM-5 sample, indicating the material is inactivity in the absence of Cu (Fig. 4.11), in agreement with literature.[4, 5, 8, 9, 18]

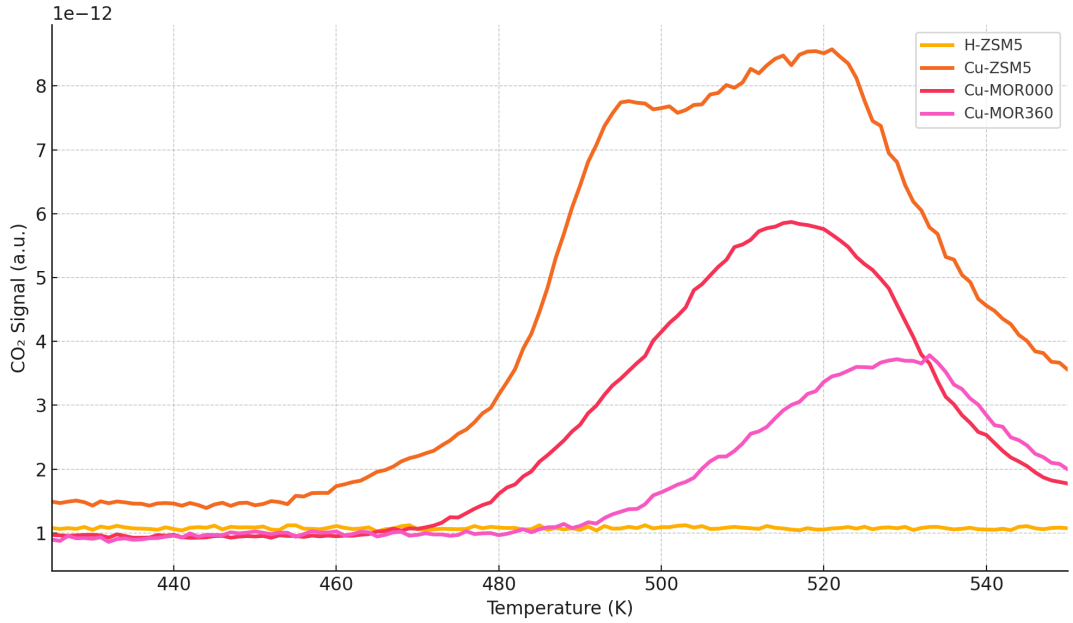

Figure 4.11: CH_4-TPSR profiles.

UV-Vis DRS was used to evaluate the change in the electronic structure of Cu species in Cu-MOR000 (Fig. 4.12). The principal absorption feature, centred around circa 260 nm and 270 nm, is generally assigned to charge transfer involving excitation from framework oxygen $2p$ orbitals to the $3d$ orbitals of Cu^{2+}.[63–65] In the fresh Cu-MOR000 sample (before O_2 activation), this band appears centred at 260 nm, with moderate intensity and a relatively narrow width, with the peak starting around 210 nm and ending around 350 nm. These features are consistent with a uniform distribution of Cu^{2+} ions in a well-defined coordination environment.[64–66] Upon O_2 activation, the absorption band undergoes a noticeable redshift, being centred at 269 nm, and a significant increase in intensity and width of the peak, starting even before the 200 nm and extending up to circa 550 nm. This spectral broadening is indicative of the formation of diverse Cu species, including Cu–oxo species, which exhibit more delocalised charge transfer transitions due to the different strength of Cu–O bonding motifs.[63–65] Following exposure to CH_4, spectra partially reverts. The absorption band undergoes a blueshift of its centre back to 260 nm, and the overall intensity diminishes back to pre-activation levels. It is worth noting that the band width does not completely reverts back to pre-activation level. Overall, this behaviour suggests partial reduction into a less absorbing state, possibly Cu^{+}.[64, 65] These observed results support the existence of electronically distinct Cu species and pose as evidence for the redox cycling during catalytical run. The data here presented is consistent the spectral behaviour reported by Grundner et al., although their reported band centre lies slightly lower.[9] Such discrepancy may be related to differences in instrumentation or data treatment.[66]

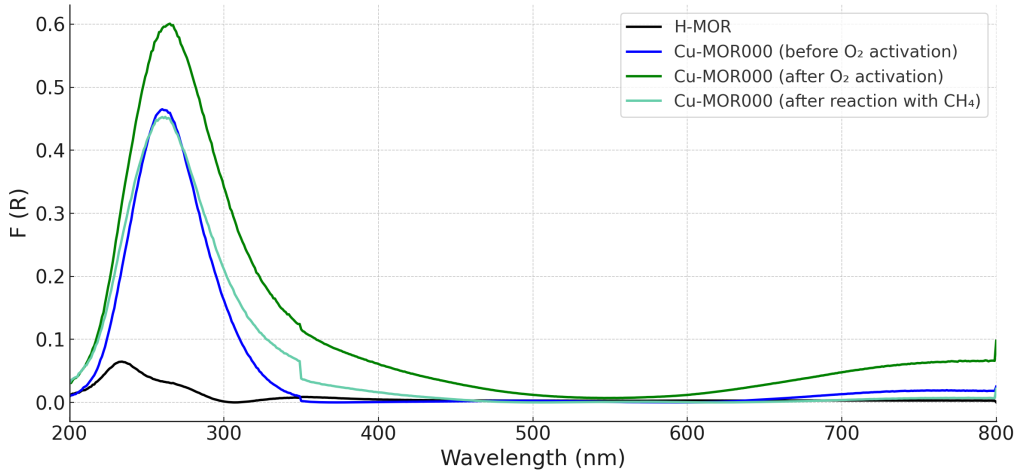

Figure 4.12: UV-Vis spectra for Cu-MOR000.

Gas outline FTIR signals was monitored as a function of time across all samples are presented on Fig. A.4. Baseline-corrected FTIR signals for CH_3OH early show substantial variation in both intensity and duration depending on the degree

of dealumination (Fig. 4.13). Total yield is calculated from the signal by evaluating the total area and applying a conversion factor from calibration curve for CH_3OH provided by the manufacturer. The overall calculated areas of analysed

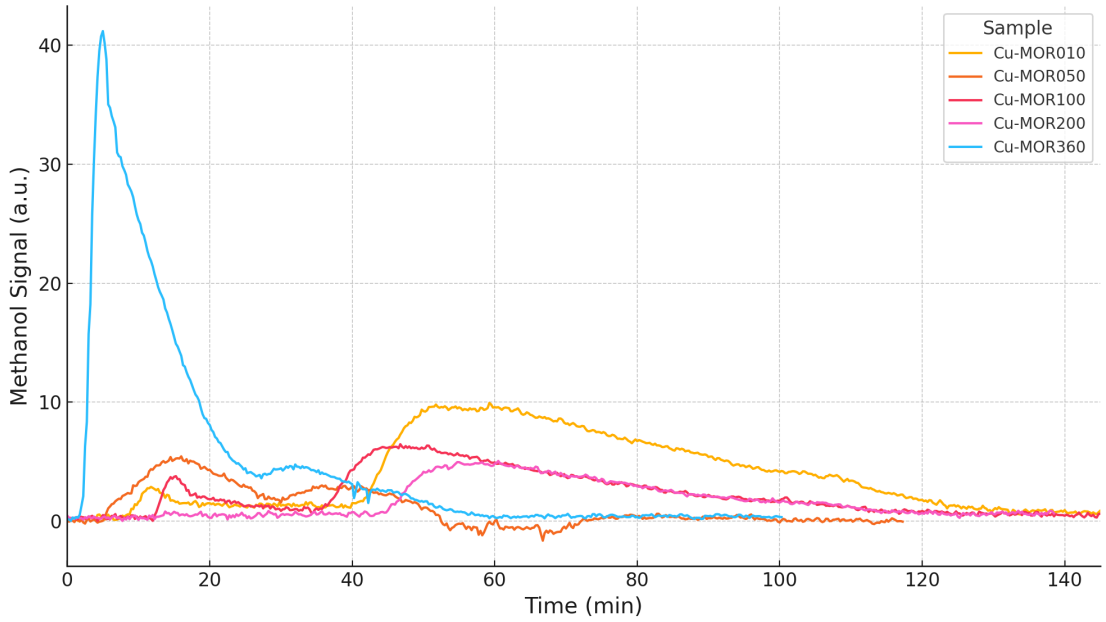

Figure 4.13: Baseline-corrected CH_3OH FTIR spectra for all samples.

products are presented on Tab. A.1. Direct analysis of the integrated areas shows that Cu-MOR010 and Cu-MOR360 clearly exhibit the highest performs in terms of CH_3OH yield. In order to provide a fair comparison, CH_3OH yield were normalised by number of Cu mols in each catalyst, calculated based on composition analysis. Both are presented on Tab. 4.6. When normalised per amount of Cu, Cu-MOR360 significantly outperforms the other samples, suggesting superior site isolation and Cu utilisation efficiency, although a definitive conclusion is dependant upon further advanced characterisation, such as via operando X-ray absorption spectroscopy (XAS).[9, 24, 56]

Table 4.6: Absolute and normalised methanol yield for each sample.

Sample	**Yield CH_3OH** (μmol)	**Yield CH_3OH** (mol mol^{-}_{Cu})
Cu-MOR010	1.84	0.0126
Cu-MOR050	0.71	0.0066
Cu-MOR100	0.89	0.0104
Cu-MOR200	0.76	0.0124
Cu-MOR360	1.64	0.0365

Catalytic results could indicate that, although moderate dealumination procedure hinder the formation of selective and redox-stable Cu species, a highly dealuminated and hierarchically modified structure may favour their formation. This behaviour may be attributed to the fact that low to moderate dealumination may be able to diminish Al avaliability without sufficiently affecting the porous configuration, thereby leading to poorly dispersed and diverse Cu speciation. In contrast, extensive dealumination, in which hierarchical porosity is observed, may potentially enhance diffusion and dispersion of Cu during the ion-exchange protocol, resulting in a more heterogeneous speciation.[24, 45, 55] It is also worth noting that N_2 physisorption demonstrate that dealuminated samples, exhibiting mesoporosity, could potentially favour accessibility of CH_4 to redox sites, as well as facilitate CH_3OH desorption, thereby contributing to the high productivity observed for Cu-MOR360.[24, 45] Additionally, this could potentially explain the CH_3OH fast desorption observed for the Cu-MOR360 catalyst, based on the time-frame of the experiment as recorded on the FTIR spectra (Fig. 4.13).

By-products were also analysed. Formaldehyde (HCHO) was detected for all samples, and its signal strongly correlates in a co-evolution with CH_3OH (Fig. 4.14). A strong positive correlation was observed, suggesting partial over-oxidation or incomplete suppression of undesired oxidation steps of CH_3OH . This is expected and commonly observed in literature.[4, 5, 19, 21, 22] Additionally, CO and CO_2 were also detected in varying amounts. Again, strong correlation can be seen between CH_3OH and both CO (Fig. A.5), $R^2 = 0.97$, and CO_2 (Fig. A.6), $R^2 = 0.95$. This is also expected since their formation occurs due to the over-oxidation of CH_3OH.[4, 5, 19, 21, 22] Moreover, it is known that adsorption energy of surface species bound to the surface through the same atom scale with each other, meaning that a correlation between CH_3OH, CO, and CO_2 is intrinsically expected.[23]

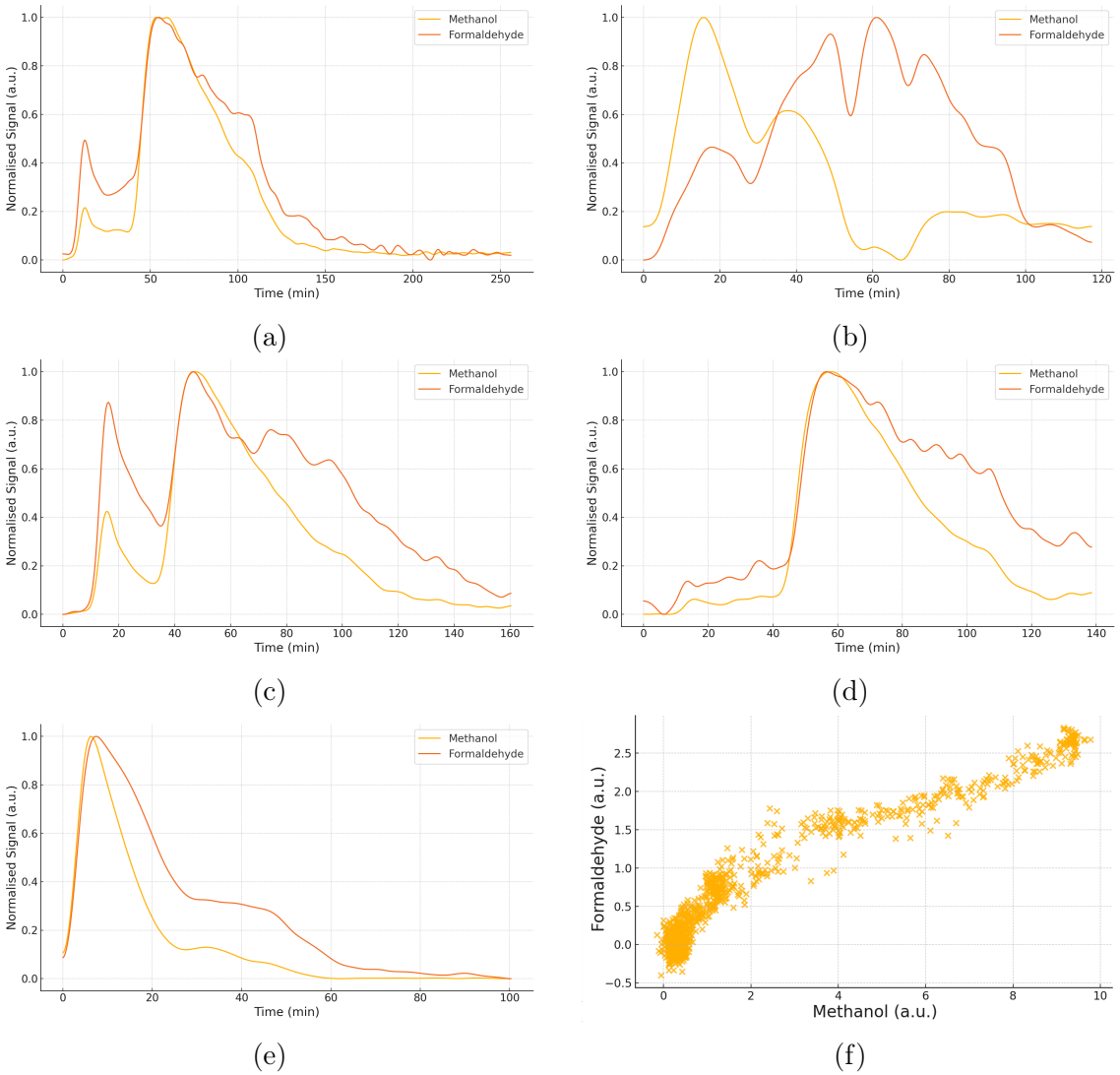

Figure 4.14: Normalised FTIR spectra of CH_3 and HCHO species for Cu-exchanged samples (a) Cu-MOR010, (b) Cu-MOR050, (c) Cu-MOR100, (d) Cu-MOR200, (e) Cu-MOR360, and (f) correlation plot for all data.

In all samples, methanol intensity started shortly after the introduction of water (Fig. 4.15), confirming its essential role as a desorption trigger.[7, 11] Interestingly, NH_3 signal also appeared consistently in a similar manner (Fig. 4.16). It is worth noting that, particularly for intermediately dealuminated samples like Cu-MOR100 and Cu-MOR200, NH_3 signals are particularly high. In contrast, these same samples exhibit lower CH_3OH production. This hints at competing pathways involving nitrogenate surface intermediates, possibly facilitated by the redox cycling of Cu sites under O_2 and N_2 exposure.[14, 24] It is worth noting that synthetic air, which mostly comprises N_2, was used as oxidant as well as carrier agent for steam. Moreover, N_2 itself was used as inert agent on cleaning steps.

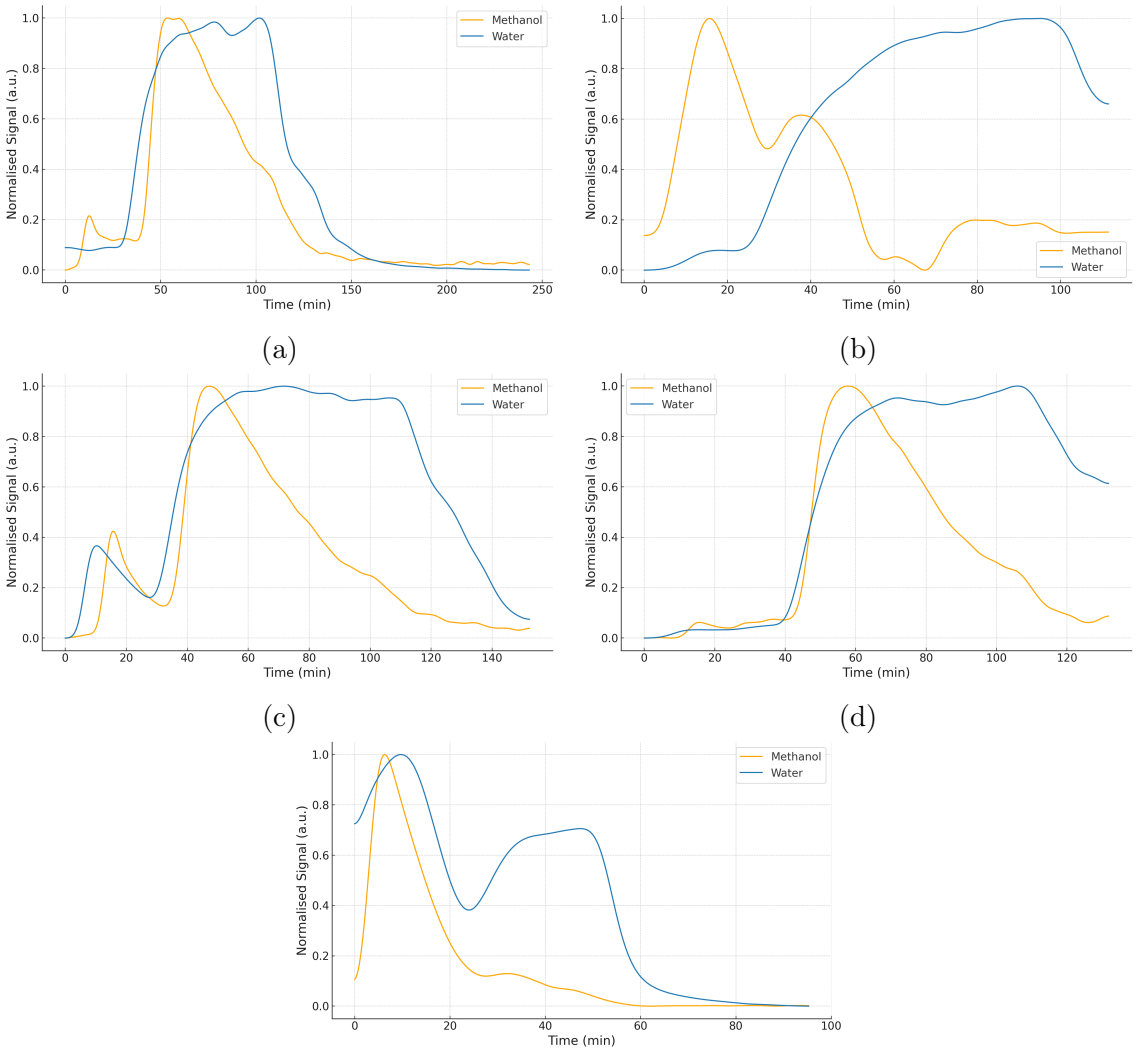

Figure 4.15: Normalised FTIR spectra of CH_3OH and water species for Cu-exchanged samples (a) Cu-MOR010, (b) Cu-MOR050, (c) Cu-MOR100, (d) Cu-MOR200, (e) Cu-MOR360.

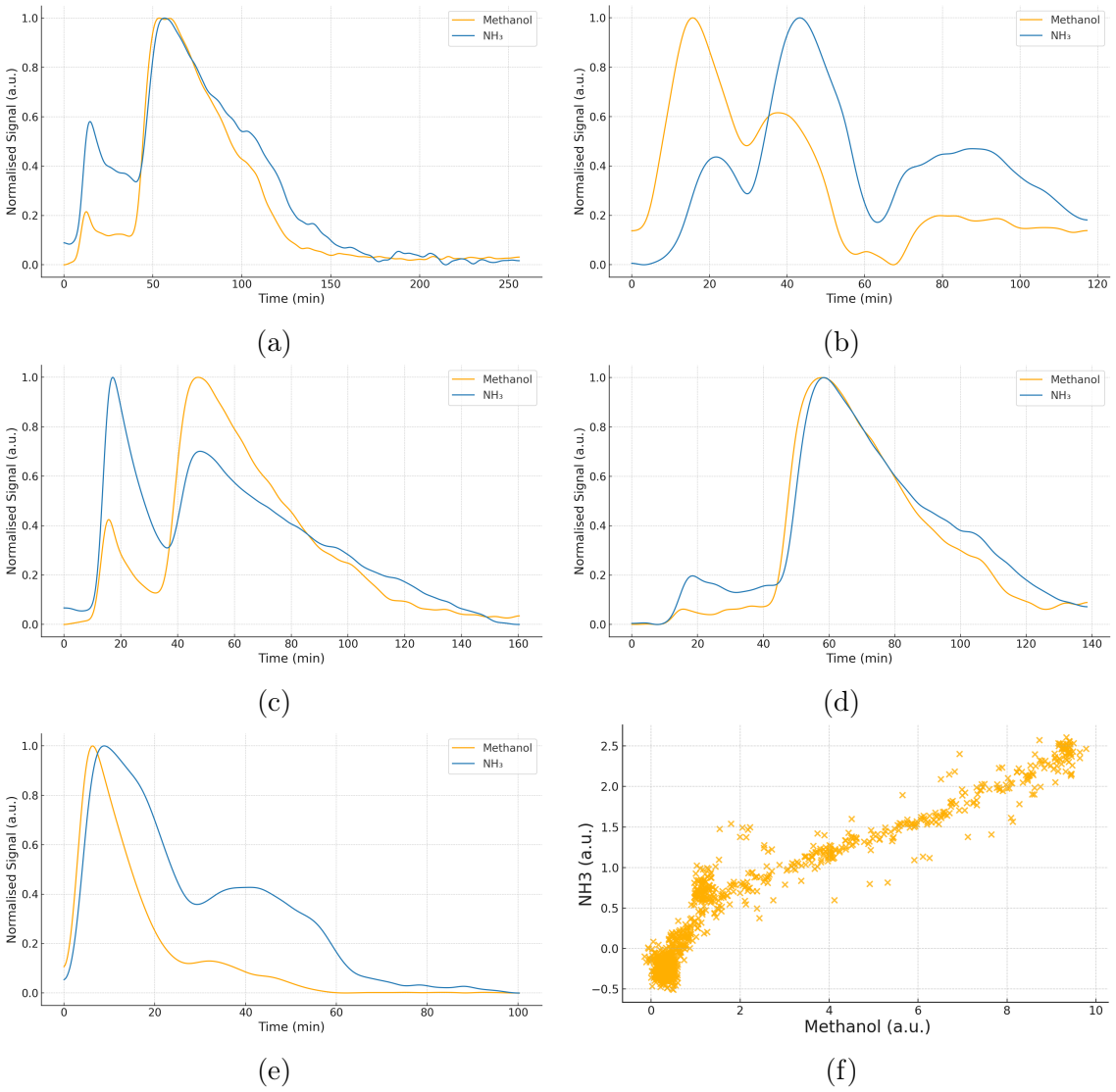

Figure 4.16: Normalised FTIR spectra of CH_3OH and NH_3 species for Cu-exchanged samples (a) Cu-MOR010, (b) Cu-MOR050, (c) Cu-MOR100, (d) Cu-MOR200, (e) Cu-MOR360, and (f) correlation plot for all data.

Other light hydrocarbons such as ethylene and propylene were detected for Cu-MOR010 showing strong signal uptake. Positive correlations between these species and CH_3OH for Cu-MOR010 (Fig. A.7) suggest the occurence of C–C coupling side-reactions. Contrastingly, all other samples displayed low or no signal variance for ethylene or propylene and, therefore, no correlation whatsoever to CH_3OH signal to be derived. It is worth noting that, in theory, less-dealuminated samples are intrinsically more prone to exhibit Brønsted acidity, behaviour that was observed by the samples TPD analysis. In such case, the zeolitic framework may possibliy be acting as catalyst itself, displaying a by-functionalised material. In contrast, more dealuminated samples like Cu-MOR360 exhibited minimal hydrocarbon release, supporting the hypothesis of increased site specificity for controlled oxidation pathways.

The heat map generated by statistical analysis on Python is shown by Fig. 4.17. PCA identified CH_3OH, water, NH_3 and HCHO as the most relevant parameters

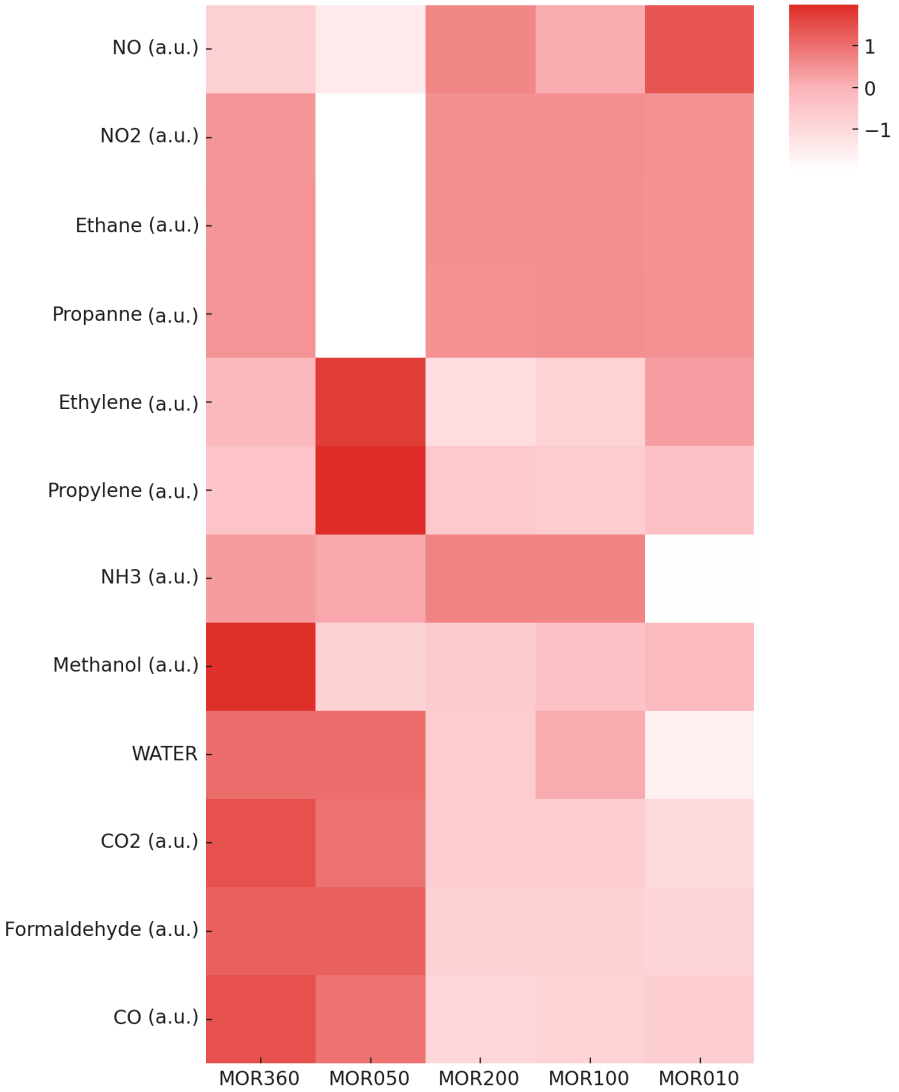

Figure 4.17: Heat-map of signal evolution for Cu-exchange MOR based on catalytical data.

across the samples. Hence, evaluating the profile on the samples across these parameters, Cu-MOR010 and Cu-MOR360 can be clustered togheter, despite being on opposite ends regarding Si/Al and Cu content. Both showed elevated CH_3OH production, although potentially through different mechanistic pathways. Cu-MOR360 performance may derive from highly selective isolated Cu sites, while for Cu-MOR010 exhibits a redox-rich but less selective active centers. Samples Cu-MOR050, Cu-MOR100 and Cu-MOR200 exhibited low CH_3OH productivity and selectivity, considering formed by-products such as nitrogenates and HCHO. Their behavior points to an imbalance in active site speciation, poorly distribution of Cu species, or even inefficient desorption. These interpretations are consistent with DFT studies indicating that the activity of Cu species is highly sensitive to both local geometry and electronic configuration, both of which can be modulated by post-synthetic treatments, incluing Si/Al modification.[7, 10]

As discussed thoroughly throughout Chapter 2, Si/Al profoundly influences the electrostatic environment of the zeolite framework, modulating the local potential and thereby the ligand field experienced by Cu ions. This field in turns ultimately governs the stabilisation of Cu species. Finally, it is possible to associate such observed behaviour with the conceptual framework of the Sabatier Principle and the occurrence of volcano plots. By directly plotting the catalytic data of CH_3OH yield against the Si/Al of associated catalyst, it is possible to observe a shape that does resemble that of a inverted volcano plot (Fig. 4.18). This profile is possibly a direct result of the complex, multi-dimensional constraints discussed. At low Si/Al, high Al density may favour Cu accumulation and over-exchange, enabling redox turnover but also promoting side reactions such as deep oxidation. At high Si/Al, although the overall number of exchangeable sites is reduced, the more isolated Al atoms, combined with lower local potentials, may be responsible for an environment that stabilises Cu species that selectively favours partial oxidation to CH_3OH. The samples with intermediate Si/Al values, however, may exhibit a mismatch in which too few paired Al sites are present for turnover number to benefit from a high overall number of sites, yet electronic conditions are not enough so that Cu species that selectively favour partial oxidation are preferably formed. This structural and electronic misbalance likely results in poorly defined Cu speciation and inferior catalytic performance. In such manner, different reaction mechanisms might be taking place according to the established conditions and formed catalytic active sites. In fact, literature [67–69] does present systems governed by overlapping mechanisms exhibiting such inverted volcano-like profiles.

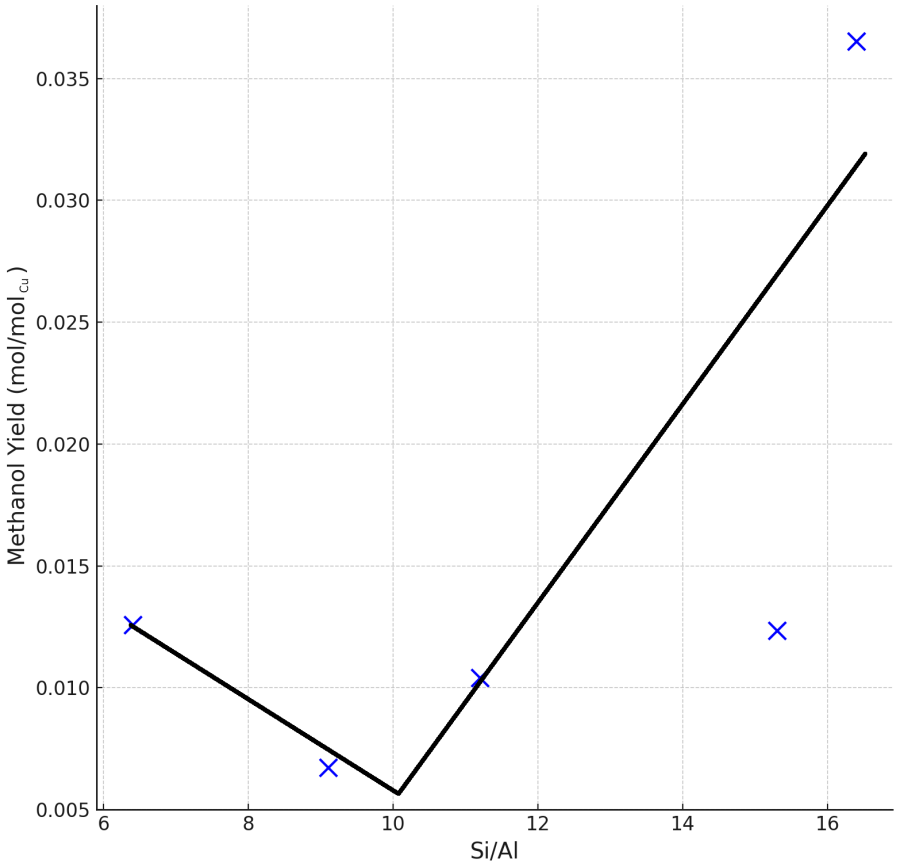

Figure 4.18: Inverted volcano-like shaped trend between CH_3OH yield and Si/Al.

Chapter 5

Conclusions and Suggestions

Modification of MOR samples was successfully implemented via a systematic protocol that was extensively validated by characterisation. XRD analysis demonstrates that the MOR crystalline structure was mainly preserved throughout all stages of treatment despite sequential ion exchange and dealumination procedures. Composition values of all final Cu-exchanged samples lay consistently under the expected nominal loadings, a behaviour that aligns with well-established literature on the limitations of ion exchange techniques. Textural analysis reveals that the applied protocol systematically affects porosity throughout samples, though in a consistent manner. Progressive dealumination induces a clear and reproducible increase in external surface area and total pore volume, an indicative of the development of secondary porosity likely associated with framework loosening and partial mesopore formation. These effects were progressive with dealumination degree and particularly pronounced in MOR200 and MOR360, whose N_2 physisorption isotherms show expanded hysteresis loops and increased pore widths. NH_3-TPD analysis confirms the presence of Brønsted acid sites in all samples and demonstrates a consistent reduction in acid site density with treatment time and resulting calculated Si/Al, coherent with the removal of framework aluminium and reduction of exchangeable protonic sites. Notably, the TPD profiles also exhibit increased asymmetry in Cu-exchanged samples, consistent with the formation of mixed site distributions, possibly involving both Brønsted and Lewis acidic centres, or even interaction with dispersed Cu species.

The catalytic experiments show that CH_3OH formation does not scale linearly with Cu content. Instead, the data support a more subtle situation in which Cu dispersion, electronic state, and framework environment, all intimately tied to the Si/Al, somehow relate to CH_3OH productivity. Cu-MOR360 sample, despite having a relatively low absolute Cu content, achieved the highest CH_3OH productivity normalised by mole of Cu. This performance may be attributed to a combination of high framework hydrophobicity, enhanced accessibility through secondary porosity,

and, specially, the stabilisation of well-dispersed Cu–oxo species that selectively yield CH_3OH. On the other hand, Cu-MOR010, possessing relatively high absolute Cu content, despite of displaying the highest overall productivity of CH_3OH, falls low on the productivity normalised by mole of Cu in the catalyst. Moreover, FTIR signals show relatively high quantities of by-products, specially nitrogenates. Such is attributed to the succeseful formation of a higher amount of active Cu species capable of CH_4 activation, but at the expense of selectivity. It is important to notice that the same redox centres active for dMtMc are usually related to the nitrogen cycle as well. The hypothesis of selective site formation in samples with high Si/Al is supported by the delayed CO_2 onset observed during CH_4-TPSR analysis, indicating a higher activation energy for total oxidation pathways. The existance of a structure and product distribution correlation is further reinforced by statistical analysis, which successfully grouped the samples according to their distinct catalytic behaviour, that shows that highly selective CH_3OH production occurs at high Si/Al while lower Si/Al benefits from possibly an overall higher conversion.

The theoretical background presented demonstrates that framework Al content modulates the local environment, leading to variable ligand field strengths and orbital splitting patterns that ultimately affect the speciation of Cu centres. Thus, zeolite framework electronic phenomena have a profound influence on the catalytic behaviour and, ultimately, on product selectivity. The experimental methodology implemented, combining systematic material modification, characterisation techniques, and catalytic evaluation, produced a coherent and highly interpretable dataset that supports the mechanistic narrative, by mapping the material structure changes and their impact in catalytic behaviour while providing a reliable interpretation of their possible implications on Cu speciation. Finally, this study reinforces that Si/Al may not merely be a compositional feature, but a crucial design parameter that fundamentally dictates the active site configuration in Cu-exchanged zeolties. Unfortunately, under the limitations of this study, it was not possible to establish a predictive framework for interpreting how catalyst structure governs reactivity.

5.1 Suggestions for Future Works

One of the main gaps in this study is the need for a more precise and quantitative assessment of the Si/Al, the EFAl species and Cu content across all samples. Although XRF provided essential insight into framework composition, the implementation of inductively coupled plasma optical emission spectroscopy (ICP-OES) would significantly enhance the accuracy and reproducibility of the compositional analysis. Specially if coupled with NMR analysis, it would be possible to rigorously deconvolute the framework and extra-framework aluminium content, enabling

a sharper evaluation on dealumination efficiency. Furthermore, ICP-OES would also allow for a more reliable quantification of Cu loading in each Cu-MOR sample. Given the subtle yet critical role of Cu in catalytic behaviour, such improved quantification would add substantial precision and credibility to the structure–activity relationships proposed in this work.

In addition, a deeper understanding of the nature of Cu species within the zeolite frameworks could be achieved through spectroscopic validation of Cu speciation via XAS techniques, namely X-ray absorption near-edge structure (XANES) and extended X-ray absorption fine structure (EXAFS). Such techniques are particularly well-suited to probe the local coordination geometry, oxidation state, and nuclearity of Cu species. The ability to resolve Cu–O and Cu–Cu distances with atomic-scale sensitivity would directly support or challenge the interpretations presented in this work.

Moreover, the application of atom probe tomography (APT) could provide unprecedented insight into the three-dimensional spatial configuration of Al within the zeolite lattice and potentially even that of Cu species. The direct visualisation of topographic distributions, combined with chemical identity at near-atomic resolution, would allow for a real-space mapping of framework heterogeneity, Cu species dispersion, and, ultimately, Al–Cu correlations. Such empirical maps could serve as a foundation for first-principles calculations, particularly through DFT modelling, providing realistic atomic models upon which more reliable simulations can be based. The coupling of DFT with experimentally obtained APT and XAS data would offer a multiscale, highly integrated understanding of the catalytic system.

Finally, there is substantial value in extending the current methodological approach to other zeolite frameworks, such as MFI, CHA, and BEA, among others. Each framework offers distinct topological constraints, channel configuration, and Al siting preferences. A comparative database across multiple frameworks would allow for generalisation or refinement of the possible structure–function relationship. Such an effort would also provide a broader perspective on the role of confinement effects, diffusion limitations, and steric control in shaping redox behaviour and product selectivity.

Disclaimer:

This document was originally written in Microsoft Word using a Microsoft 365 subscription which includes Copilot integration, configuring an AI-assisted technology. Microsoft Copilot was therefore used to assist in identifying grammatical issues, redundancies, incoherences, and inconsistencies, and to provide real-time feedback on readability. The author declares that only minor interferences were allowed and takes full responsibility for the publication's content.

References

[1] International Energy Agency (IEA), "World energy outlook 2024." `https://www.iea.org/reports/world-energy-outlook-2024`, 2024. IEA, Paris. Licence: CC BY 4.0 (report); CC BY NC SA 4.0 (Annex A).

[2] İlhami Yıldız, "1.12 fossil fuels," in *Comprehensive Energy Systems* (I. Dincer, ed.), pp. 521–567, Oxford: Elsevier, 2018.

[3] I. Chorkendorff and J. W. Niemantsverdriet, *Concepts of Modern Catalysis and Kinetics*. Germany: Wiley-VCH, 2017.

[4] M. B. Park, E. D. Park, and W.-S. Ahn, "Recent Progress in Direct Conversion of Methane to Methanol Over Copper-Exchanged Zeolites," *Frontiers in Chemistry*, vol. 7, p. 514, 2019.

[5] M. Ravi, V. L. Sushkevich, A. J. Knorpp, M. A. Newton, D. Palagin, A. B. Pinar, M. Ranocchiari, and J. A. Van Bokhoven, "Misconceptions and challenges in methane-to-methanol over transition-metal-exchanged zeolites," *Nature Catalysis*, vol. 2, no. 6, pp. 485–494, 2019.

[6] P. Tomkins, A. Mansouri, S. E. Bozbag, F. Krumeich, M. B. Park, E. M. C. Alayon, M. Ranocchiari, and J. A. vanBokhoven, "Isothermal Cyclic Conversion of Methane into Methanol over Copper-Exchanged Zeolite at Low Temperature," *Angewandte Chemie International Edition*, vol. 55, no. 18, pp. 5467–5471, 2016.

[7] G. Brezicki, J. Zheng, C. Paolucci, R. Schlögl, and R. J. Davis, "Effect of the Cocation on Cu Speciation in Cu-Exchanged Mordenite and ZSM-5 Catalysts for the Oxidation of Methane to Methanol," *ACS Catalysis*, vol. 11, no. 9, pp. 4973–4987, 2021.

[8] G. Brezicki, J. D. Kammert, T. B. Gunnoe, C. Paolucci, and R. J. Davis, "Insights into the Speciation of Cu in the Cu-H-Mordenite Catalyst for the Oxidation of Methane to Methanol," *ACS Catalysis*, vol. 9, no. 6, pp. 5308–5319, 2019.

[9] S. Grundner, M. A. Markovits, G. Li, M. Tromp, E. A. Pidko, E. J. Hensen, A. Jentys, M. Sanchez-Sanchez, and J. A. Lercher, "Single-site trinuclear copper oxygen clusters in mordenite for selective conversion of methane to methanol," *Nature Communications*, vol. 6, no. 1, p. 7546, 2015.

[10] Z.-J. Zhao, A. Kulkarni, L. Vilella, J. K. Nørskov, and F. Studt, "Theoretical Insights into the Selective Oxidation of Methane to Methanol in Copper-Exchanged Mordenite," *ACS Catalysis*, vol. 6, no. 6, pp. 3760–3766, 2016.

[11] T. Sheppard, C. D. Hamill, A. Goguet, D. W. Rooney, and J. M. Thompson, "A low temperature, isothermal gas-phase system for conversion of methane to methanol over Cu–ZSM-5," *Chem. Commun.*, vol. 50, no. 75, pp. 11053–11055, 2014.

[12] M. J. Wulfers, S. Teketel, B. Ipek, and R. F. Lobo, "Conversion of methane to methanol on copper-containing small-pore zeolites and zeotypes," *Chemical Communications*, vol. 51, no. 21, pp. 4447–4450, 2015.

[13] G. Wang, W. Chen, L. Huang, Z. Liu, X. Sun, and A. Zheng, "Reactivity descriptors of diverse copper-oxo species on ZSM-5 zeolite towards methane activation," *Catalysis Today*, vol. 338, pp. 108–116, 2019.

[14] P. Xie, T. Pu, G. Aranovich, J. Guo, M. Donohue, A. Kulkarni, and C. Wang, "Bridging adsorption analytics and catalytic kinetics for metal-exchanged zeolites," *Nature Catalysis*, vol. 4, no. 2, pp. 144–156, 2021.

[15] P. Vanelderen, J. Vancauwenbergh, B. F. Sels, and R. A. Schoonheydt, "Coordination chemistry and reactivity of copper in zeolites," *Coordination Chemistry Reviews*, vol. 257, no. 2, pp. 483–494, 2013.

[16] D. A. McQuarrie and J. D. Simon, *Physical chemistry: a molecular approach*. USA: Univ. Science Books, 1997.

[17] E. Roduner, "Understanding catalysis," *Chem. Soc. Rev.*, vol. 43, pp. 8226–8239, 2014.

[18] H. J. Kim, J. Huh, Y. W. Kwon, D. Park, Y. Yu, Y. E. Jang, B.-R. Lee, E. Jo, E. J. Lee, Y. Heo, W. Lee, and J. Lee, "Biological conversion of methane to methanol through genetic reassembly of native catalytic domains," *Nature Catalysis*, vol. 2, no. 4, pp. 342–353, 2019.

[19] N. F. Dummer, D. J. Willock, Q. He, M. J. Howard, R. J. Lewis, G. Qi, S. H. Taylor, J. Xu, D. Bethell, C. J. Kiely, and G. J. Hutchings, "Methane

Oxidation to Methanol," *Chemical Reviews*, vol. 123, no. 9, pp. 6359–6411, 2023.

[20] R. J. Jodts, M. O. Ross, C. W. Koo, P. E. Doan, A. C. Rosenzweig, and B. M. Hoffman, "Coordination of the copper centers in particulate methane monooxygenase: Comparison between methanotrophs and characterization of the cuc site by epr and endor spectroscopies," *Journal of the American Chemical Society*, vol. 143, no. 37, pp. 15358–15368, 2021. PMID: 34498465.

[21] Z. R. Jovanovic, J.-P. Lange, M. Ravi, A. J. Knorpp, V. L. Sushkevich, M. A. Newton, D. Palagin, and J. A. Van Bokhoven, "Oxidation of methane to methanol over Cu-exchanged zeolites: Scientia gratia scientiae or paradigm shift in natural gas valorization?," *Journal of Catalysis*, vol. 385, pp. 238–245, 2020.

[22] A. A. Latimer, A. Kakekhani, A. R. Kulkarni, and J. K. Nørskov, "Direct Methane to Methanol: The Selectivity–Conversion Limit and Design Strategies," *ACS Catalysis*, vol. 8, no. 8, pp. 6894–6907, 2018.

[23] J. K. Nørskov, F. Studt, F. Abild-Pedersen, and T. Bligaard, *Fundamental Concepts in Heterogeneous Catalysis*. USA: John Wiley & Sons, 2014.

[24] R. van Santen, *Modern heterogeneous catalysis: an introduction*. Germany: Wiley-VCH Verlag, feb 2017.

[25] Z.-J. Zhao, S. Liu, S. Zha, D. Cheng, F. Studt, G. Henkelman, and J. Gong, "Theory-guided design of catalytic materials using scaling relationships and reactivity descriptors," *Nature Reviews Materials*, vol. 4, no. 12, pp. 792–804, 2019.

[26] J. K. Nørskov, T. Bligaard, J. Rossmeisl, and C. H. Christensen, "Towards the computational design of solid catalysts," *Nature Chemistry*, vol. 1, no. 1, pp. 37–46, 2009.

[27] Y. Tsuji, Y. Yoshioka, K. Okazawa, and K. Yoshizawa, "Exploring metal nanocluster catalysts for ammonia synthesis using informatics methods: A concerted effort of bayesian optimization, swarm intelligence, and first-principles computation," *ACS Omega*, vol. 8, no. 33, pp. 30335–30348, 2023.

[28] P. Schlexer, "Computational Modeling in Heterogeneous Catalysis," in *Reference Module in Chemistry, Molecular Sciences and Chemical Engineering*, Elsevier, 2017.

[29] M. Schmal, *Heterogeneous Catalysis and its Industrial Applications*. Brazil/Switzerland: Springer International Publishing, 2016.

[30] F. Calle-Vallejo, D. Loffreda, M. T. M. Koper, and P. Sautet, "Introducing structural sensitivity into adsorption–energy scaling relations by means of coordination numbers," *Nature Chemistry*, vol. 7, no. 5, pp. 403–410, 2015.

[31] S. S. Borkar and M. Shetty, "Density functional theory investigation into modulating surface–adsorbate interactions with strain for ammonia synthesis on a pd (111) surface," *The Journal of Physical Chemistry C*, vol. 128, no. 31, pp. 12916–12930, 2024.

[32] A. Weilhard, I. Popov, E. C. Kohlrausch, G. N. Aliev, L. S. Blankenship, L. T. Norman, S. Ghaderzadeh, L. Smith, M. Isaacs, J. O'Shea, A. E. Lanterna, W. Theis, D. Morgan, G. J. Hutchings, E. Besley, A. N. Khlobystov, and J. Alves Fernandes, "A descriptor guiding the selection of catalyst supports for ammonia synthesis," *Chem. Sci.*, vol. 16, pp. 4851–4859, 2025.

[33] C. J. H. Jacobsen, S. Dahl, B. S. Clausen, S. Bahn, A. Logadottir, and J. K. Nørskov, "Catalyst design by interpolation in the periodic table: bimetallic ammonia synthesis catalysts," *Journal of the American Chemical Society*, vol. 123, no. 34, pp. 8404–8405, 2001. PMID: 11516293.

[34] L. Liu, Y. Zhao, X. Lin, C. Ren, Y. Gao, and W. Zhu, "Ammonia synthesis via nitric oxide electrochemical reduction on oh-mxenes: A universal descriptor," *The Journal of Physical Chemistry C*, vol. 129, no. 8, pp. 4067–4076, 2025.

[35] C. Zhi, S. Cai, D. Sun, J. Yang, and Z. Sun, "A simple descriptor toward optimizing electrocatalytic n2 oxidation to hno3 performance over graphene-based single-atom catalysts," *The Journal of Physical Chemistry Letters*, vol. 16, no. 11, pp. 2742–2751, 2025. PMID: 40052867.

[36] S. Li, Z. Luo, S. Wang, and H. Cheng, "Atomic structure and her performance of doped mos2: A mini-review," *Electrochemistry Communications*, vol. 155, p. 107563, 2023.

[37] J. Suntivich, K. J. May, H. A. Gasteiger, J. B. Goodenough, and Y. Shao-Horn, "A perovskite oxide optimized for oxygen evolution catalysis from molecular orbital principles," *Science*, vol. 334, no. 6061, pp. 1383–1385, 2011.

[38] X. Huang, J. Wang, H. B. Tao, H. Tian, and H. Xu, "An essential descriptor for the oxygen evolution reaction on reducible metal oxide surfaces," *Chem. Sci.*, vol. 10, pp. 3340–3345, 2019.

[39] L. B. McCusker and C. Baerlocher, "Chapter 3 Zeolite structures," in *Studies in Surface Science and Catalysis*, vol. 137, pp. 37–67, Elsevier, 2001.

[40] J. Weitkamp, "Zeolites and catalysis," *Solid State Ionics*, vol. 131, no. 1, pp. 175–188, 2000.

[41] J. Limtrakul, S. Jungsuttiwong, and P. Khongpracha, "Adsorption of carbon monoxide on h-fau and li-fau zeolites: an embedded cluster approach," *Journal of Molecular Structure*, vol. 525, no. 1, pp. 153–162, 2000.

[42] G. Kramer and R. Santen, van, "Theoretical determination of proton affinity differences in zeolites," *Journal of the American Chemical Society*, vol. 115, no. 7, pp. 2887–2897, 1993.

[43] A. H. de Vries, P. Sherwood, S. J. Collins, A. M. Rigby, M. Rigutto, and G. J. Kramer, "Zeolite structure and reactivity by combined quantum-chemicalclassical calculations," *The Journal of Physical Chemistry B*, vol. 103, no. 29, pp. 6133–6141, 1999.

[44] R. Santen, van, G. Ooms, C. Ouden, den, B. Beest, van, and M. Post, "Computational studies of zeolite framework stability," in *Zeolite synthesis : developed from a symposium sponsored by the Division of Colloid and Surface Chemistry at the 196th national meeting of the American Chemical Society, Los Angeles, California, September 25 - 30, 1988*, ACS Symposium Series, (United States), pp. 617–633, American Chemical Society, 1989. conference; National Meeting of the American Chemical Society ; 196 (Los Angeles, Calif.) : 1988.09.25-30; 1988-09-25; 1988-09-30 ; Conference date: 25-09-1988 Through 30-09-1988.

[45] R. Giudici, H. W. Kouwenhoven, and R. Prins, "Comparison of nitric and oxalic acid in the dealumination of mordenite," *Applied Catalysis A: General*, vol. 203, no. 1, pp. 101–110, 2000.

[46] C. Liu, G. Li, E. Hensen, and E. Pidko, "Nature and catalytic role of extraframework aluminum in faujasite zeolite : a theoretical perspective," *ACS Catalysis*, vol. 5, pp. 7024–7033, Nov. 2015.

[47] T. Bligaard, J. K. Nørskov, and B. I. Lundqvist, "Chapter 8 Understanding Heterogeneous Catalysis from the Fundamentals," in *Handbook of Surface Science*, vol. 3, pp. 269–340, North-Holland, 2008.

[48] N. Kosinov, C. Liu, E. Hensen, and E. Pidko, "Engineering of transition metal catalysts confined in zeolites," *Chemistry of Materials*, vol. 30, pp. 3177–3198, May 2018.

[49] M. Radetzki, "Seven thousand years in the service of humanity—the history of copper, the red metal," *Resources Policy*, vol. 34, no. 4, pp. 176–184, 2009.

[50] T. Brown, H. LeMay, B. Bursten, C. Murphy, and P. Woodward, *Chemistry: The Central Science*. Pearson Prentice Hall, 12 ed., 2012.

[51] A. Guo, H. Liu, Y. Li, Y. Luo, D. Ye, J. Jiang, and P. Chen, "Recent progress in novel zeolite catalysts for selective catalytic reduction of nitrogen oxides," *Catalysis Today*, vol. 422, p. 114212, 2023.

[52] M. V. Veidis, G. H. Schreiber, T. E. Gough, and G. J. Palenik, "Jahn-teller distortions in octahedral copper(ii) complexes," *Journal of the American Chemical Society*, vol. 91, no. 7, pp. 1859–1860, 1969.

[53] D. B. Rorabacher, "Electron transfer by copper centers," *Chemical Reviews*, vol. 104, no. 2, pp. 651–698, 2004. PMID: 14871138.

[54] B. Hathaway and D. Billing, "The electronic properties and stereochemistry of mono-nuclear complexes of the copper(ii) ion," *Coordination Chemistry Reviews*, vol. 5, no. 2, pp. 143–207, 1970.

[55] N. Katada, T. Takeguchi, T. Suzuki, T. Fukushima, K. Inagaki, S. Tokunaga, H. Shimada, K. Sato, Y. Oumi, T. Sano, K. Segawa, K. Nakai, H. Shoji, P. Wu, T. Tatsumi, T. Komatsu, T. Masuda, K. Domen, E. Yoda, J. N. Kondo, T. Okuhara, Y. Kageyama, M. Niwa, M. Ogura, M. Matsukata, E. Kikuchi, N. Okazaki, M. Takahashi, A. Tada, S. Tawada, Y. Kubota, Y. Sugi, Y. Higashio, M. Kamada, Y. Kioka, K. Yamamoto, T. Shouji, Y. Arima, Y. Okamoto, and H. Matsumoto, "Standardization of catalyst preparation using reference catalyst: ion exchange of mordenite type zeolite: 1. Remarkable dealumination accompanying ion exchange," *Applied Catalysis A: General*, vol. 283, no. 1, pp. 63–74, 2005.

[56] D. Skoog, F. Holler, and S. Crouch, *Principles of Instrumental Analysis*. Cengage Learning, 2017.

[57] S. Sklenak, J. Dědeček, C. Li, B. Wichterlová, V. Gábová, M. Sierka, and J. Sauer, "Aluminium siting in the zsm-5 framework by combination of high resolution 27al nmr and dft/mm calculations," *Phys. Chem. Chem. Phys.*, vol. 11, pp. 1237–1247, 2009.

[58] J. A. van Bokhoven, A. L. Roest, D. C. Koningsberger, J. T. Miller, G. H. Nachtegaal, and A. P. M. Kentgens, "Changes in structural and electronic properties of the zeolite framework induced by extraframework al and la in h-usy and la(x)nay: a 29si and 27al mas nmr and 27al mq mas nmr study," *The Journal of Physical Chemistry B*, vol. 104, no. 29, pp. 6743–6754, 2000.

[59] I. Hannus, A. Fonseca, I. Kiricsi, J. Nagy, and P. Fejes, "29si and 27al mas nmr investigation of h-mordenite dealuminated with phosgene," in *Catalysis by Microporous Materials* (H. Beyer, H. Karge, I. Kiricsi, and J. Nagy, eds.), vol. 94 of *Studies in Surface Science and Catalysis*, pp. 155–162, Elsevier, 1995.

[60] P. Massiani, F. Fajula, F. Figueras, and J. Sanz, "29si and 27al mas n.m.r. study of the distribution of si and al atoms in various forms of synthetic zeolite omega," *Zeolites*, vol. 8, no. 4, pp. 332–337, 1988.

[61] L. B. McCusker, D. H. Olson, and C. Baerlocher, *Atlas of Zeolite Framework Types*. London, England: Elsevier Science, 6 ed., Aug. 2007.

[62] P. Vanelderen, J. Vancauwenbergh, M. Tsai, R. G. Hadt, E. I. Solomon, R. A. Schoonheydt, and B. F. Sels, "Spectroscopy and Redox Chemistry of Copper in Mordenite," *ChemPhysChem*, vol. 15, no. 1, pp. 91–99, 2014.

[63] H. Praliaud, S. Mikhailenko, Z. Chajar, and M. Primet, "Surface and bulk properties of cu–zsm-5 and cu/al2o3 solids during redox treatments. correlation with the selective reduction of nitric oxide by hydrocarbons," *Applied Catalysis B: Environmental*, vol. 16, no. 4, pp. 359–374, 1998.

[64] H. Li, C. Paolucci, I. Khurana, L. Wilcox, F. Göltl, J. D. Albarracin-Caballero, A. J. Shih, F. H. Ribeiro, R. Gounder, and W. F. Schneider, "Consequences of exchange-site heterogeneity and dynamics on the uv-visible spectrum of cu-exchanged ssz-13," *Chem. Sci.*, vol. 10, pp. 2373–2384, 2019.

[65] P. J. Smeets, M. H. Groothaert, and R. A. Schoonheydt, "Cu based zeolites: A uv–vis study of the active site in the selective methane oxidation at low temperatures," *Catalysis Today*, vol. 110, no. 3, pp. 303–309, 2005. First International Workshop on the Application of Microporous and Mesoporous Materials as Catalytic Hosts for Fe, Cu and Co.

[66] F. C. Jentoft, "Chapter 3 ultraviolet–visible–near infrared spectroscopy in catalysis: Theory, experiment, analysis, and application under reaction con-

ditions," vol. 52 of *Advances in Catalysis*, pp. 129–211, Academic Press, 2009.

[67] M. J. Kolb and F. Calle-Vallejo, "The bifunctional volcano plot: thermodynamic limits for single-atom catalysts for oxygen reduction and evolution," *J. Mater. Chem. A*, vol. 10, pp. 5937–5941, 2022.

[68] K. S. Exner, "Importance of the walden inversion for the activity volcano plot of oxygen evolution," *Advanced Science*, vol. 10, no. 36, p. 2305505, 2023.

[69] T. Worakul, R. Laplaza, S. Das, M. D. Wodrich, and C. Corminboeuf, "Microkinetic molecular volcano plots for enhanced catalyst selectivity and activity predictions," *ACS Catalysis*, vol. 14, no. 13, pp. 9829–9839, 2024.

APPENDIX

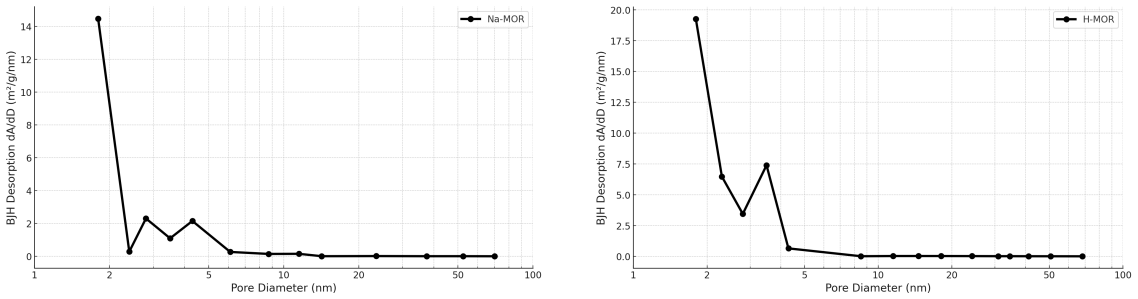

(a) (b)

Figure A.1: BJH Desorption Pore Area for (a) parent Na-MOR and (b) ion-exchanged H-MOR.

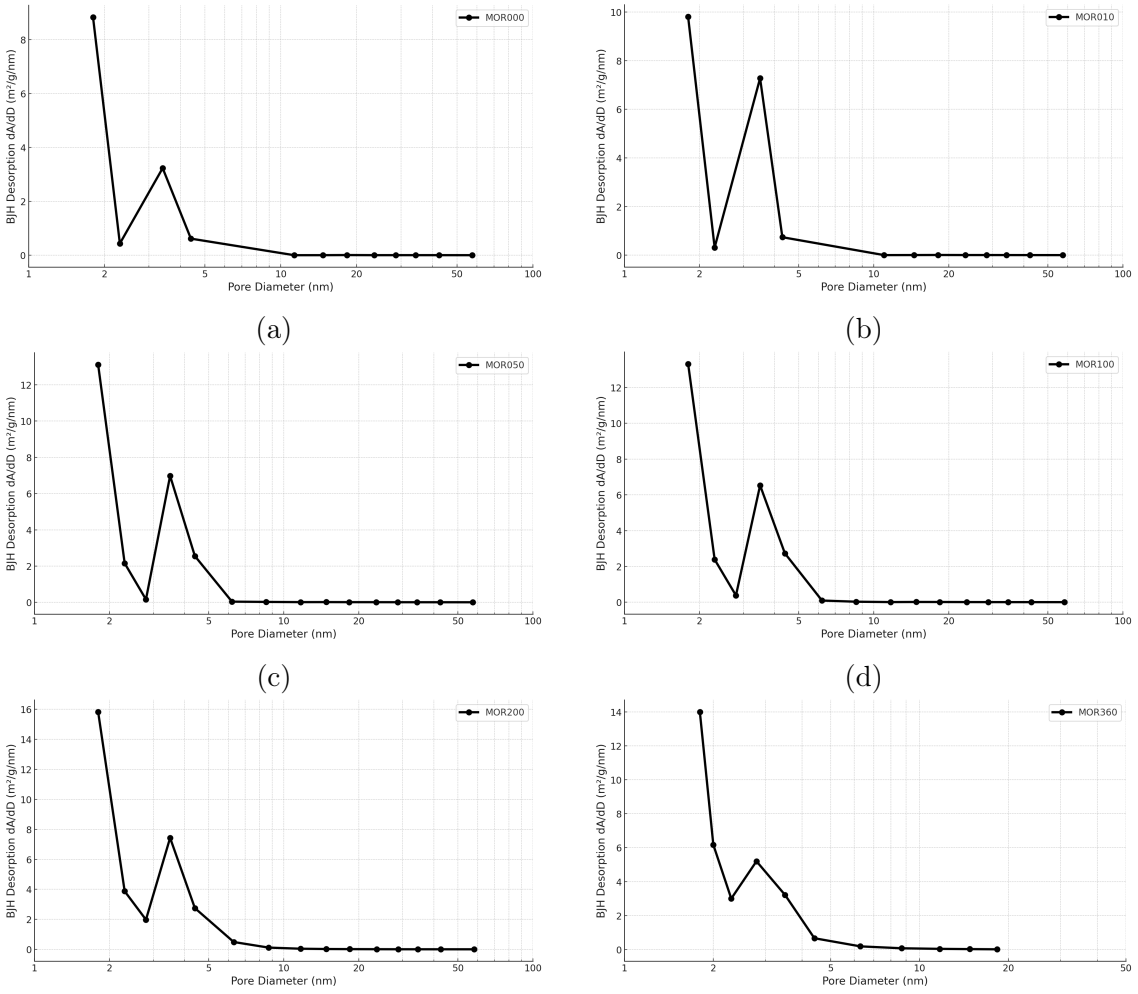

(a) (b)

(c) (d)

(e) (f)

Figure A.2: BJH Desorption Pore Area for acid treated (a) MOR000, (b) MOR010, (c) MOR050, (d) MOR100, (e) MOR200 and (f) MOR360.

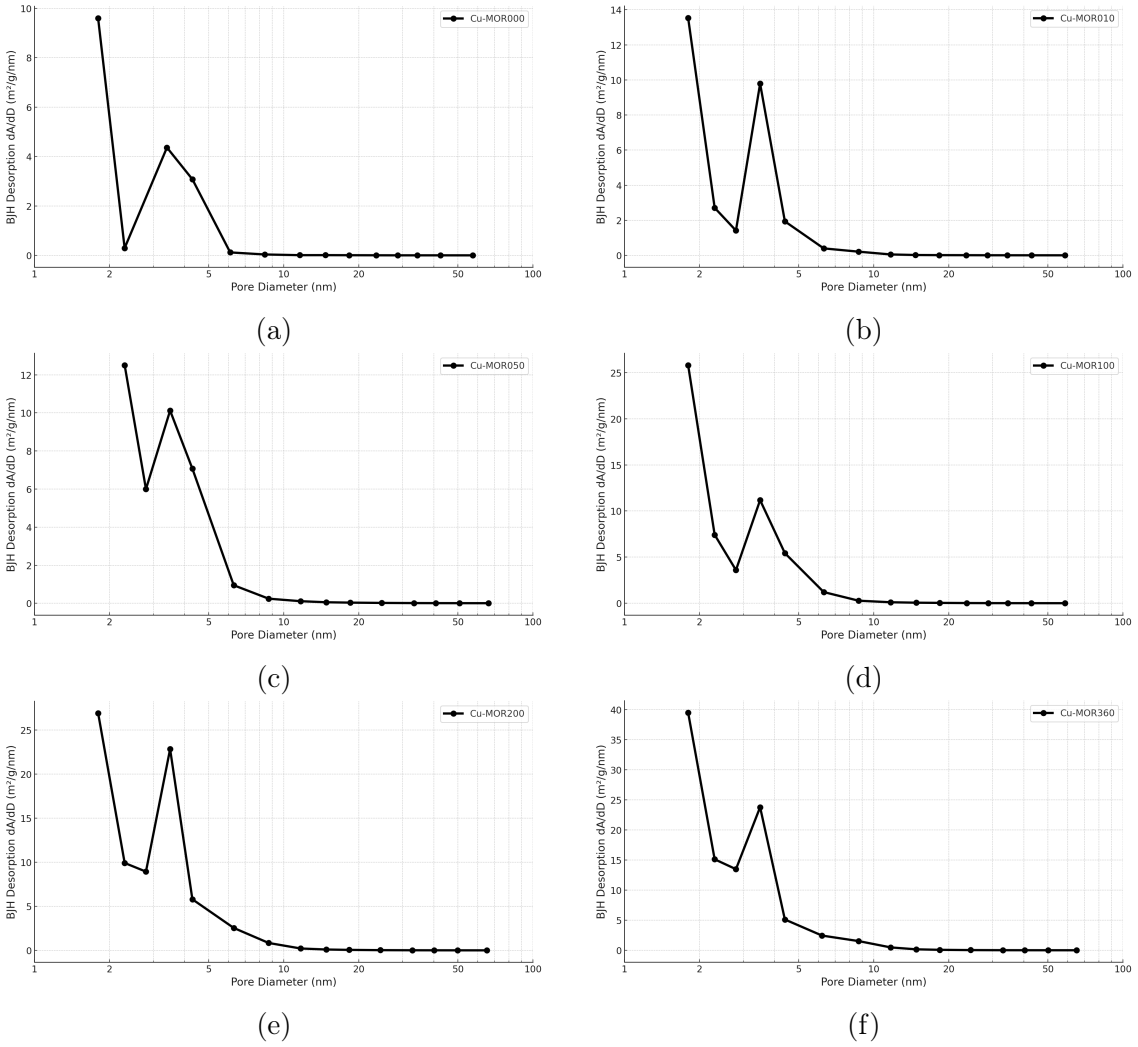

Figure A.3: BJH Desorption Pore Area for Cu-exchanged samples (a) Cu-MOR000, (b) Cu-MOR010, (c) Cu-MOR050, (d) Cu-MOR100, (e) Cu-MOR200 and (f) Cu-MOR360.

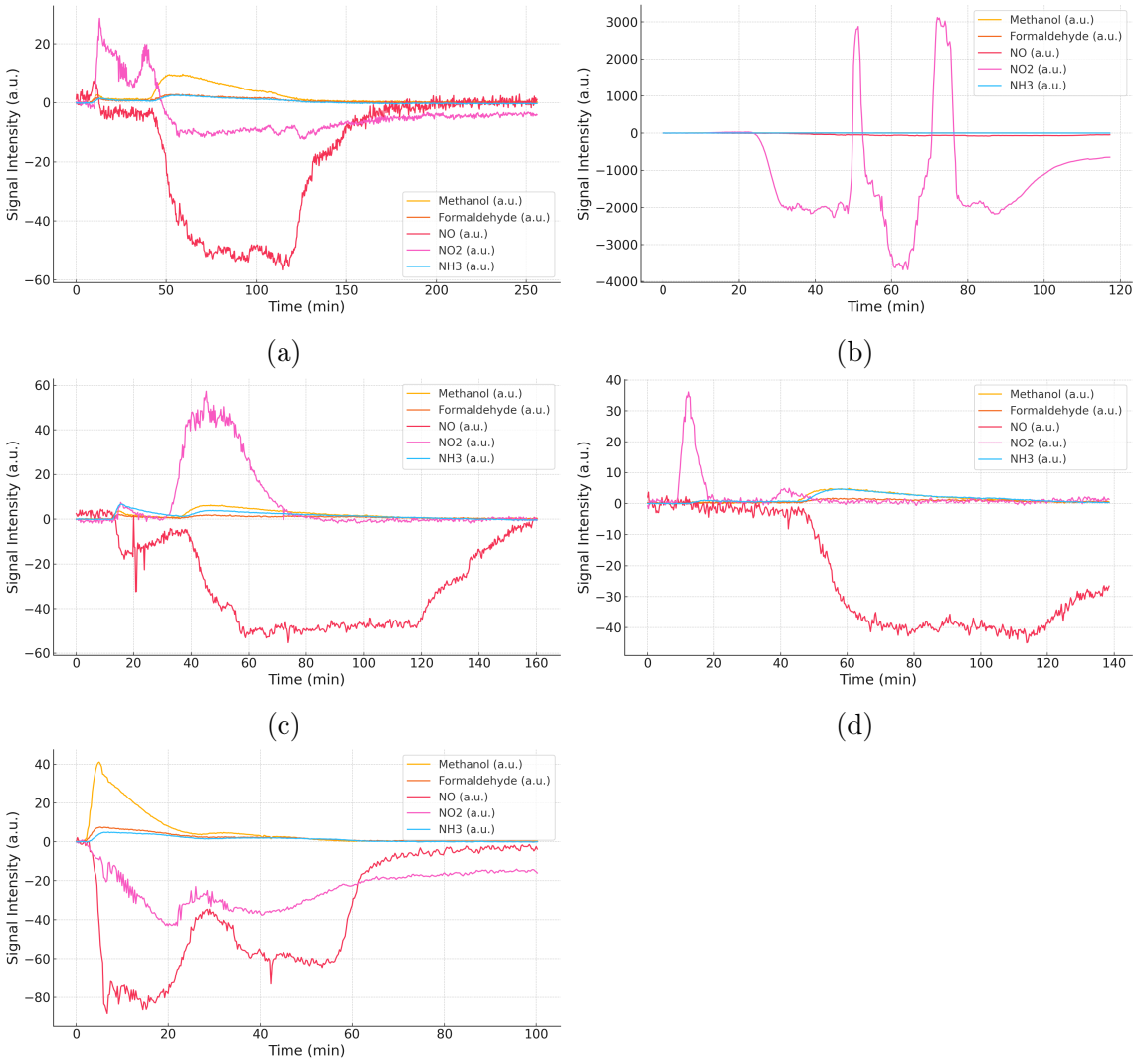

Figure A.4: Raw FTIR spectra for selected species for Cu-exchanged samples (a) Cu-MOR010, (b) Cu-MOR050, (c) Cu-MOR100, (d) Cu-MOR200, (e) Cu-MOR360.

Table A.1: Area under the FTIR spectra.

Sample	**CH_3OH**	**HCHO**	**NO**	**NO_2**	**NH_3**
	(a.u.)	(a.u.)	(a.u.)	(a.u.)	(a.u.)
Cu-MOR010	483	294	10130	2194	257
Cu-MOR050	186	282	4413	310926	185
Cu-MOR100	234	167	4301	1519	328
Cu-MOR200	199	125	2968	514	244
Cu-MOR360	431	219	5212	1959	161

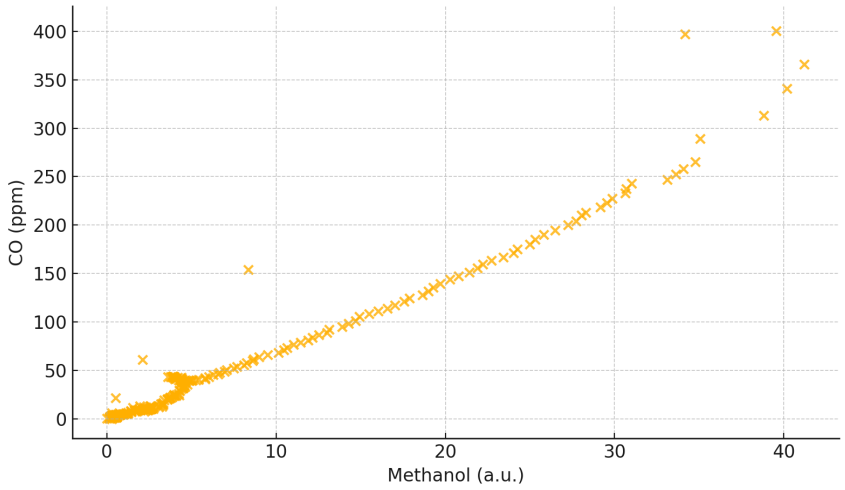

Figure A.5: Correlation plot of FTIR signals for CH_3OH and CO for all data.

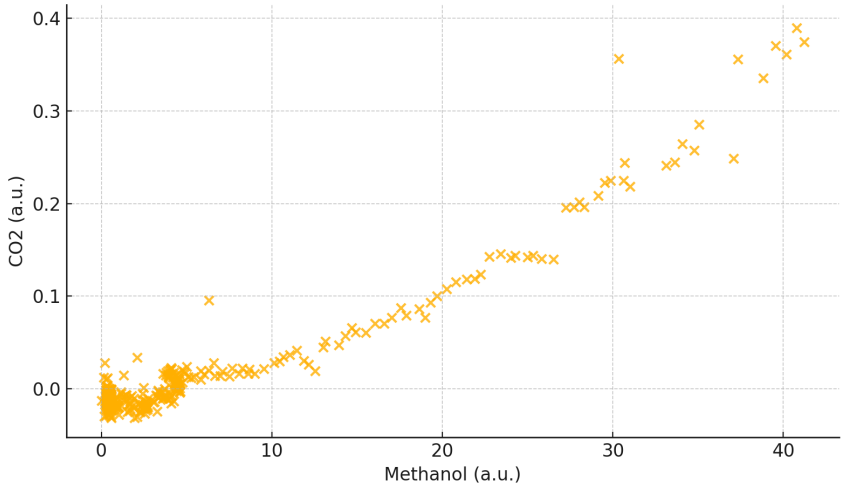

Figure A.6: Correlation plot of FTIR signals for CH_3OH and CO_2 for all data.

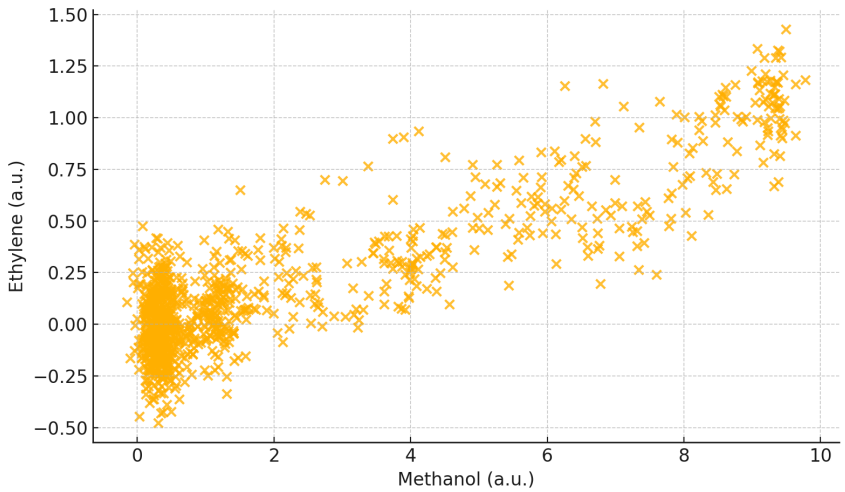

Figure A.7: Correlation plot of FTIR signals for CH_3OH and Ethylene for Cu-MOR010.